POLITECNICO DI TORINO
FACULTY OF ENGINEERING
Master's Degree course in Biomedical Engineering

Master's Degree Thesis

Optical fibre sensors for distributed temperature monitoring during mini-invasive tumour treatments with laser ablation

Supervisors:
Prof. Guido Perrone
Prof. Alberto Vallan
Prof. Gianni Coppa

Candidate:
Aurora Bellone

Academic year 2019/2020

To all those who crossed my path and walked by my side

"Be curious, learn as much as possible
making mistakes is normal.
Sbaglia con la tua testa" My parents

Abstract

The advent of mini invasive surgical techniques to treat tumours has increased the number of successful recoveries, while minimizing the patient discomfort.

These techniques usually rely on the generation of a localized thermal gradient, either heating (High Intensity Focused Ultrasound, Radiofrequency Ablation, Microwave Ablation, and Laser Ablation), or cooling (Cryoablation) the tissue at cytotoxic levels.

The aim of this Master's Thesis has been the study of novel optical fibre temperature sensors for the real-time monitoring of percutaneous Laser Ablation (LA) treatments.
Fibre Optic sensors are particularly attractive for LA because they can be integrated into the applicator, do not introduce artefacts due to interactions with the laser beam; moreover, being all non-conductive, they cannot cause electrocution and can be used under the Nuclear Magnetic Resonance procedures employed to position the applicator and monitor the treated tissue evolution.

Two types of sensors suitable multi-point measurements along a single fibre have been investigated and compared:

- 1) Arrays of multiplexed Fibre Bragg Gratings (FBGs) for quasi-distributed sensing;
- 2) Optical Frequency Domain Reflectometry (OFDR) in Single-Mode Fibres (SMFs) for fully distributed sensing.

FBGs are optical devices with notch filter response, so that they propagate all the wavelengths except for some centred at the so-called Bragg wavelength, which are reflected toward the source because of the backscattering phenomena.
The Bragg wavelength shifts linearly with temperature, allowing estimating temperature variations from spectral response changes.

Multi-point sensing to recover the temperature distribution in the treated region can be obtained by cascading FBGs with different Bragg wavelengths.

For this work, arrays up to 15 FBGs with 1 mm spacing have been written by femtosecond laser in single-mode telecom-grade fibres.
FBG arrays can be interrogated with tunable lasers obtaining 0.1 °C resolution with a 2 mm spatial resolution.

SMFs can also be used as a truly distributed temperature sensor by measuring the Rayleigh scattering, which is dependent on the local temperature, as a function of the position.

The Rayleigh scattering can be measured with an advanced instrument called optical backscatter reflectometer, which allows evaluating the temperature with sub-millimetre spatial resolution.

Both types of sensors have been first characterized and calibrated in a climatic chamber.

Then, in order to investigate their distributed sensing capabilities, a specific setup using a metallic cantilever devised to generate linear thermal gradients has been built.

Both the FBG array and the OFDR have allowed recovering a temperature distribution profile in agreement with a reference measure obtained from thermocouples.

Finally, both optical fibre sensors have been used to monitor a laser ablation test on ex-vivo bovine liver.

Again, both recovered temperature profiles have been found in agreement with reference measures obtained with a thermographic camera, demonstrating that both sensors represent promising tools for monitoring of the temperature during LA treatments.

Acknowledgements

This work has been possible thanks to the supervisors of my work: Professor Guido Perrone and Professor Alberto Vallan, I want to thank them for the possibility they gave me to be part of this project and for their kind disponibility to explain and support me.

A kind thanks goes to Professor Gianni Coppa, for have given to me the possibility to know about this project and to Massimo Olivero, for having followed me in my initial period at Links Foundation.

Thank you to the lab mates, becoming familiar in so little time.

The biggest thanks to my family, especially my parents: without your love my path would not have lead me to this point; to all my friends, the lifelong and the newest but profound for the energy and the positivity shared with me, to Zoe for having taught that life is like a cat and to my Riccardo (and his family), for your immense patience and for you love even in stressful moments, you know what it means to me.

You all have believed in me, thank you!

"Contano due princìpi:
non farsi mai troppe illusioni e non smettere di
credere che ogni cosa che fai potrà servire."
Italo Calvino

Aurora Bellone

Contents

Chapter 1

Introduction

According to the World Health Organization (WHO), cancer incidence and mortality are increasing worldwide, becoming the first cause of death over heart disease [1]. The esteems predict that the number of incident cases will increase with a rate of 2.5 million in 5 years, up to 30 million cases in 2040, and that the number of mortality cases will reach 16.4 million in 2040 (Fig. 1.1). The most common types of cancer affect the lungs, the female breast and the colorectum 1.2.

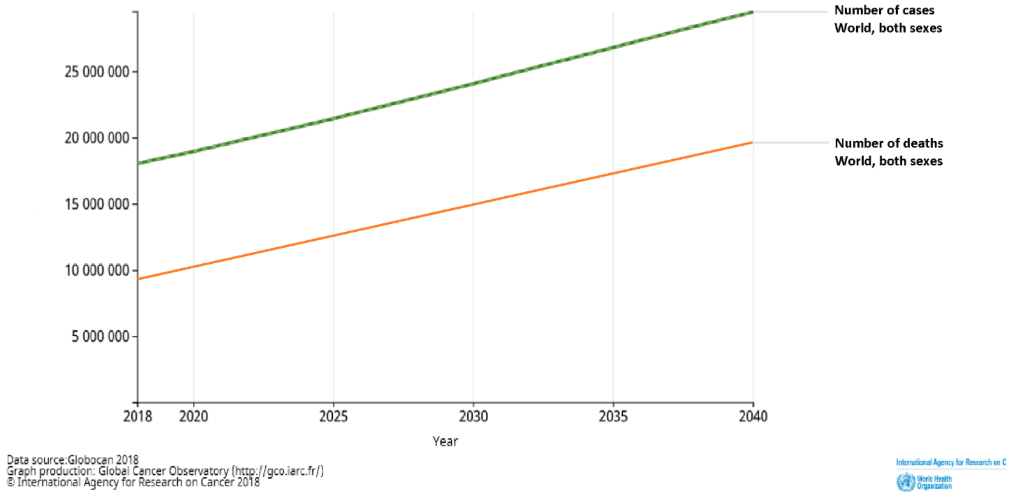

Data source:Globocan 2018
Graph production: Global Cancer Observatory (http://gco.iarc.fr/)
© International Agency for Research on Cancer 2018

Figure 1.1: Estimated of incident cases and death from 2018 to 2040, all cancers, both sexes, all ages. Adapted from [1].

The cancer site is a crucial factor to determine the therapeutic approach. For some neoplastic forms, an efficient and well-established treatment has been developed; but other forms are more critical both in the diagnosis both in the treatment. A concrete example of a critical neoplasia is the liver cancer, which is predicted to become the sixth most diagnosed cancer and the fourth cause of death. The most diffused liver cancer is the HepatoCellular Carcinoma (HCC), which can be originated by hepatitis B and C, alcohol abuse, obesity and type 2 diabetes [1][2].

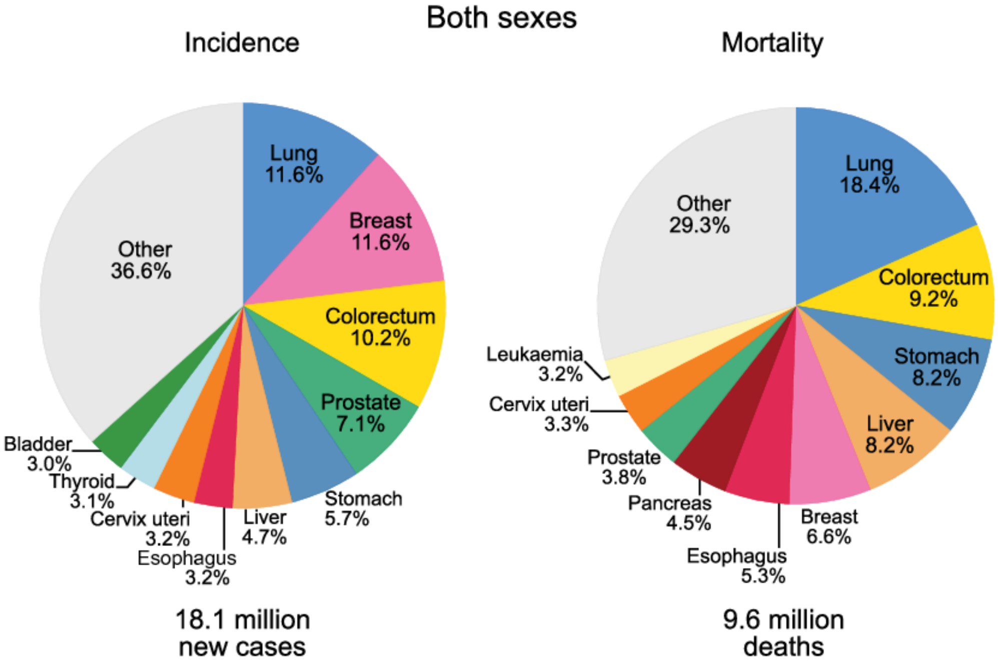

Figure 1.2: Pie Charts Present the Distribution of Cases and Deaths for the 10 Most Common Cancers in 2018 for Both Sexes. The area of the pie chart reflects the proportion of the total number of cases or deaths; non-melanoma skin cancers are included in the “other” category [1].

HCC is difficult to be treated with traditional surgical approaches because of the complex structure of the liver and its distinctive features, such as the friability and its venous reticulum; on the other hand, mini-invasive surgeries represent a viable approach, especially those relying on thermal treatments to raise the temperature above the cytotoxic level. Among the various thermal mini-invasive treatments, this thesis discusses some aspects related to the monitoring of the Laser Ablation (LA), which, as the name implies, uses the absorption of laser light from the tissue to generate a localised thermal increase leading to cellular necrosis. In particular, targeting deep-laying organs such as liver, in this thesis it is assumed that the laser beam is delivered through an optical fibre percutaneously inserted.

LA is one of the latest mini-invasive thermal treatments – most known are the Radio-Frequency Ablation (RFA) and MicroWave Ablation (MWA) – with very promising perspectives, but not yet widely deployed for different reasons, among which the necessity of accurate measurement of the induced temperature to optimise the treatment result. This, however, is not an easy problem and the aim this Master’s degree thesis is to compare different noninvasive fibre optic based solutions to measure the temperature distribution profile during laser ablation processes.

The possibility to measure the temperature in different point across the tumour mass in real-time is fundamental to allow adjusting the laser power and the treatment duration. The solutions investigated in this thesis include both quasi-distributed – specifically, arrays of Fibre Bragg Gratings (FBGs) – and distributed – a standard Single-Mode Fibre (SMF) in which it is measured the Rayleigh scattering – fibre sensors.

The thesis is organised to reflect the order in which the activities have been carried out. First, the physical principles underlying the different approaches (e.g., optical fibres, FBGs, scattering phenomena in fibres) and the operating instructions of the devices and instruments used (e.g., handling of optical fibres FBG-interrogator, etc.) have been studied. This is described in the first part of the thesis.

Then, an experimental activity has been carried out. Different sets of FBG arrays have been characterised in a climatic chamber to extract the descriptive parameters of their thermal behaviour. At the same time, some fibres to be used as distributed optical sensors have been employed for preliminary thermal test. The behaviour of the two types of sensors has been compared in different conditions, to mimic actual operating environments. In particular, an ad-hoc setup to generate linear temperature gradients has been designed and implemented. Finally, ex-vivo laser ablation tests have been conducted using a bovine liver to compare the two types of sensors in the presence of the laser beam and in highly non-uniform temperature conditions. This is described the in the second part of the thesis, devoted to the description of the experimental tests and the presentation of the obtained results.

Part I

Theoretic background

Chapter 2

Minimally invasive surgery techniques

The development of minimally invasive thermal treatments has offered an interesting alternative to all those tumoral patients who are not eligible for traditional surgery. Indeed, thermal treatments are less traumatic and require fewer days of hospital recovery; however, they can be used only for small tumour dimensions, smaller than about 3 cm in diameter [3].

The anatomic sites typically treated with these techniques are kidneys, prostate, pancreas and liver. Liver is particularly interesting because it is a common site for metastasis due to its blood perfusion and its filtering properties.

In all these cases, the thermal treatment is done with applicators that are inserted through the skin using needles (percutaneous insertion), reducing the time of recovery and possible post-surgery complications. The exact positioning of the guiding needle is defined using image guided procedures, such as with Ultrasounds (US), Magnetic Resonance (MR), or Computed Tomography (CT).

Thermal treatments are usually distinguished in conventional hyperthermia and in ablation therapy, depending on the maximum temperature and the extension of the area treated [4]. In conventional hyperthermia, a part of the body, such as an organ, (regional hypertemia) or the entire body (whole-body hyperthermia) is heated up to 42 °C-45 °C (basically, a very strong fever) as a way to make chemotherapy work better in treating cancer that has spread (metastatic cancer). On the contrary, in ablation techniques very high temperatures (above 55 °C) are induced in a localised area to directly kill the cancer cells and destroy nearby blood vessels. In practice, this cooks the exposed area causing irreversible damage to cells. Radio waves, microwaves, ultrasound waves, and laser beams can be used to heat the area, giving origin to treatments knwon as Radio-Frequency Ablation (RFA), MicroWave Ablation (MWA), High Intensity Focused Ultrasound (HIFU), and Laser Ablation (LA), respectively. Alternatively, very low temperatures can be used as well to kill malignant cells, in the so-called cryotherapies [5, 6, 7].

The effects on the tissue cells of the temperature level and the duration of the treatment are summarised in Tab. 2.1 [8]. Considering the temperature increase only, it is possible to distinguish four cases:

- $T < 50\,^{\circ}\mathrm{C}$ for which reversible cellular damages are caused;

- $50\,°\mathrm{C} < T < 100\,°\mathrm{C}$ for which biomolecular and protein denaturation occur;
- $T \geq 100\,°\mathrm{C}$ for which the water inside the tissue evaporates;
- T > 300 °C for which carbonisations occur.

Table 2.1: Effect of temperature on biological tissues [8].

Temperature range (°C)	Time requirements	Physical effects	Biological effects
< - 50	> 10 min	Freezing	Complete cellular destruction
0 - 25		Decreased permeability	Decreased blood perfusion, decreased cellular metabolism, hypothermic killing
30 - 39	No time limit	No change	Growth
40 - 46	30 - 60 min	Changes in the optical properties of tissue	Increased perfusion, thermotolerance induction, hyperthermic killing
47 - 50	> 10 min	Necrosis, coagulation	Protein denaturation, not subtle effects
> 50	After ∼ 2 min	Necrosis, coagulation	Cell death
60 - 140	Seconds	Coagulation, ablation	Protein denaturation, membrane rupture, cell shrinkage
100 - 300	Seconds	Vaporisation	Cell shrinkage and extracellular steam vacuole
> 300	Fraction of a second	Carbonisation, smoke generation	Carbonisation

In the case of ablation procedures in the liver, a critical issue comes from the relevant effect of blood perfusion, because this organ has important blood vessels that can play the role of either sink or source of thermal energy (not to mention the that the important flow of blood can contribute to diffuse the neoplastic cells originating metastasis).

The next sections describe in more detial the technologies that involve the heating of the target tissue, which are:

- Radiofrequency ablation [5, 6, 7, 9, 10]
- Microwave ablation [5, 6, 7]
- High-intensity focused ultrasound [5, 6]
- Laser ablation [5, 6, 7, 9, 11, 12, 13, 14]

2.1 Radiofrequency ablation

RFA is the today most used mini-invasive surgery technique. It is derived from the electrocautery and makes use of the electrical currents at about 450 kHz directly applied to the tissue to treat [5]. There are two types of operations: monopolar and bipolar RFA.

Monopolar operation

The alternating current from the electrode inserted in the target area flows in the tissue towards a wide electrode on the skin surface (grounding electrode), causing an increase in the temperature in the tissue on which the power is delivered. The limit of this type of electrode is in the size of the treated area, which is less than 1.6 cm [10].

Multipolar operation

The current flow can travel between two or more small electrodes, individually inserted into the neoplastic site. The arrangements of the electrodes can be tailored and also multi-electrode probes can be used to increase the ablation area size. However, complex applicators consisting of three or more parallel arrays of electrodes are more invasive and requires that several needles are precisely placed inside the tumour mass. Examples of practical applicators are the umbrella-, basket-, and star-shaped electrodes shown in Fig. 2.1, which can treat areas up to 4 cm in diameter [6].

RFA relies on Joule effect for which heat is produced by the friction of cellular ions agitated by the alternating current. To avoid a localised hot spot close to the applicator, the electrodes can also be internally cooled.

The positive effects of RFA are the same of all mini-invasive thermal treatments, moreover it decreases the possibility of bleeding problems due to its cautery property. On the contrary, the disadvantages are mainly related to the intrinsic dependence on the variation of impedance seen by the electrodes. Indeed, the impedance is inversely proportionality with the quantity of water inside the tissue, so that it increases as the treatment proceeds, therefore making it less effective. Moreover, localised high temperatures could lead to the generation of vapour, which acts practically as an insulator. In these conditions the overall ablative effect is achieved mainly by thermal conduction.

2.2 Microwave ablation

MWA is the second most used ablative technique. It is similar to RFA, but it uses an electromagnetic signal at higher frequency, around 2.45 GHz, which heats again by the Joule effect as it causes the oscillations of the water molecules inside the tissue, thus, the heating is obtained again by Joule effect.

The advantages, especially over RFA, are the absence of grounding pad and of risks of related localised burns, the more uniform temperature in the treated area and the substantial invariance of the tissue impedance as the ablation proceeds. There are, anyway, some

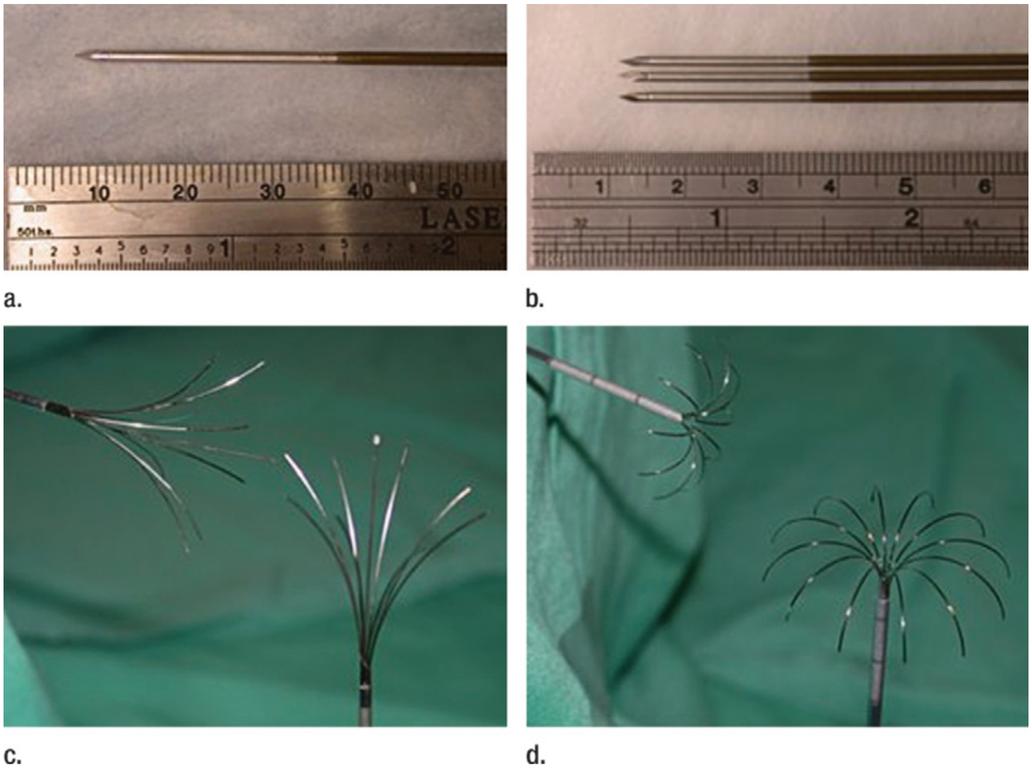

Figure 2.1: RF ablation electrodes in common clinical use: (a) unipolar single and (b) cluster and deployable arrays with (c) star and (d) umbrella shapes [7].

difficulties: the increase of temperature of the antenna itself, partially solved by the use of cooling gases, and the shape of the ablated area shape as the result of the less heating of antenna in its proximal tract for which the ablation becomes teardrop-shaped).

2.3 High-intensity focused ultrasound ablation

The ultrasound waves are generated by a piezoelectric source and focused with a reflector on the target area. The waves are transmitted to the skin of the patient through degassed water, whose acoustic properties are similar to those of the human tissues. The waves are converged and thus deliver high power to a small portion of tissue, causing cytotoxic heating. The entire operation is very slow because it consists of the overlapping of many HIFU ablated small areas.

The main advantage is the complete non-invasiveness of the treatment: the source and the focalizing reflector are external.

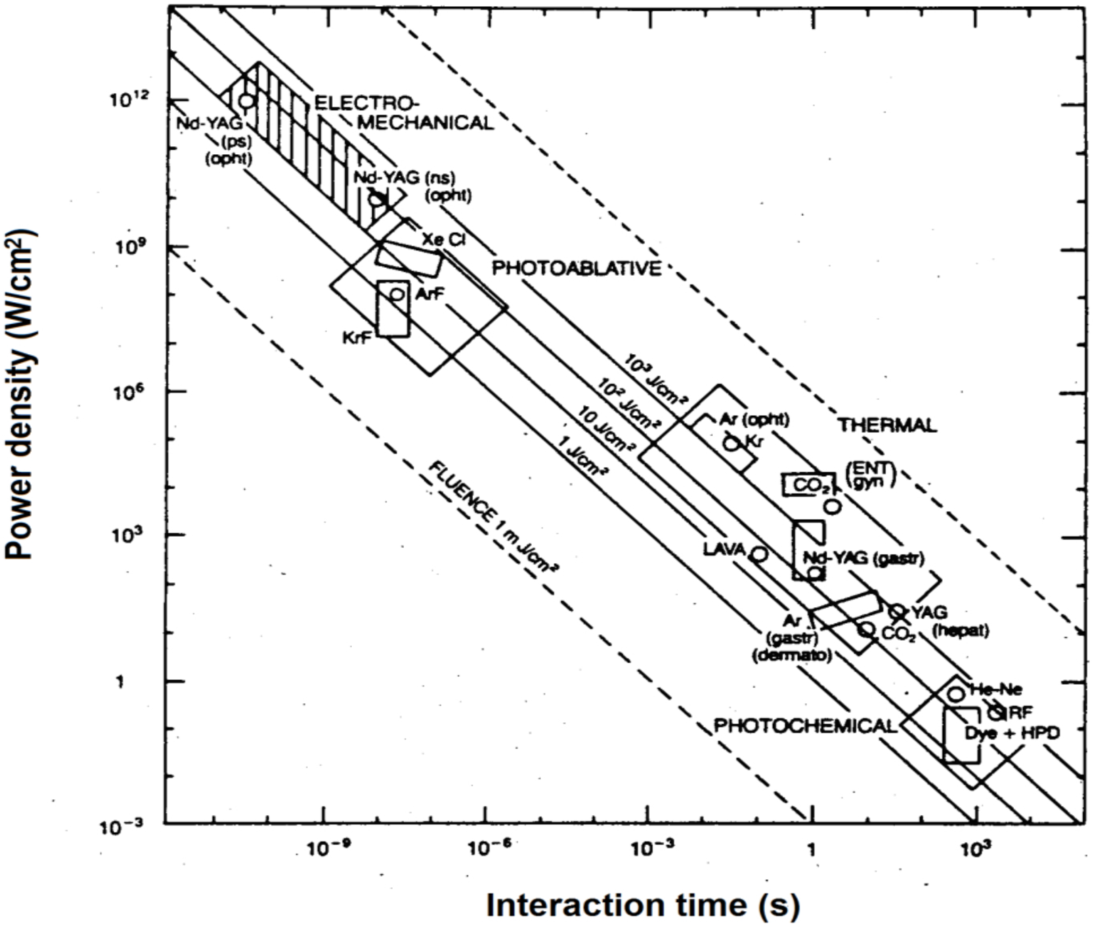

Figure 2.2: Medical laser interaction map [11].

2.4 Laser ablation

The laser ablation is the most recent thermal treatment technique and exploits the laser capability to concentrate high power radiations in a small solid angle [11]. Light propagating in the tissue undergoes scattering and absorbing phenomena; the fraction absorbed is converted into heat, which in turn causes the denaturation of the proteins and thus the cellular necrosis [13]. Different emission wavelengths from visible to infrared) and operating regimes (Continuous or Pulsed Wave, CW or PW) can be used depending on the required penetration depth and, in general, on the tumour location and characteristics. The typical configuration makes use of Laser Diodes (LD) emitting at about 1 µm, operated in CW, with a maximum power in the order of 5 W to 10 W.

The interaction of laser light with organic tissues for different combinations of power density and treatment time is described in Fig. 2.2.

The optical tissue response is given by Lambert-Beer's Law, which describes the exponential decrease of the light intensity $E(z)$ as a function of the depth in the tissue, due to both scattering and absorption:

$$E\left(z\right) = \left(1 - r_{\mathrm{s}}\right) F_{\mathrm{sc}} E_0 \; \mathrm{e}^{-\mu_{\mathrm{eff}} z} \tag{2.1}$$

where:

- r_{s} is the Fresnel reflection coefficient for the normal light ($\simeq 2\%$ in the considered cases) at the interface between air and tissue [11];
- F_{sc} takes into account of the scattering phenomenon;
- z is the penetration depth;
- $\mu_{\mathrm{eff}} = \mu_{\mathrm{a}} + \mu_{\mathrm{s}}$ is an effective absorption coefficient that combines the scattering and absorption phenomena at the wavelength λ of the laser radiation.

The main component of biological tissue is water, which has high absorption values in the infra-red (IR) spectrum (Fig. 2.3).

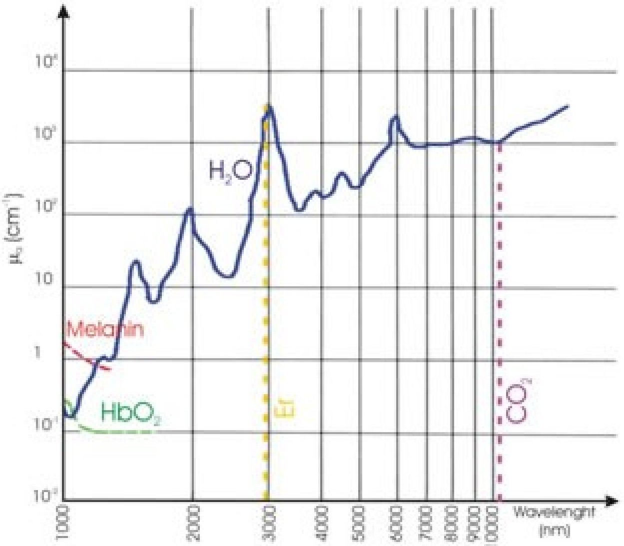

Figure 2.3: Absorption coefficient of water as a function of the wavelength [15].

In LA, a compromise in the absorption must be made since a high absorption value shortens the treatment but also reduces the penetration depth. For this reason, in many practical cases a wavelength around 1 µm is chosen.

The laser-tissue interactions can be subdivided in four classes:

1. Photochemical interaction. As shown in Fig. 2.2, it occurs with high duration and low-energy exposures. The absorbed energy is converted into structural modification of the pre-existing molecules or is employed in chemical reaction to produce new substances.

2. Photothermal interaction. Most laser surgical applications rely on this regime in which the absorbed energy is converted into heat and the tissue damage is function of the time exposure, as reported in Tab. 2.1.

3. Photo-ablative interaction. It requires high power density, typical of very short pulsed laser radiation. It leads to the destruction of macro-molecules inside the tissue. The ablation phenomenon is characterised by the so-called ablation threshold that defines the minimum irradiation removing the treated tissue. Over this value the ablation effect becomes proportional to the total thermal dose collected in the target area.

4. Electro-mechanical interaction. It manifests as pressure pulses propagating near the real target area. It needs high intensity laser in order to generate collapse in the material.

Photothermal and photo-ablative effects are the results of many consolidated thermal techniques in medical surgery.

The most common laser used in LA are Nd:YAG (neodymium-doped yttrium aluminium garnet) and semiconductor diodes, which are the most effective for deep penetration and for producing haemostasis [14].

The main advantage of LA is the complete electromagnetic compatibility, allowing the performing of the procedure under MRI guidance. The laser light is highly energetic, the heat is rapidly produced in the nearby of the emitting tip. The effective heat spread around the applicator for about 1 cm (in diameter) [7]. But the attenuation of the laser light is substantial if the tissue has been dehydrated or charred, resulting in low energy delivered. To avoid the charring of the tissue, the laser applicator has a cooling system and the power of the emitter system is controlled.

Optimal LA outcomes require an accurate real-time monitoring of the induced temperature since the laser parameters should be adjusted to be above the cytotoxic level in the entire tumour mass, but below the carbonization temperature. This Master's Thesis project is mainly concerns with the monitoring of the temperature during LA treatments.

Chapter 3

Introduction to Lasers and Optical Fibres

In this chapter a short introduction to lasers and optical fibres is given. The temperature sensor studied and compared in this project thesis are optical fibres. Here is given a brief introduction to lasers and optical fibres.

3.1 Laser

LASER is the acronym of Light Amplification by Stimulated Emission of Radiation [16].
The basic elements of a traditional laser device are: active material, pumping device and optical resonator.
The active material is an amplifier of photons and is active when is excited, it is where the stimulated emission of photons happens.
The pumping device is the energy supply for the active material to photon amplification, it emits a particular radiation for the phenomenon.
The optical resonator is made of two mirrors: the totally reflective mirror reflects the radiation inside the active material; the partially reflective mirror transmits part of the photons outside the active material.

3.1.1 Laser diode

The innovative lasers work using a semiconductor diode instead of the active material. Thus there are not the population inversion phenomenon and the level-lasers distinctions.
The key component is the semiconductor diode: a LED (Laser Emitting Diode) emitting a coherent light.
The structure of a diode is based on a semiconductor crystal differently doped in two regions. The positive side, labeled p-region, is poor in electrons, whereas the negative side, n-region, is rich in negative charges. The interface is the p-n junction.
The main property of a diode is to allow the electrons flow only from the n-region to the p-region (direct polarization) when a voltage is applied (p connected to V^+; n connected to V^-). When a vacation and en electron recombine, the result is a photon-like energy emitted.

The laser diode consists in a multi-layer structure (Fig. 3.1), each layer is different in doping and composition. The region in which the recombining process acts is a thin layer. The spontaneous recombining process is, therefore, not sufficient to obtain a laser light.
The pumping mechanism is obtained applying a current flowing in the thin active layer of the diode. The recombination stimulates another photon able to recombine and the process continues. This is the stimulated emission phenomenon inside the laser diode.
The stimulated photons are at the same frequency, polarization and phase of the originating recombined photon. The gain in wavelength increases.
As in the traditional laser with active material, the optical laser cavity amplifies the laser radiation with its reflective surfaces and, if the gain is more than the losses, the laser radiation is emitted.
The main advantages of a laser diode are the high gain, the miniaturisation even tough the emitted power is oh hundred of Watt.
The dimensions allow the laser diode to be employed in the medical field.

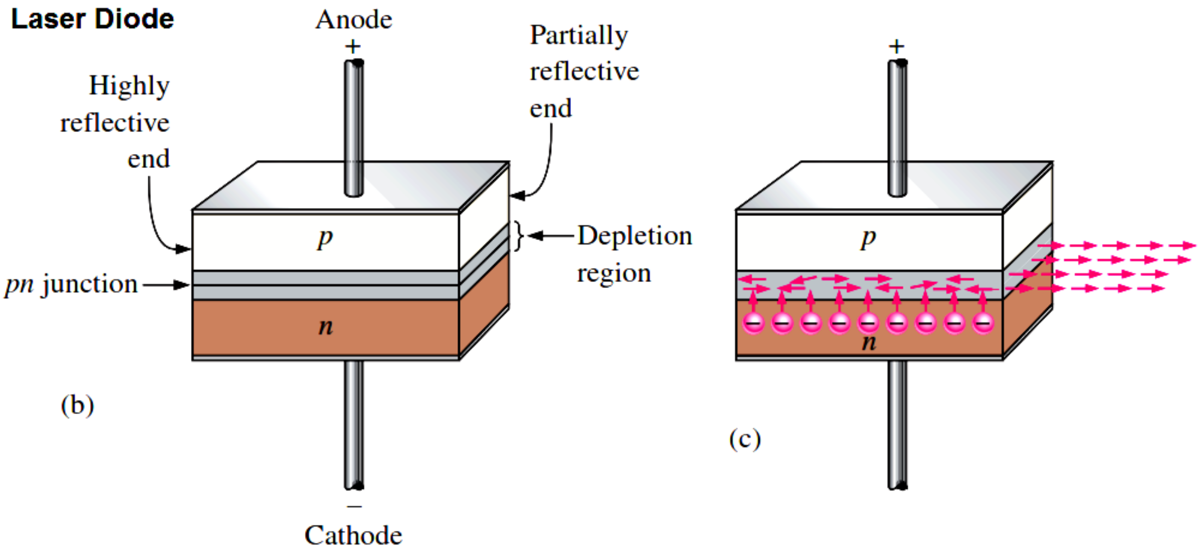

Figure 3.1: Scheme of a laser diode [17].

In this project, the laser diode is employed in the last experimental activity, the ablation of *ex-vivo* bovine liver.
In biomedical application, the laser operation is determined by the desired thermal effect. The continuous wave emission, the generated heat is spread all over the tissue, leading to a high treated area with a uniform overall temperature.
On the contrary, if the aim is to heat and damage a specific small area, the pulsed wave emission is the most appropriate. The chosen wavelength has to be highly absorbed by the water present in the tissue, in order to limit the heat spreading. The pulsing mode generates fast tissue heating and during the time interval in which the laser radiation is not emitted,

the heat is transferred to the close portion of tissue. The consequence is a small treated area and less energy delivered in the ablative process.

3.2 Optical fibres

The optical fibres are concentric layers of silica glass or plastic, guiding the light in their inner layer.

The main structure is composed of an internal *core*, covered by the *cladding*, they are responsible for the travelling of the light in the fibre. The external layers are polymeric and have protective function (Fig. 3.2).

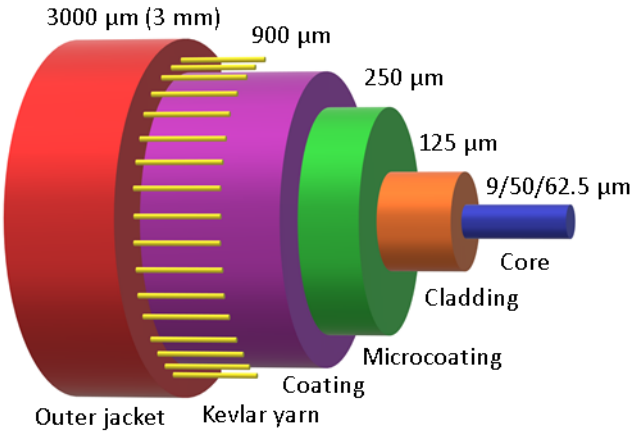

Figure 3.2: Scheme of the structure of an optical fibre.

The property of the optical fibre is to guide the light for long distances thanks to the variation of refractive property of the glass, according to the Snell's law. In fact, when the light travels from the vacuum to a medium, its velocity is slowed with a factor n, the so-called refractive index. The light inside the optical fibre is guided in the core, the inner layer. It is confined in the core because the cladding has a smaller refractive index, and thus, the incident angle is larger than the critical angle θ_C, leading to total internal reflection of the light.

The numerical aperture is an important parameter defined by the product of the refractive index of the eternal layer with the sine of the acceptance angle θ_a, the maximum angle of the entering rays to be guided inside the core. The numerical aperture is the width of the beam possible to be captured by the fibre.

The light travels in the optical fibre if at the air-glass interface it incides with an angle less than θ_a and if the incident angle at the boundary core-cladding is more than θ_C (Fig. 3.3).

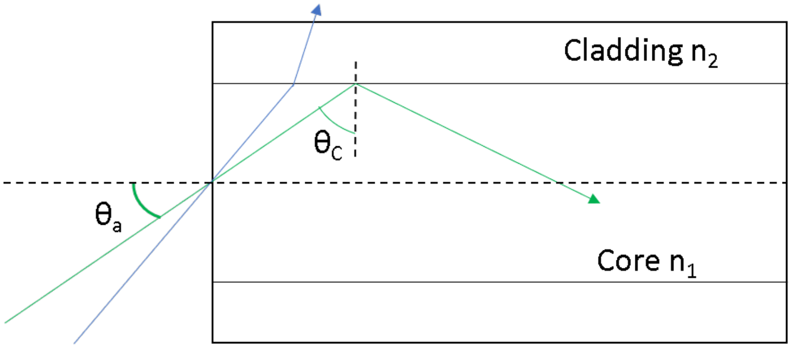

Figure 3.3: Propagation of the light in the optical fibre. If the incidence angle is smaller than the acceptance angle θ_a the light enters the core, it is propagates if the angle on incidence at the limit with the cladding is greater than the critic angle θ_C.

The light undergoes to attenuation phenomena due either to intrinsic or to extrinsic causes.
The intrinsic causes of attenuation are the phenomenon of absorption and scattering.
The material of the fibre presents some impurities causing absorption of the light. The silica glass (SiO_2) has attenuation coefficient dependent on the wavelength.
The scattering is interesting for this study. It belongs to the wide class of the interactions between matter and radiation. It is the deflection (change in trajectory) of the radiation due to the collision with the particles of the matter (tissue, for the topic of this work).
It consists in the interaction of the travelling photon with a particle, this leads to the polarization of the cloud of electrons raising the atom to a higher energy for a short time. The atom then returns to the ground state and frees a photon. According to the energy of the reemitted photon, there are elastic or inelastic scattering phenomena.

- In elastic scattering, the total kinetic energy is conserved and the reemitted radiation has the same wavelength of the incident radiation but the direction of propagation of the incident radiation is modified.

  There are two elastic scattering phenomena:

  - Rayleigh scattering: it occurs if the scattering particle is smaller than the wavelength of the incident radiation. The dispersion of the light after the collision is isotropic (any direction) and the coefficient of diffusion, indicating the amount of scattering, is inversely proportional to the fourth power of the incident wavelength, leading to declare that the shorter the wavelength the more the scattering.

    $$k_s \propto \frac{2\pi}{\lambda^4} R_p \tag{3.1}$$

    Where R_p is the radius of the scattering particle;

    λ is the wavelength of the incident radiation.

  - Mie scattering: it occurs if the scattering particle is larger or of the same order of magnitude of the wavelength of the incident radiation. The consequence of this kind of scattering is the anisotropic dispersion of the light, in fact the scattered light has higher intensity towards the direction of the propagation of incident light.

    The different effects of the two types of elastic scattering are represented in Fig. 3.4.

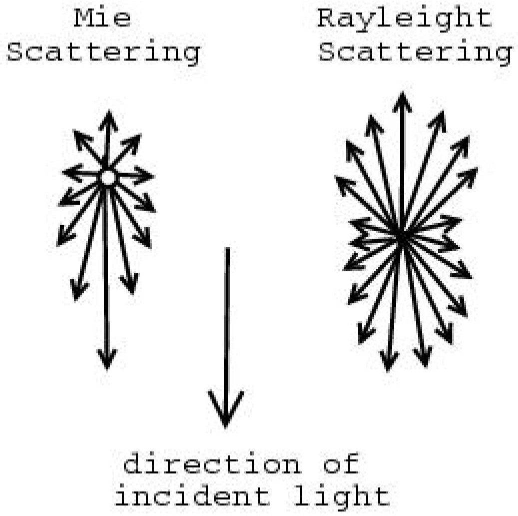

Figure 3.4: Types of elastic scattering [18].

- The main inelastic scattering is the Raman scattering. The feature of this scattering is the different wavelength of the reemitted radiation, after the collision, due to the change of vibrational energy of the molecule.
  The reemitted photon can have low energy (and propagates at longer wavelength) if after the excited state comes back to a higher energy level than the ground state. This type of anelastic scattering is named Raman-Stokes scattering.
  On the contrary the emitted photon can reach a lower-energy state than the ground state, increasing its energy at propagating at a shorter wavelength (anti-Raman-Stokes scattering).
  Fig. 3.5 explains this phenomenon, comparing elastic and inelastic scatterings.

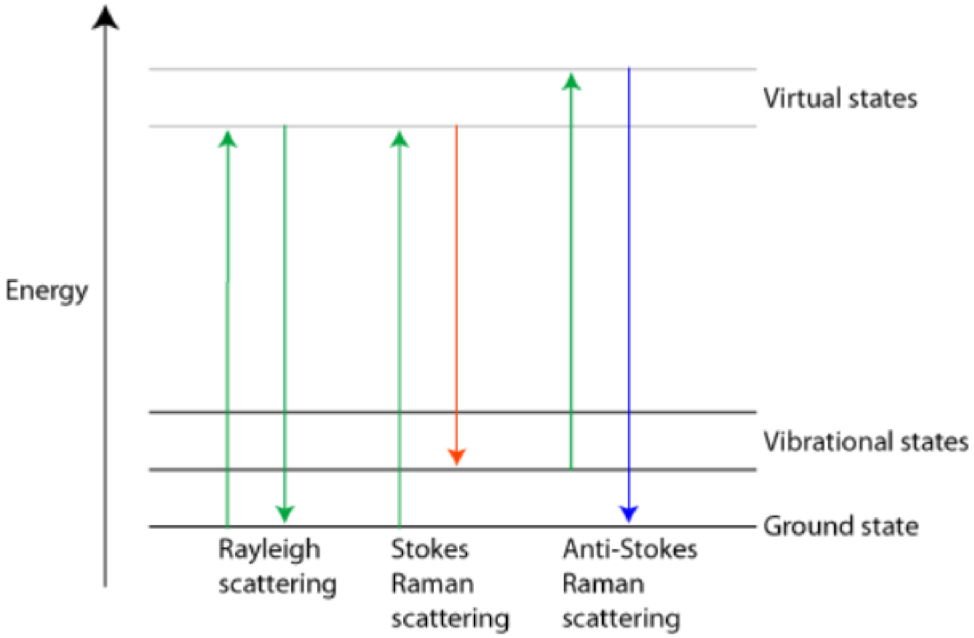

Figure 3.5: Comparing elastic and inelastic scatterings [19].

In the optical fibres the Rayleigh scattering has an important effect, attenuating the propagated signal. It is a random event as much as its cause: the presence of inhomogeneities in the glass (of the same order of magnitude of the wavelength). The consequence is a local fluctuation of the refractive index in the core or at the core-cladding interface.

The temperature produces a change in the Rayleigh scattering and the measure of the reflected signal is indicative of the temperature variation sensed by the fibre [20].

Chapter 4

Fibre Bragg Gratings (FBGs)

The *fiber Bragg gratings (FBGs)* are in-fibre components. This device can perform reflection and filtering functions with high efficiency, and this fact made them become rapidly employed in many fields of applications.
It consists of a "*periodic modulation of the index of refraction along the fibre core*" [21].

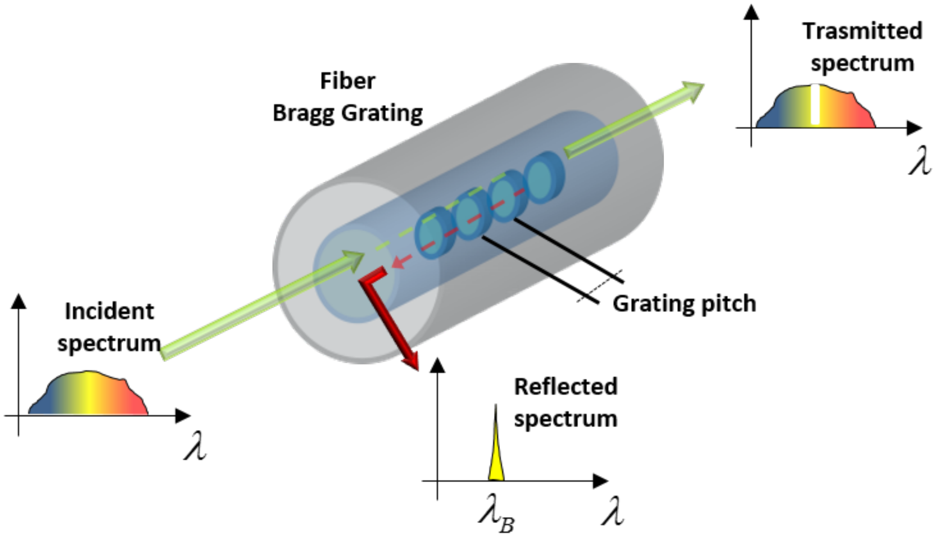

Figure 4.1: Fibre Bragg gratings [22].

The characteristic parameter of an FBG is the so-called *Bragg wavelength*:

$$\lambda_B = 2n_{eff}\Lambda \tag{4.1}$$

Where n_{eff} is the effective refractive index of the core;
Λ is the periodicity of the gratings.

The periodicity of the FBG is influenced on the effects of temperature (ΔT) and strain (ε), leading to a shift in the reflected wavelength by the grating ($\Delta\ \lambda$).
The variation of the Bragg wavelength with respect to stain and temperature is:

$$\begin{aligned} d\lambda_B = \left[\frac{\delta}{\delta\varepsilon} 2\ n_{eff}\Lambda\right] d\varepsilon + \left[\frac{\delta}{\delta T} 2\ n_{eff}\Lambda\right] dT = \\ = \left[2n_{eff}\frac{\delta\Lambda}{\delta\varepsilon} + 2\Lambda\frac{\delta n_{eff}}{\delta\varepsilon}\right] d\varepsilon + \left[2n_{eff}\frac{\delta\Lambda}{\delta T} + 2\Lambda\frac{\delta n_{eff}}{\delta T}\right] dT \end{aligned} \tag{4.2}$$

The relative shift in wavelength is described by the following equation, using the definition of Bragg wavelength 4.1:

$$\frac{d\lambda_B}{\lambda_B} = \left[\frac{1}{\Lambda}\frac{\delta\Lambda}{\delta\varepsilon} + \frac{1}{n_{eff}}\frac{\delta n_{eff}}{\delta\varepsilon}\right] d\varepsilon + \left[\frac{1}{\Lambda}\frac{\delta\Lambda}{\delta T} + \frac{1}{n_{eff}}\frac{\delta n_{eff}}{\delta T}\right] dT \tag{4.3}$$

The right-term of the equation 4.3 is the sum of the effect of the strain with the effect of the temperature variation on the relative Bragg wavelength.
The strain introduces two modifications on the FBG: varies the periodicity Λ and, due to the photo-elastic effect, changes the value of $\mathrm{n_{eff}}$.
The characteristic coefficient of the photo-elastic effect, regarding the incidence of a radiation on a mechanical stressed surface, is $p_e \sim 0.22\cdot\ 10^6\ \frac{1}{\mu\ \varepsilon}$ for silica fibres.
The equation of the macroscopic variation of Bragg wavelength is:

$$\Delta\lambda_B = K_\varepsilon \cdot \varepsilon + K_T \cdot T \tag{4.4}$$

Where, for silica optical fibres,
$K_\varepsilon\ = 1\,\mathrm{pm}/\mu\varepsilon$ is the strain sensitivity;
$K_T = 10\,\mathrm{pm}/^\circ\mathrm{C}$ is the temperature sensitivity.

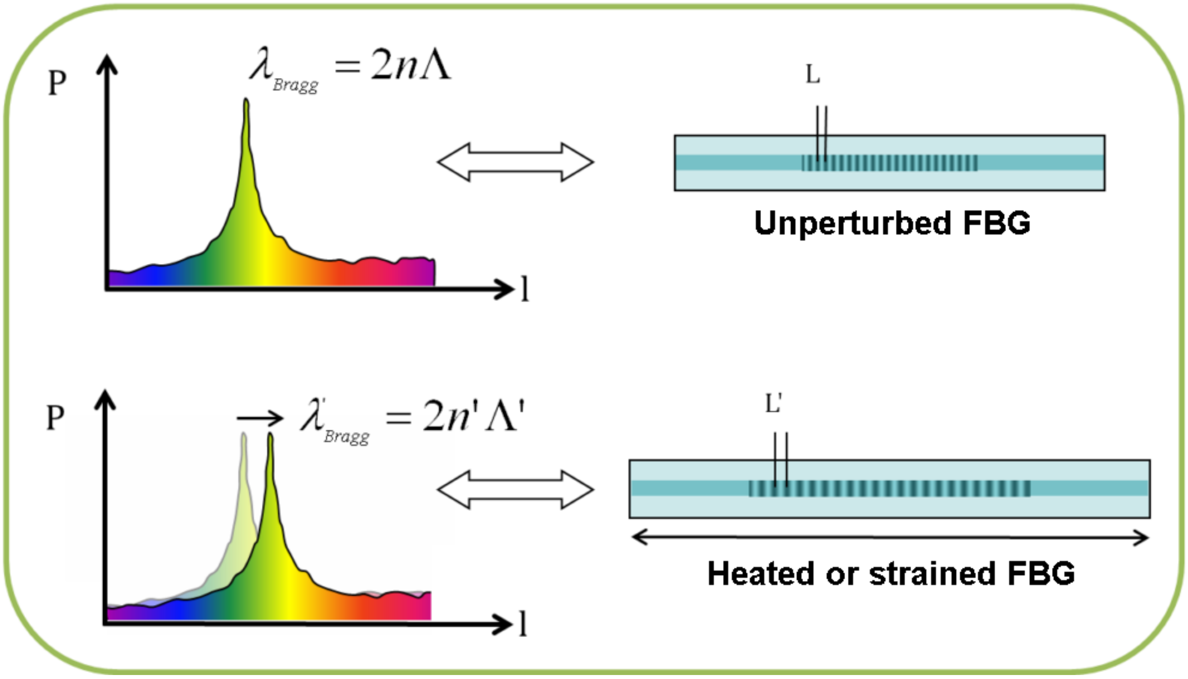

Figure 4.2: Effect of external perturbation of the FBG [23].

4.1 Manufacture

FBG are ″written″ inside the optical fibres creating a periodic variation of the core refractive index. There are three writing techniques:

- Interference
  This lithographic method exploits the interference between two UV beams. The interference creates a distribution of intensity in line with a periodic pattern. The doped silica glass of the core changes its refractive index following the intensity of the light. The Bragg wavelength depends on the periodic pattern of interference and on the angle on incidence of the laser light.

- Photomask
  The FBG is ″printed″ in the core through a mask placed between the UV-laser source and the core.
  This technique is preferable to use for chirped FBGs.

- Poin-by-point
  The FBG is ″written″ inside the core (non-doped) with a pulsed laser beam. The beam is very high in energy and is high in both spatial both temporal resolutions, due to very

short pulses (10^{-15} s). The instrument used is mainly the femtosecond laser.

4.2 FBG structures

Two parameters describe the FBG structure: the refractive index and the periodicity of the grating.
According to the periodicity parameter, the main types of FBG structure are:

- Uniform: the periodicity is regular; thus, the Bragg wavelength is constant;
- Chirped: the periodicity varies in linear fashion;
- Tilted: the periodicity is constant but the periodic modulation of the refractive index is not perpendicular to the core axis but presents a slope angle;
- Superstructure: FBG-array with different Bragg wavelength.

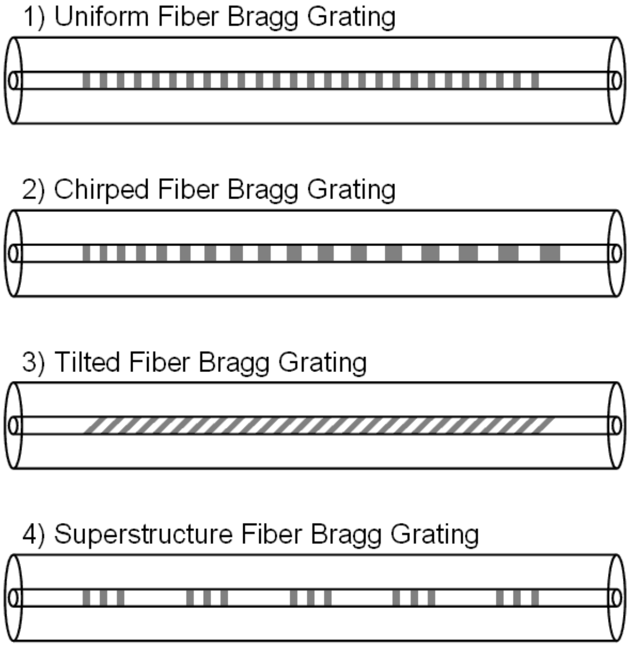

Figure 4.3: Principal types of FBG structures [24].

While the refractive index parameter classifies the FBGs as:

- Uniform: the refractive index is the same for each line of the grating;

- Gaussian-apodized: the envelop of the refractive indices of each line along the longitudinal core axis is gaussian-shaped. The apodization concerns to the fact that the external lines of the grating have almost no-difference from the refractive index of the core;
- Raised cosine-apodized: the envelop of the refractive index of the grating is both higher and lower than the core refractive index;
- Discrete phase shift: the profile of the refractive index of the grating does not presents the same phase along the axis of the core. This changes in phase cause a specular shape of the reflection with the axis of symmetry corresponding to the Bragg wavelength of the grating.

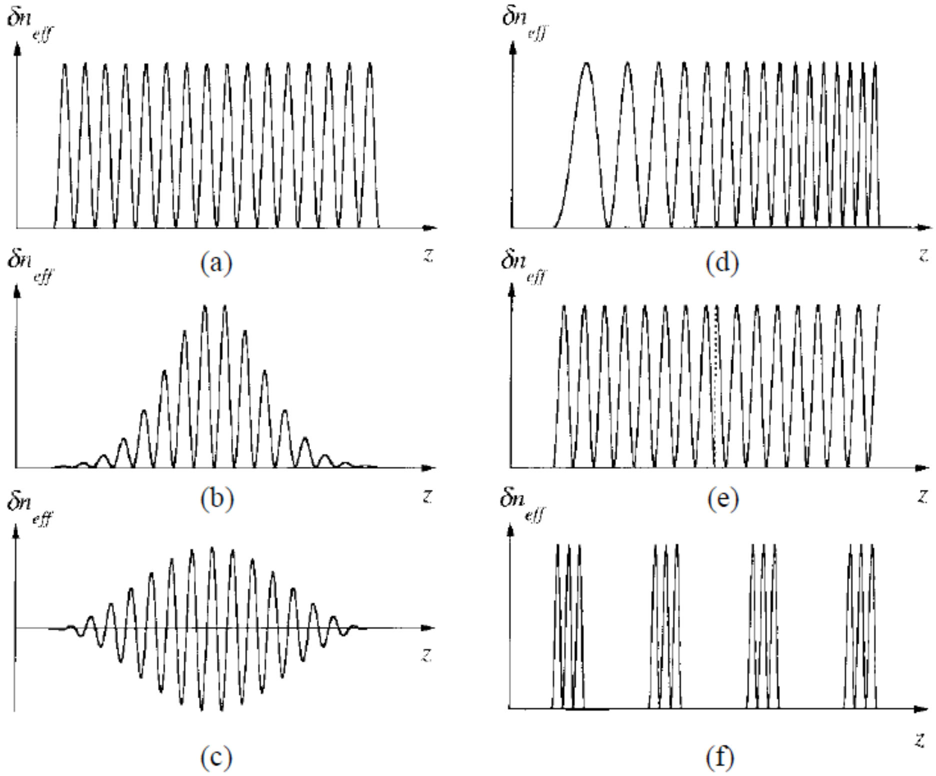

Figure 4.4: Variation of the refractive index in the FBG depending on the type of FBG. (a) Uniform FBG; (b) Gaussian-apodized; (c) raised cosine apodized FBG; (d) chirped FBG; (e) discrete phase shift; (f) superstructure [25].

Chapter 5

Optical interrogators

The temperature changes cause a variation of the wavelength of the reflected light and in the Rayleigh backscatter by the optical fibre sensors. The instruments used to detect the wavelength and the intensity of this reflection are named optical interrogators.
In this project two optical interrogators have been used: a FBG sensing system and an optical backscatter reflectometer based on the optical frequency domain reflectometry.

5.1 FBG sensing system

This type of instrument acquires the reflected signal by the FBG (or FBGs) inscribed inside the fibre core. The signal from the FBGs is the reflected radiation at the Bragg wavelength. The monitoring of the FBGs can be dynamic, allowing the real-time reading of the changes in Bragg wavelength.
The data are acquired simultaneously for all the FBGs written in the connected optical fibre. During the process of measurement, the instrument measures the wavelength of the reflected light reaching the detectors (the technique of the system is named *wavelength division multiplexing* due to the fact that it refers to wavelength instead of frequency, which is more usual for non-optical systems.
The main advantage in the use of FBGs is the fact that all the thermal variation and/or strain phenomena occurring have effect only on the Bragg wavelength, the central peak wavelength. For this reason, the optical interrogator system has to detect a single wavelength. This advantage can become a problem in case the noise does not submerge the signal (reducing dramatically the Signal to Noise Ratio - SNR).
The superstructure of FBGs is an array of FBGs and it can be entirely interrogated in a single acquisition, due to the different Bragg wavelengths of the FBGs, performing a quasi-distributed measurement.
The basic component elements of an FBG optical interrogator are a light source and an optical spectrum analyser for the light reflected by the FBG(s).
There are two different light sources available:

- Broadband light source The broadband light source, e.g. a super-luminescent LED

(SLED), goes in input to an optical circulator and reaches the optical fibre containing the FBGs under test. The optical circulator prevents the light from travelling in the same direction with opposite verse in the same arm. In this architecture, the optical circulator also guides the light reflected by the FBGs to a tuneable filter. This, working as a pass-band filter, sweeps all the wavelengths and the filtered signal goes to an optical detector (photodiode) and then to a trans-impedance amplifier. The optical power gets converted into analogic voltage.
The peculiarity of this kind of source is the tuneable filter, embodied by an interferometer.

- Tuneable laser This source is made with a narrow-band laser, swept over the selected range of wavelengths to perform the interrogation. As a difference from the previous type of source the reflected light from the FBGs (occurring when the laser wavelength coincides with the Bragg wavelength) does not need to be filtered and reaches directly the photodiode and then undergoes the conversion into analogic voltage.
  In this way, the spectral filtering of the light is executed before the light propagates into the FBGs. Moreover, the laser light is more constant in intensity than the SLED source, leading to a higher SNR.

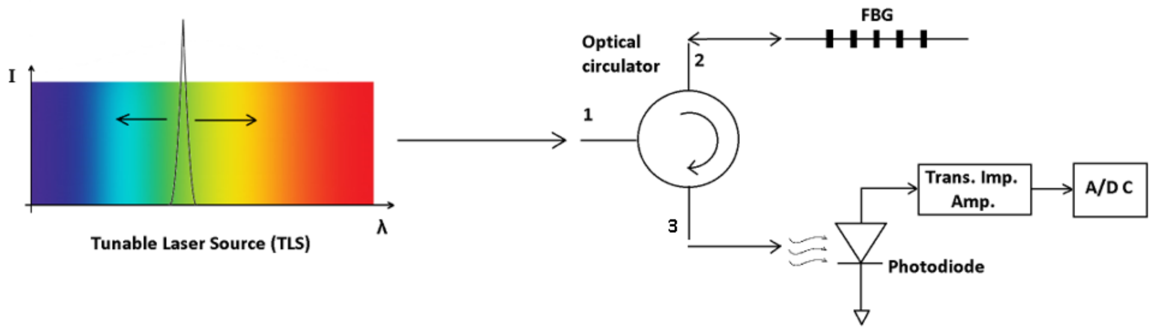

Figure 5.1: Tuneable laser FBG optical interrogator.

5.1.1 MICRON OPTICS HYPERION si155

The optical fibres in which FBG arrays have been written with the femtosecond laser have been interrogated with an optical interrogator provided with a tuneable laser source, Micron Optics HYPERION si155, by Luna Technologies®.
The technical specifications are:

- wavelength range: 1500 nm – 1600 nm;
- wavelength resolution: 10 pm;
- maximum acquisition rate: 1 kHz for peak detection, 10 Hz for spectrum detection;
- 4 parallel channels;
- dimension typical of the laboratory instruments (20.6 cm × 27.4 cm × 7.9 cm / 3.0 kg).

The instrument requires an Ethernet connection to be remotely controlled. The user interface is a free software, *ENLIGHT Sensing Analysis Software*.
The software allows the contemporary graphical visualization of the signals from the four channels and also the list of the peaks detected in the channels. The functionalities of this software allows the user to change the acquisition rate, save data acquisitions, to manage the sensors and to set alarms related to value of selected parameters (Fig. 5.2).

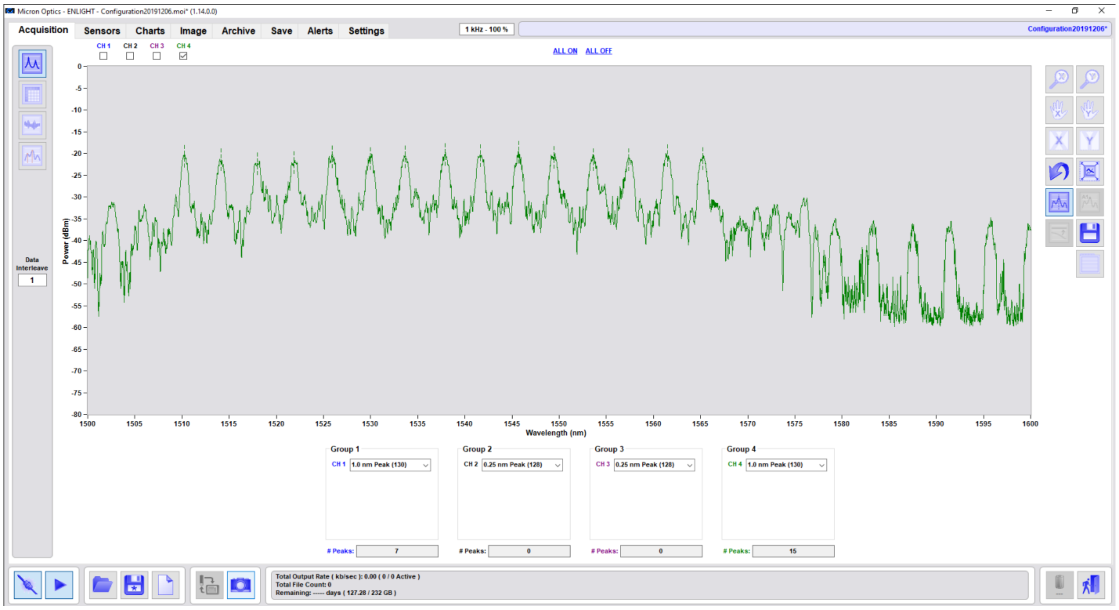

1 kHz - 100 %

CH 1 ☐ CH 2 ☐ CH 3 ☐ CH 4 ☑

Data Interleave: 1

Group 1: CH 1 1.0 nm Peak (130); # Peaks: 7

Group 2: CH 2 0.25 nm Peak (128); # Peaks: 0

Group 3: CH 3 0.25 nm Peak (128); # Peaks: 0

Group 4: CH 4 1.0 nm Peak (130); # Peaks: 15

```
Total Output Rate ( kb/sec ): 0.00 ( 0 / 0 Active )
Total File Count: 0
Remaining: ----- days ( 127.28 / 232 GB )
```

Figure 5.2: User interface of the ENLIGHT Sensing Analysis Software. Only the channel 4 is selected and shown but the channels detecting data are 1 and 4 as seen in the boxes indicating the numbers of peaks.

The instrument allows the automatic detection of the Bragg peak wavelengths of each FBG. The data processing in the instrument itself is contemporary with the data acquisition, and this leads to a real-time monitoring of the changes due to temperature change or strain phenomena.
The signal gets initially filtered, for noise reduction, then undergoes a further filtering process with a *derivative filter*, whose output is the derivative of the signal profile.

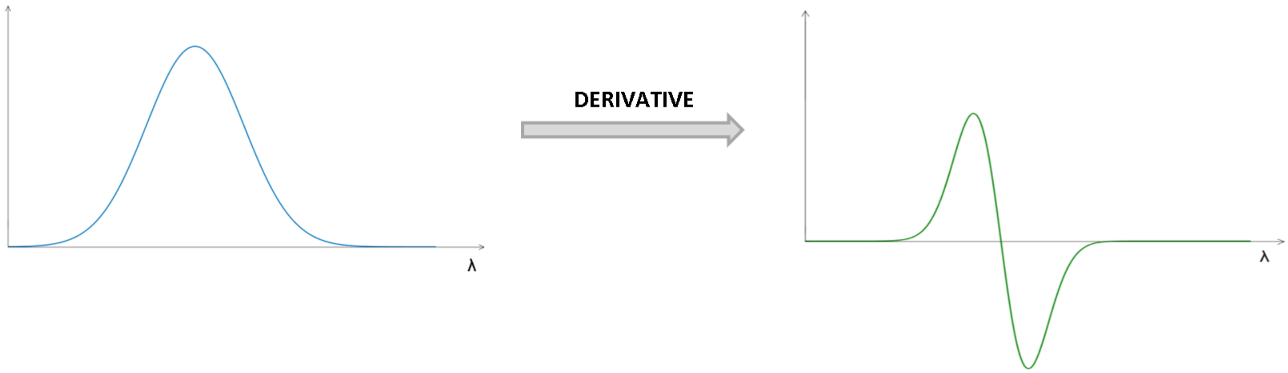

Figure 5.3: Filtering process with a derivative filter.

The peak is detected with the *zero-crossing* method, with a variation due to the non-ideal profile of the signal. In fact, the filtering process causes the presence of more zeros in the signal than they are in the reality. To solve this problem, it is necessary to set a threshold value to detect the wavelength interval of the points of the signal beginning from the first higher than the threshold. The user sets the threshold (Fig. 5.2, for the visualized channel, the threshold selected is 1 nm of width of the peak, rule 130) according to the purpose of the analysis, e.g. considering only the primary lobe of a non-apodized FBG.
The algorithm now searches for the zero of the real peak, which is the first detected.

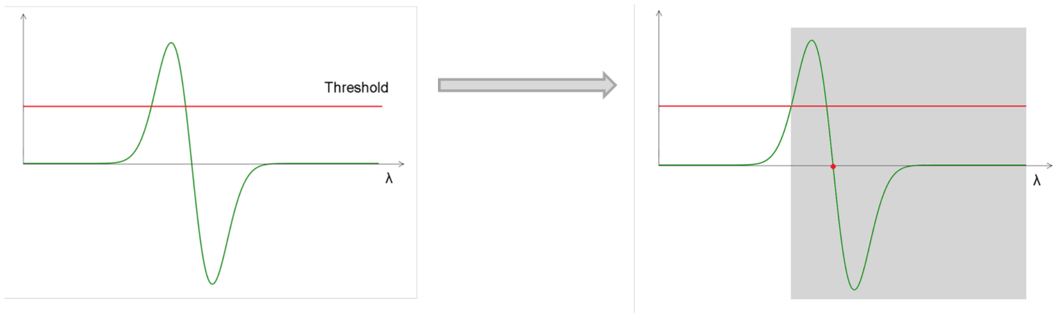

Figure 5.4: Zero-crossing method application.

5.2 Optical frequency domain reflectometer

Reflectometry in the frequency domain is more convenient type of reflectometer method available.
The coherent OFDR (C-OFDR) is the type of OFDR used in this Master's Thesis project.
The C-OFDR works thanks to a swept Tuneable Laser Source (TLS). Then the signal is split in two paths by a coupler: the first arm of the interferometer is the reference signal and the other goes to the optical fibre to investigate. The signal returning due to reflective elements in the fibre under test and the reference signal totally reflected by a mirror are mixed, producing an interferent signal. The interference presents beat frequencies, appearing as peaks after the Fourier transform of the interferent signal.
The frequency sweep of the TLS is linear, allowing to measure the distance of each beat frequency which means the distance of each reflective element in the tested optical fibre.
Moreover, the reflectivity of each reflection origin is obtained as the squared amplitude of the signal at each beat frequency.
The advantage of the C-OFDR is the possibility to measure of a large range of amplitude, because the discrete photocurrent detected is proportional to the square root of the reflected optical power.
Finally, unlike OTDR, the dead zone in these measurements is not present because the detector never saturates. The only disadvantage that is worth noting is the limit in the distance to measure, due to the coherence length of the TLS.

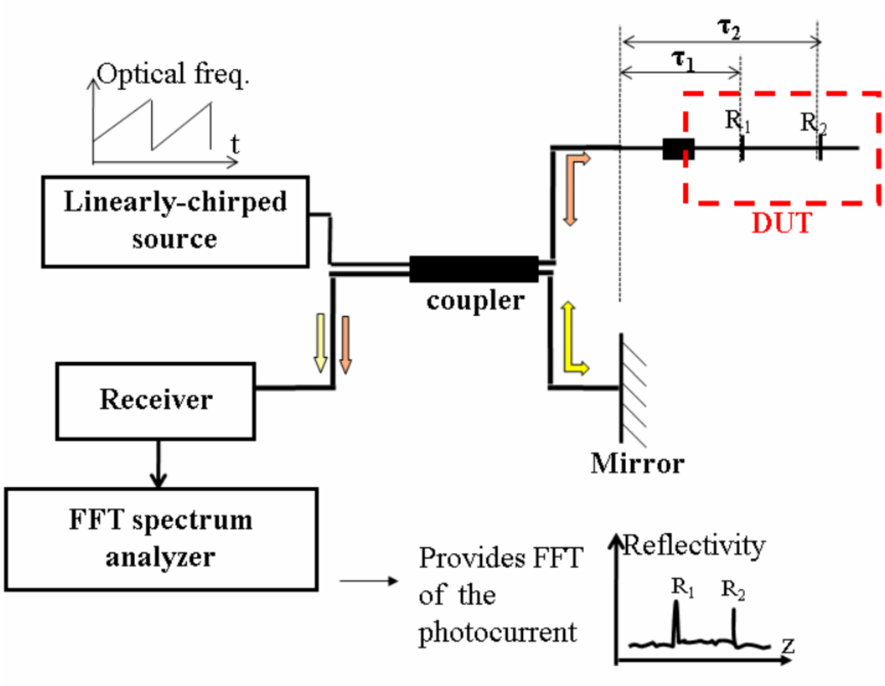

Figure 5.5: Scheme of an OFDR device.

The OFDR is more recent and more preferable over the optical time domain reflectometry (OTDR).

Briefly, an OTDR works with the same physical principles as a radar.

The physical phenomena exploited are the Rayleigh backscattering, as in OFRD, but also the Fresnel reflection. Both of them are generated by a sharp change in the index of reflection inside the optical fibre. The Fresnel reflection is due also to optical connectors and to the end of the fibre (interface silica – glass). The OTDR measures the reflected power and the time delay between the injected pulse and the received reflection, the velocity of the light inside the silica core is the ratio between the speed of light and the index of refraction of the silica (1.47). The position of the reflective element is obtained obviously from the equation describing the velocity (distance=velocity · time interval).

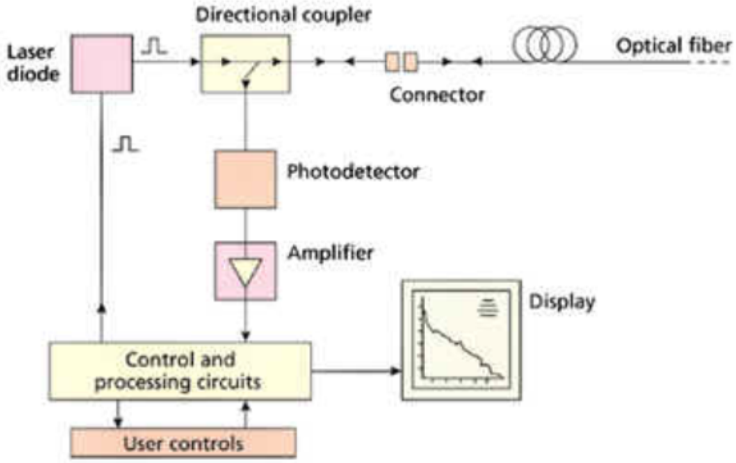

Figure 5.6: Scheme of an OTDR device.

The duration of the pulses from the laser source determines the spatial resolution.
Short pulses increase the spatial resolution but are low in energy, reaching low distances and with low SNR.
On the contrary, longer pulses decrease the spatial resolution and since the energy is high the distance travelled is long and the noise has less effect.
The disadvantage of the OTDR is the dead zone, after each reflective event the detector is momentarily blind to the following events. The detector is a photodiode and needs to recover, the dead zone is short if the impulse is fast and so the recovery time is short. But the consequence is a noisy low-power signal as described above.

5.2.1 Comparison OFDR-OTDR

The difference is that OFDR does not need recovery time and thus, is not affected by the dead zone.

Moreover, the measurements are higher in resolution and in SNR. The noise at the optical detector is proportional to the detector bandwidth, in OFDR the bandwidth is proportional to the resolution in space, a great advantage over the OTDR in which the inverse proportionality between the spatial resolution and the SNR is a limit.

The reflections can be detected by the OFDR even if they are weak.

5.2.2 LUNA OBR 4600

The distributed optical fibre sensors have been investigated with the Optical Backscatter Reflectometer OBR 4600, by Luna Technologies®.
It is based on optical swept-wavelength interferometry to detect and evaluate even the smallest reflections in the optical fibre under test as a function of length.
The technical specifications for mode with maximum device length of 30 m are:

- wavelength range: 1525 nm – 1610 nm;
- wavelength resolution: 0.02 pm;
- scan time: 2.7 s, 1.3 s in fast scan for 5 nm of wavelength scan range;
  14.2 s, 6.3 s in fast scan for 65 nm of wavelength scan range;
- sampling resolution: 10 µm;
- temperature resolution (distributed sensing mode): ±0.1 °C;
- single channel;
- dimension 36.6 cm × 34.5 cm × 16.5 cm / 11.4 kg.

The instrument is provided with a laptop PC equipped with the OBR control software *OBR V.3*.
The software shows two graphs (Fig. 5.7), the displayed magnitudes are selected from the pull-down menu in the plot title and in lateral boxes parameter are selected.

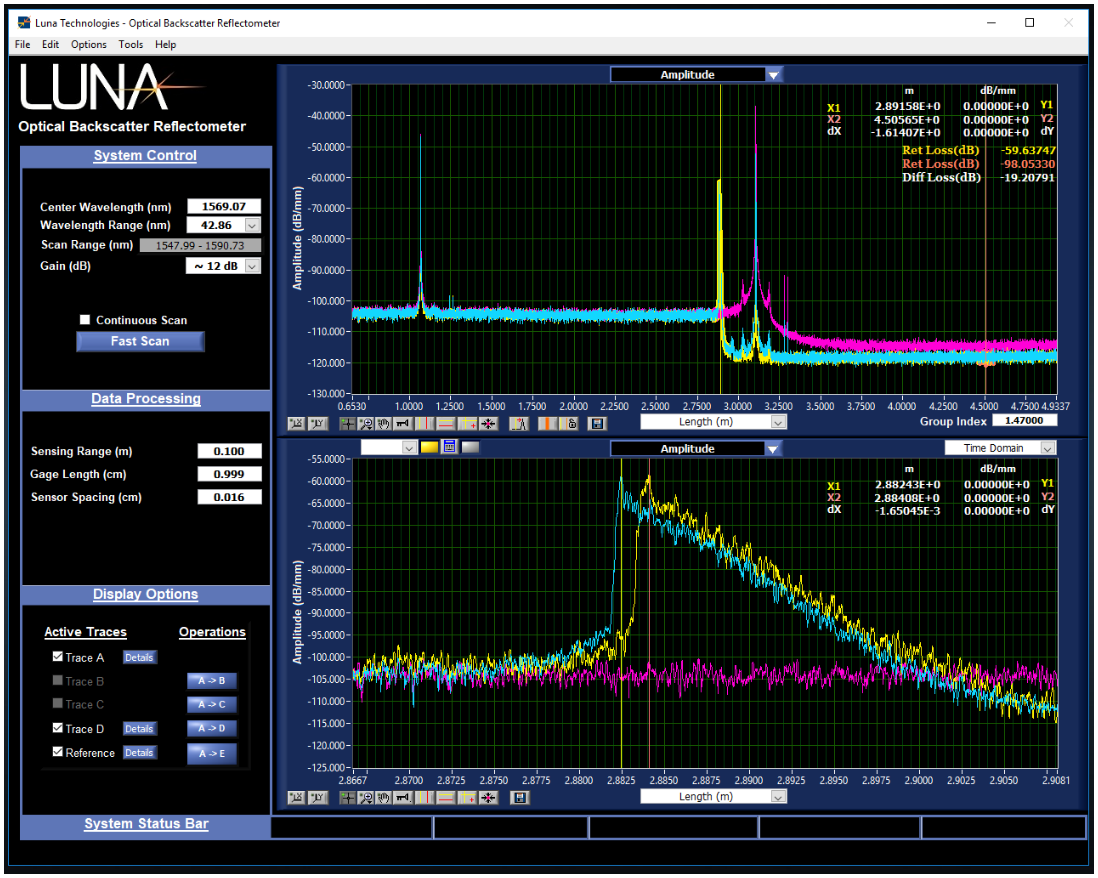

Center Wavelength (nm) 1569.07
Wavelength Range (nm) 42.86
Scan Range (nm) 1547.99 - 1590.73
Gain (dB) ~ 12 dB
☐ Continuous Scan
Fast Scan

Sensing Range (m) 0.100
Gage Length (cm) 0.999
Sensor Spacing (cm) 0.016

☑ Trace A
☐ Trace B
☐ Trace C
☑ Trace D
☑ Reference

	m	dB/mm	
X1	2.89158E+0	0.00000E+0	Y1
X2	4.50565E+0	0.00000E+0	Y2
dX	-1.61407E+0	0.00000E+0	dY

Ret Loss(dB) -59.63747
Ret Loss(dB) -98.05330
Diff Loss(dB) -19.20791

Group Index 1.47000

Time Domain

	m	dB/mm	
X1	2.88243E+0	0.00000E+0	Y1
X2	2.88408E+0	0.00000E+0	Y2
dX	-1.65045E-3	0.00000E+0	dY

Figure 5.7: User interface of the OBR V.3 software.

The upper graph is always displayed, the lower is related only on a specific section of the upper graph, highlighted by the user.
The upper graph automatically displays the amplitude of the backscattered signal in the time domain (or in the length of the DUT), this corresponds to the data acquired by an Optical Time Domain Reflectometer (OTDR). The lower graph can display both time domain and frequency domain quantities.
In the time domain, a peak is detected for each optical interface in the DUT. The time domain can be displayed with the horizontal axis in time (ns) or length (many units). The length axis is useful to locate the reflecting events along the investigated optical fibre.
The frequency domain quantities can be displayed only in the lower graph, for a selected tract of the entire DUT in time domain.

5.2.3 Patent OFDR US 7.515.276 B2

The instrument used to perform distributed temperature acquisitions along the length of a single mode optical fibre SMF-28 is the Luna Technologies® OBR (Optical Back-scatter Reflectometer) [26].

The technology of this instrument is the C-OFDR (Coherent Optical Frequency Domain Reflectometer).

The starting optical signal is generated by a tuneable laser and its optical carrier frequency is swept in time with linearity. This signal divides itself into the two paths of the interferometer, which is the main component of this instrument.

The optical signals from the two arms (the reference and the tested device ones) then recombine at a coupler with interference due to the different length of the paths caused by the presence of backscattering events in the DUT (device under test). The interferent signal reaches the receiver and then is processed with a Fourier Transform, which allows the extraction of the beat frequencies shown as peaks. The correspondence between the beat frequencies and the position of the backscattering event in the DUT can be obtained using a linearly swept optical frequency, the pace of change of the optical frequency determines the proportionality factor.

OFDR is based on the concept that the coherence length of the laser used establishes that the device measured must be comprised in it. The coherence length is the distance within the light is coherent with itself, that means that the phase of the considered wave is known at priori within a resolution in time T. This can be demonstrated splitting the wave into two ways and then recombined before that time T is passed: the wave produced by the interference of the two ones will have known fringes. The ability to predict the interference fringes will decrease with the passing of time after T, until the correlation will be zero when the random part of the phase is greater than 180 degrees.

The coherence length is generally expressed as optical delay, thus using a time unit of measure (ns), and it can be approximately obtained as the inverse of the laser linewidth which is the extension of the spectrum of frequencies at both sides of the central frequency. The unpredictability of the phase of the laser light propagating in the optical fibre after the coherence time, is the motivation to avoid the use of inexpensive laser for interferometry when its paths have larger difference than the coherence time. The length of the reflection path is calculated as the half of the velocity of the light inside the medium multiplied the coherence time: $(l = \frac{c}{n} \cdot t)$.

The inventors of this instrument disproved this assumption and described a technology in which is possible the use of a cost-effective laser to build an OFDR to analyse optical fibre at reflection length longer than the coherent length of the laser itself and obtain high resolution measurements in the interferometric system.

The laser source scans the device under test (DUT), each wavelength has a corresponding coherence length: the length that the laser light runs across with still known a priori phase. The interferometric response of the DUT is obtained by mixing the known a priori phase of the laser with the intensity of the interferometric measurement in the DUT.

The instantaneous optical phase is measured at the same time of the interferometric response of the DUT and it is processed to compensate it and to obtain high-resolution data for a precise section of the DUT length.

The first image is the general scheme of composition of an OFDR system: it has a laser tuned either with the current drive mode of tunability or with the temperature mode regarding the change of temperature of the diode by many Celsius degrees. The tuneable laser linewidth

is less extended than the bandwidth of the electronic components of the circuit to acquire data.
The emitted laser is split between two interferometers: the laser monitor and the DUT ones. The former generates optical signals reaching optical detectors converting the light into electrical signals, then they are digitalized by the circuit of data acquisition which also transmits digital information about the intensity to the data processor which use it to evaluate the phase (also the known a priori phase) of the laser, corresponding to a certain reflection length of the DUT. The second scheme describes both the interferometers. In the laser monitor the light is split again and sent to the two arms of the interferometer: a short reference fibre arm and a longer fibre path, then the optical signals are recombined in a 3x3 optical coupler where the light interferes. The intensity of the interference is detected by the two detectors (for example photodiodes), receiving the in phase and in quadrature measurements from the optical couplers.
In the DUT monitor interferometer the laser light undergoes the same steps as the laser monitor interferometer (splitting, reflection, recombination). The recombined interference signal (it has interference fringes) reaches a polarization beam splitter which separates the light according to its polarization state (P and S), the detectors receives either P or S light intensity.
The data processor calculates the laser phase at a certain length of the DUT using the digitized signals from the laser monitor. This information is then used to compensate the digitized signals coming from the DUT monitor in order to evaluate the interferometric response of the DUT depending on the optical delay (or on the optical length) with high resolution.

The flow charts in Fig. 5.8 subdivides the procedure in steps:

- S1: the laser light sweeps a large interval of frequencies.
- S2: the detectors receive the intensity signals deriving from the interference phenomenon.
- S3: the laser monitor phase is calculated from the conversion of the interference of the light.
- S4: the second derivative of the phase of the laser monitor is obtained filtering the phase data. This step is not mandatory but it is helpful because the second derivative contains the main information and also because it needs a few bits to be represented, important aspect if the processing is executed by an FPGA.
- The phase of the DUT interferometer is calculated as the difference between the phase of the light in the reference arm (short length of travelling) and the phase of the light in the DUT arm (long length of tavelling). This means that the phase of the DUT is the difference between the laser phase and the delayed laser phase itself, provided that the phaser of the light is known. S5: the second derivative of the phase of the light at a certain position in the DUT is extracted using the differences and the delays. Both

of the operations are linear, so they can be executed in any order, but perform the subtraction first is recommended in order to economize the computational resources.

- S6: double integration of the second derivative of the location phase at the DUT position.
- S7: the phase is then converted into the two reference signals (in-phase and quadrature ones) for the laser phase at the considered position on the DUT.
- S8: the reference signals (I and Q) for the laser phase at the position on the DUT are multiplied by the input signals of the interferometer of the DUT. Unless this fact, the phase of the laser is not known at the selected position on the DUT.
- S9: the result of the previous multiplication is filtered with a low-pass filter in order to consider only the information related to the chosen position. The filtered-away data are not usable in fact, their phase is not compensated for, because their distance from the selected position is greater than a coherence length.
- S10: in this step the filtered (complex) signals of the DUT undergo a re-sapling process at the part of the laser frequency which varies more slowly as measured with the laser monitor.
- If the linearized DUT response is used in the frequency domain the steps are concluded, else (S11) the signals are Fourier transformed to obtain the corresponding DUT interferometric response signals in the time domain.

The in-phase and quadrature signals from the laser monitor interferometer contain information about the laser phase. The two signals are intensities and their conversion is needed to obtain the laser phase representation. The formulation of the laser light is as a complex field in which phase φ and amplitude ρ are functions of time:

$$E(t) = \rho(t)e^{i\varphi(t)} \tag{5.1}$$

The fields reaching the 3x3 coupler (providing 120 degrees of phase shift between the interference fringes hitting on the two detectors – I and Q) are delayed and reduced in amplitude due to the paths of the interferometer:

$$E_{T_1}(t) = \alpha_{T_1}\rho(t - T_1)e^{i\varphi(t-T_1)} \tag{5.2}$$

$$E_{T_2}(t) = \alpha_{T_2}\rho(t - T_2)e^{i\varphi(t-T_2)} \tag{5.3}$$

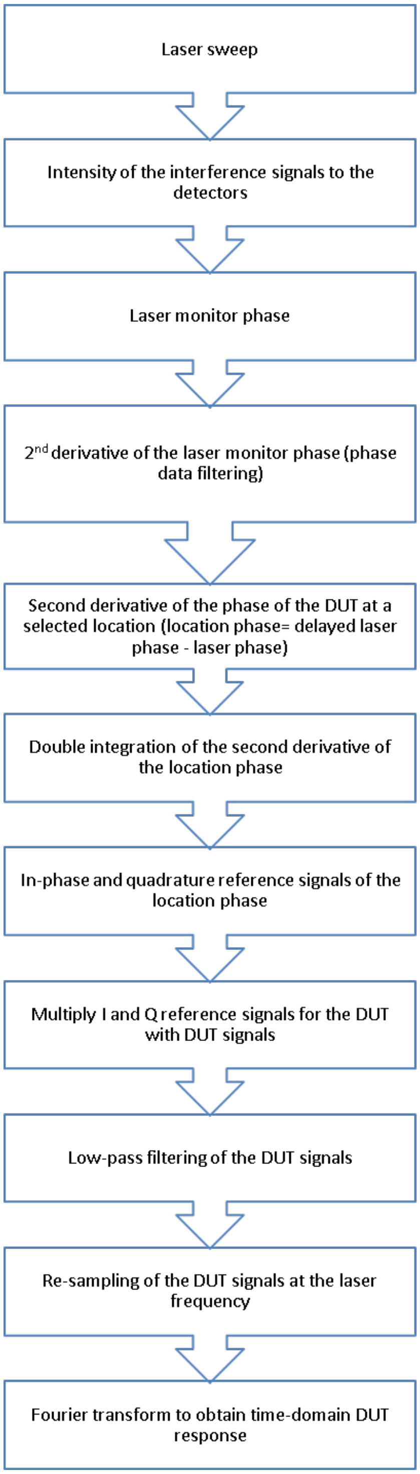

Figure 5.8: Flow-chart of the OFDR working procedure.

Where α_{T_1} and α_{T_2} are the losses due to the path of each arm of the interferometer, T_1 and T_2 are the delay in the time-of-flight of the light related to the paths of the interferometric system.
The outputs of the coupler are the input of the detectors and are new field obtained by the recombination of the input ones:

$$E_{det_1}(t) = E_{T_1}(t) + E_{T_2}(t) \tag{5.4}$$

$$E_{det_2}(t) = E_{T_1}(t) + E_{T_2}(t)e^{i\varphi_c} \tag{5.5}$$

Where $\varphi_c \cong 120$ degrees is the phase shift caused by the coupler.
The intensity detected by each detector are:

$$\begin{aligned} I_1(t) = |E_{det_1}(t)|^2 = \Big(E_{T_1}(t) + E_{T_2}(t)\Big)\Big(E_{T_1}(t) + E_{T_2}(t)\Big)^* &= \\ = \quad \Big(\alpha_{T_1}\rho(t-T_1)\Big)^2 + \Big(\alpha_{T_2}\rho(t-T_2)\Big)^2 &+ \\ + 2\alpha_{T_1}\rho(t-T_1)\alpha_{T_2}\rho(t-T_2)\cos\Big(\varphi(t-T_1) - \varphi(t-T_2)\Big) \end{aligned} \tag{5.6}$$

$$\begin{aligned} I_2(t) = |E_{det_2}(t)|^2 = \Big(E_{T_1}(t) + E_{T_2}(t)\Big)\Big(E_{T_1}(t) + E_{T_2}(t)e^{i\varphi_c}\Big)^* &= \\ = \quad \Big(\alpha_{T_1}\rho(t-T_1)\Big)^2 + \Big(\alpha_{T_2}\rho(t-T_2)\Big)^2 &+ \\ + 2\alpha_{T_1}\rho(t-T_1)\alpha_{T_2}\rho(t-T_2)\cos\big(\varphi(t-T_1) - \varphi(t-T_2) - \varphi_c\big) \end{aligned} \tag{5.7}$$

Considering an ideal case $\alpha = constant$, $\rho = constant$ and $\varphi_c = ideal$:

$$\begin{aligned} I_1(t) &= (\alpha\rho)^2 + (\alpha\rho)^2 + 2(\alpha\rho)^2\cos\Big(\varphi(t-T_1) - \varphi(t-T_2)\Big) \\ &= 2(\alpha\rho)^2\left(1 + \cos\Big(\varphi(t-T_1) - \varphi(t-T_2)\Big)\right) \end{aligned} \tag{5.8}$$

$$\begin{aligned} I_2(t) &= (\alpha\rho)^2 + (\alpha\rho)^2 + 2(\alpha\rho)^2\cos\Big(\varphi(t-T_1) - \varphi(t-T_2) - \varphi_c\Big) \\ &= 2(\alpha\rho)^2\left(1 + \cos\Big(\varphi(t-T_1) - \varphi(t-T_2) - \varphi_c\Big)\right) \end{aligned} \tag{5.9}$$

Plotting a graph of the intensity signal at a detector against the intensity signal at the other detector, the resulting figure is an ellipse, to derive the phase $\theta(t) = \phi(t$ - $T_1)$ - $\phi(t$ - $T_2)$, it is necessary to obtain a circle with the centre in the origin, in this way the angle within the complex vectors of the intensities signals corresponds to the phase $\theta(t)$.
To obtain this transformation, the shift phase between the signals to the detectors, ϕ_c, is assumed as 120 degrees (the 3x3 coupler is considered as ideal); each signal gets subtracted an offset in order to centre the circle in the origin and then the magnitude of the phase vector gets normalized. At this point sin θ(t) is plotted against cos $\theta(t)$ in which the cosine corresponds to $I_1(t)$ and the sine is $\sin\theta(t) = \frac{I_1 \cos\varphi_c - I_2}{\sin\varphi_c}$.
The phase angle $\theta(t)$ indicates the frequency of the laser at each instant and is calculated as the arc-tangent on all the four quadrants, in fact the derivative of the phase with respect to time is the frequency.
θ(t) is the variation of phase of the laser light at different moments, with the transfer function of the interferometric system it is possible to calculate the real laser phase $\varphi(t)$.
The Fourier Transform of the phase $\theta(t) = \varphi(t - T_1) - \varphi(t - T_2)$ is:

$$\Theta(t) = \Phi(\omega)e^{i\omega T_1} - \Phi(\omega)e^{i\omega T_2} = H(\omega)\Phi(\omega) \tag{5.10}$$

Where $H(\omega) = e^{i\omega T_1} - e^{i\omega T_2}$ is the linear-system response of the interferometer. Each zero of the transfer function corresponds to a multiple of the delay difference $\frac{1}{T}$ and at the frequencies in which the transfer function vanishes, the signal has not any information regarding the laser phase, since the coherence time of the laser must be greater than the delay difference measured with the interferometer.
Using the transfer function for the derivative of the laser phase, the singularity at zero of the transfer function is avoided and then the laser phase is obtained thanks to the integration of the derivative of the laser phase.

$$H_d^{-1}(\omega) = \frac{-i\omega}{e^{i\omega T_1} - e^{i\omega T_2}} \tag{5.11}$$

Another advantage deriving from the calculation of the derivative of the laser phase is that it is directly taken in the further processing operations and requires less bits than the laser phase itself.
If the laser phase in the frequency domain $\Phi(\omega)$ is limited until $\frac{1}{T}$, the effects of the singularities of the transfer function can be eliminated multiplying the transfer function by a window-profile function $G(\omega)$ that makes the amplitude of the laser phase tend to zero outside the window width, going from $f = 0$ to $f = \frac{1}{T}$.

There are two ways to calculate the laser phase:

- 1: In the frequency domain: multiply the Fourier transformed interferometer phase $\Big(\theta(t)$ into $\Phi(\omega)\Big)$, by the inverse transfer function limited by the window $G(\omega)H(\omega)$ and then calculating the result in the time domain with a Fourier back-transform.
- 2: In the time domain: executing the convolution between the interferometer phase $\theta(t)$ and the impulse response of the transfer function $g(t)$.

The calculation in the time domain can directly be executed using an FPGA, the ideal transfer function is the result of the filtering process of the data with a FIR filter (finite-impulse response). The design of the FIR filter presents a gain derived from the ratio of the interferometer delay of the laser monitor and the clock delay. The result of this process is the derivative of the laser monitor phase.
If the process uses the derivative of the laser monitor phase, the result is the second derivative of the laser monitor phase, which needs to undergo double integration to obtain the phase.
The phase (or its derivative/s) obtained with the process described above is used to calculate the interferometric response with any delay. The response of the DUT interferometric system has a precise delay for each reflection distance.
This can be seen in a similar interferometer in which the longer path includes the DUT, which can be simplified in the model as a huge quantity of reflectors whose locations are related to a certain delay.
Naming τ_1 the delay in the reference arm of the interferometer and τ_2 the delay in the signal arm, the detector receives an intensity:

$$\begin{aligned} I_S(t) &= DCTerms+ \\ &+ \quad \alpha_1\rho(t-\tau_1)\int_{\tau_2=0}^{L} \alpha_2\rho(\tau_2)e^{i\gamma\tau_2}\rho(t-\tau_2)e^{i\Big(\varphi(t-\tau_1)-\varphi(t-\tau_2)\Big)}\,d\tau_2 \end{aligned} \tag{5.12}$$

Where α_2 is the loss in the DUT arm; γ is the phase of the reflection in the DUT depending on the delay; τ_2 in the delay in the time-of-flight due to the selected position.

The phase of the selected delay (position) is the difference between two delayed laser phases:

$$\theta_S(t) = \varphi(t-T_1) - \varphi(t-T_2) \tag{5.13}$$

And Fourier transformed is easier to calculate:

$$\Theta_S(t) = \Phi(\omega)(e^{i\omega T_1} - e^{i\omega T_2} = H_S(\omega)\Phi(\omega) \tag{5.14}$$

The time-domain transfer function of the phase at the selected position (delay) is:

$$h_\tau(t) = \delta(t - \tau_1) - \delta(t - \tau_2) \tag{5.15}$$

The digital processing needs sampled signals, for this reason the input signals are sampled at the frequency f_s:

$$\tilde{h}_\tau(q) = h_\tau(\frac{q}{f_S} = \delta(\frac{q}{f_S} - \tau_1) - \delta(\frac{q}{f_S} - \tau_2) = \delta(q - \tau_1 f_S) - \delta(q - \tau_2 f_S) \tag{5.16}$$

A shift register can be used to implement the calculation but also the delays τ_1 and τ_2 have to be converted in integer multiples of the sample period. The shift register executes the integration of the second derivative of the phase to extract its first derivative. The sampling affects the resolution of the position of the central section of the DUT, reducing it. But, set the chosen length of the DUT, the coherence length of the laser considers a segment including the selected position.

It is important that the coherence length of the laser is larger enough than the smallest variation in time in the shift register.

At this point, the information data about the reflection in distance in the DUT is obtained with the signal of change in the predicted phase. This procedure requires the use of the phase related to the delay to extract the in-phase and quadrature signals (sine and cosine signals). The following step consists in the mixture of these signals with the intensity of the signal of the DUT interferometer in order to obtain and elaborate the data polarized p and s, composed of real and imaginary parts. The signal received at the detectors is real by definition and gets multiplied by the real and imaginary parts of the signal to measure. Then, there is a low-pass filtration to produce a signal representing the wanted signal of the interference process. The width of the filter determines the length of the portion represented by the extracted data.

The operation of integration can be executed with the shift register explained above, but also with a digital accumulator which represents 2π as a binary integer number. The accumulator at every cycle starts again from zero, reducing the resources to save the values. For every signal, look-up tables depending on the value of the phase are created to convert the in-phase and quadrature signals in binary and then the signals undergo the multiplication with the DUT signals detected by the s and p detectors. Again, a low-pass filtering is performed but, in this case, the cut-off frequency is lower than linewidth of the laser in order to reduce the spectral contents. The resulting signal is the reflection in the DUT around a position established by the selected delay for the extraction of the phase related to the delay and the length of the considered tract in the DUT is determined by the width of the low-pass filter.

The data from the s and p detectors are mixed, filtered and then linearized with the optical frequency with the aim to Fourier transform data with high resolution. The linearization is achieved with the filtration of the phase derivative, then integrated with the shift register.
The resolution is the inverse of the laser linewidth, thus is very high in this system because the laser sweeps a broad range of wavelengths. The laser is tuned both with current driving and temperature controlled.
The entire system is represented in Fig. 5.9 [26].

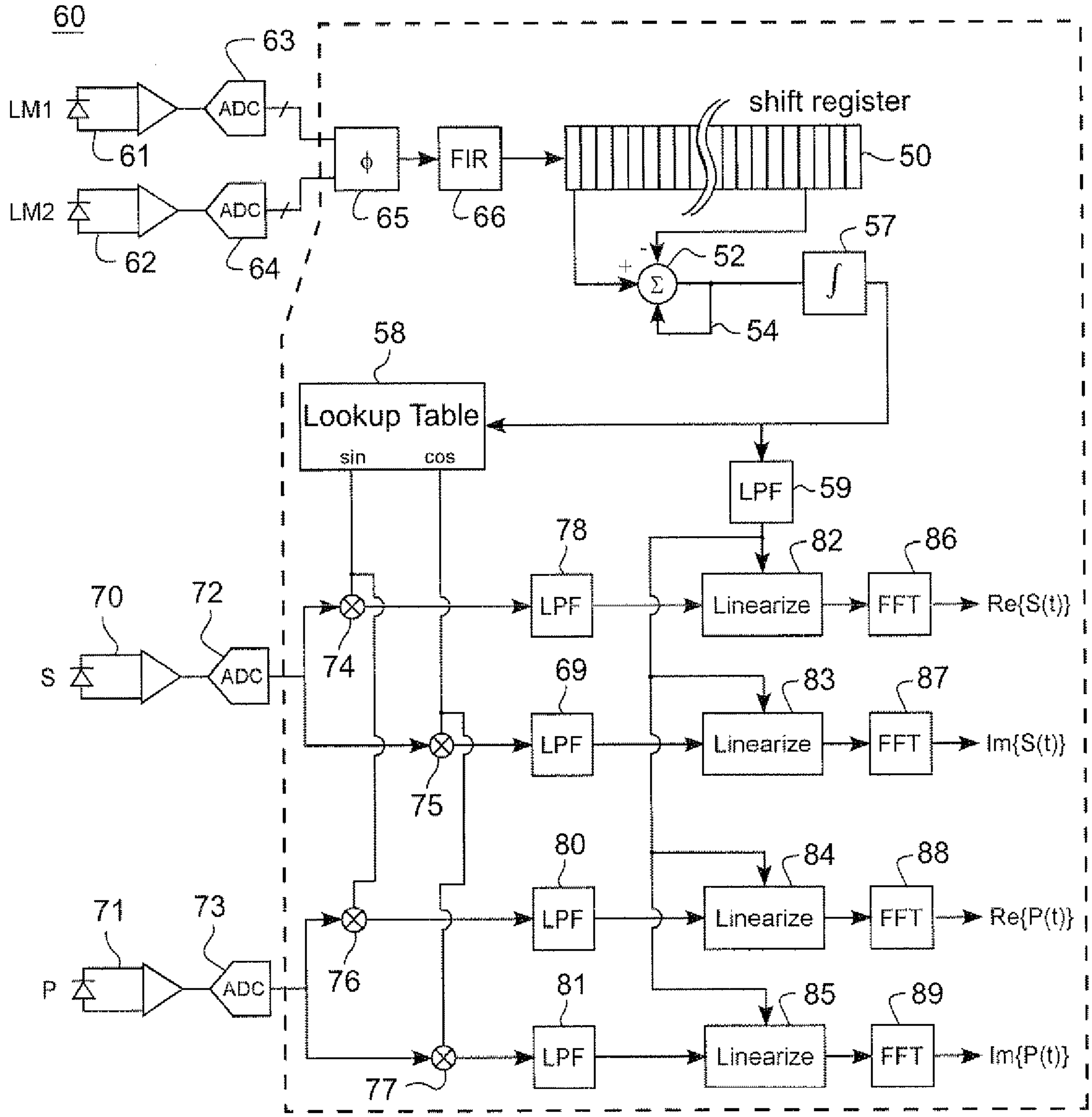

Figure 5.9: Scheme of the entire system of the patent *US 7.515.276 B2* [26].

Chapter 6

Sensors for temperature monitoring during laser ablation

The main scope of thermal treatments is the precise removal of the selected tumour, saving the surrounding healthy tissues.
The applicator probe and the geometrical parameters of the tumour are fundamental to achieve the success of the treatment. But, another important actor in the process is the temperature monitoring in order to control the evolution of the thermal ablation because there are specific temperature levels leading to cytotoxic effect [27].
The temperature level reached inside the tissue helps the operator to adjust the treatment settings during the current ablation process and to visualize the damaged area and the surrounding parenchyma, following the clinical practice of treating also a 1 cm-thick border to prevent the recurrence of the neoplasia.
The risk for the sensor deriving from these measurements close to the emitting tip is to be irreversibly damaged, bringing to errors in the monitoring of the temperature.
The temperature monitoring techniques are classified in two main categories: non-invasive and invasive approaches.

6.1 Non invasive methods for temperature monitoring

This kind of sensing procedure is more and more interesting, obviously because of their non-invasiveness, but also for their capability to map (2D) of temperature of the area surrounding the irradiating tip.

6.1.1 CT-based thermometry

At the beginning (1970s) of its application in the thermometric field, the radiodensity (HU - Hounsfield Unit) of the water was measured experimentally as the temperature changes were applied. But it was abandoned, due to problems of reproducibility and spatial resolution

apart from the X-ray irradiation on the patient, the biggest obstacle.
The X-rays go through the patient and are detected only the transmitted rays, according to the linear attenuation coefficient μ.
Each pixel corresponds to the attenuation of the relative voxel of tissue.
In the CT-scan the obtained image is reconstructed from the different images obtained at many shooting angles (Fig. 6.1 [28]).
The CT number is expressed in HU with the following formula [29]:

$$CT\left(x,y\right)=1000\,\frac{\mu\left(x,y\right)-\mu_w}{\mu_w} \tag{6.1}$$

Where

μ_W is the linear attenuation coefficient of the water;

μ (x , y) is the attenuation coefficient of the considered voxel and depends on the effect of the X-ray on the tissue element.

The X-ray hitting the tissue causes the removal of an electron (photon) from the target (Compton scattering), the energy (related to the wavelength) and the angle of the scattered photon are influenced by the temperature.
In fact, the density is a function of the temperature and this relates on the linear attenuation coefficient. The result is the following equation [29]:

$$\Delta CT\approx-\left[1000+CT\left(T_0\right)\right]\alpha\Delta T \tag{6.2}$$

Where the left-hand term is the variation in CT as the temperature changes (from T_0 to T).
Many studies have been performed about CT thermometry, but the results obtained with the *in vivo* tests showed issues related to the artefacts and to thickness of the area to be investigated adding to the dose released to the tissue.

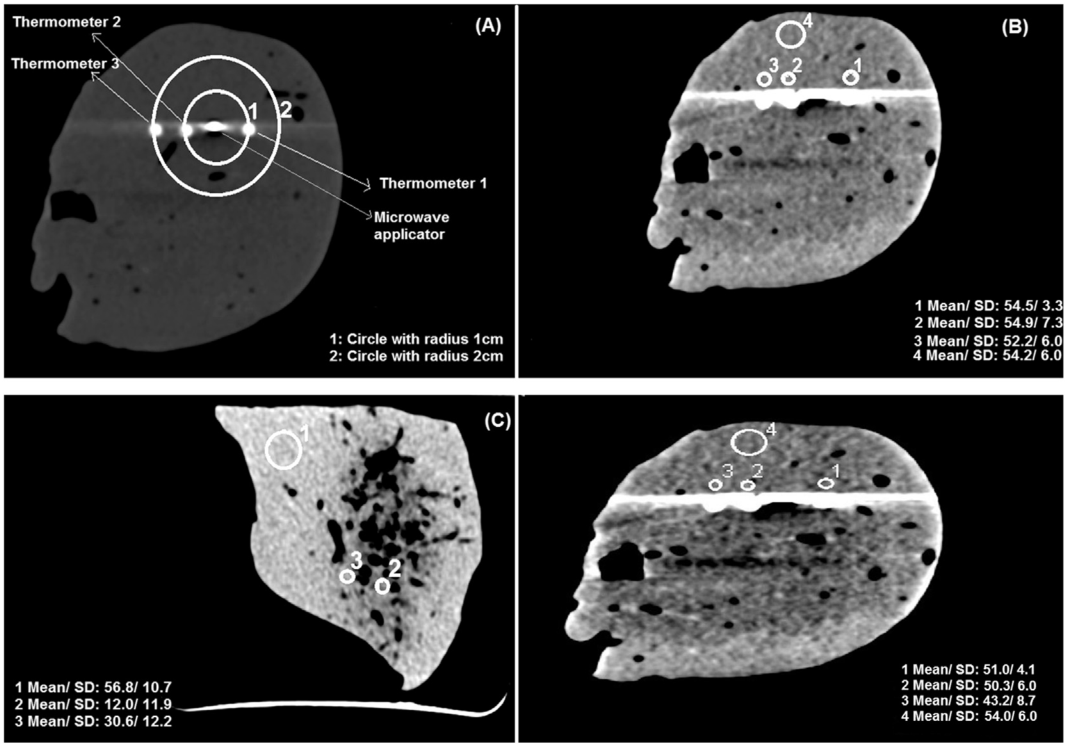

Figure 6.1: CT-themometry. (A) Image cross-section shows the porcine liver parenchyma with tips of the inserted ablative (MWA) applicator and the temperature sensors. The two white circles shows 1 cm and 2 cm radius measured for thermometer positions from the applicator. (B) Pre-ablation computed tomography image with basic organ temperature, the values in HU at different location are reported. (C) Cross-sectional image of the porcine liver at the end of MWA procedure; the region with low HU values are close to the applicator. (D) Cross-sectional image obtained at the end of cooling phase. The values in HU at the location of the temperature sensors are higher [28].

6.1.2 Ultrasound-based thermometry

The physical principle of the US imaging is the interaction of a sound wave emitted with a probe at high frequency 2-15(MHz) with the tissue. The probe is both emitter and receiver. The reflected sound wave (echo) reaches the emitter with a certain delay in time from the emission instant the delay brings the information related to the consistence and the shape of the tissue.

The intensity of each echo is then plotted against the position, in order to obtain an image representing a section of the analysed tissue.

The time delay of an echo located at z is [29]:

$$t\left(T_0\right)=\frac{2z}{v_s\left(T_0\right)} \tag{6.3}$$

Where

v_s (T_0) is the velocity of the sound wave in the tissue when the temperature is T_0.

The time shift Δt is caused by the thermal expansion and the variation of the velocity of the sound, since the latter is preponderant over the former, the relationship between the time shift and the temperature change is [29]:

$$\Delta T \approx k_1 \frac{d\left(\Delta t\right)}{dt} \tag{6.4}$$

Where

k_1 is a tissue-dependent constant;

$\frac{d\Delta t}{dt}$ is the normalised time shift.

The time shift of each frame is normalised and transformed into a temperature map and the variation in the attenuation coefficient gives information about the denaturation state of the tissue.

The advantages of US-based thermometry are the non-invasiveness, the use of sound waves, compatible with metallic elements, and the widespread existence of US technology.

The issues of this technique are: the strong artefacts deriving from the breath and the pulse movements and the compromise to reach between the spatial resolution of the image and the depth in penetration.

6.1.3 MRI-based thermometry

The studies in MRI-based thermotherapy increased with the development of the LA, due to the electromagnetic compatibility of the optical fibres [27, 30, 31, 32].

Temperature measurement with T1 relaxation time

When a radiofrequency signal is applied to a medium in a magnetic field B_0, a rotating magnetic field B_1 is superposes and is perpendicular to the principal magnetic field B_0. The magnetization vector M varies its orientation and begins to rotate.

Then, the radiofrequency signal is removed and the rotating magnetic field B_1 ends.

The vector M returns to its initial configuration (aligned with B_0) during the ″relaxation process″.

The time constant T_1 rules the process for the longitudinal component M_Z.

The time constant T_2 rules the process for the transversal component M_{XY}.

T_1 is always bigger than T_2 because it depends on the intensity of the principal magnetic field B_0.

The temperature can be measured monitoring the variation in T1 relaxation time. T1 is the result of the dipolar interactions of water molecules and macro-molecules, consequence

of their motion (roto-translation). The temperature affects the roto-translation and varies T1, heating increases T1.
In the water molecule, the dependence of T1 on the temperature is almost linear [29]:

$$T_1 \propto exp\left(-\frac{E_a\left(T_1\right)}{k_B T}\right) \tag{6.5}$$

Where
$E_a(T1)$ is the activation energy of the relaxation process;
k_B is the Boltzmann constant ($1.38 \cdot 10^{-23}$ J/K);
T is the absolute temperature (K).

The lipids cause artefacts and thus, it is important to operate in fat-suppression mode. Apart from this solvable difficulty, this technique is suitable for qualitative measurements because: the issue is the change of tissue property due to thermal action, leading to non-linear effects and to wrong value of T1 due to the fact that the properties of the tissue should be evaluated continuously because of the dependence of T1 on them.

Temperature measured with proton resonance frequency

The temperature can be measured also with proton resonance frequency (PRF) [29, 32].
The PRF shifts according with the temperature, the chemical shift is the variation in the resonant frequency of a nucleus compared to a reference element. The external magnetic field B_0 and the structure of a molecule (location of atoms) influence the resonance frequency of a nucleus.
In a single water molecule, a hydrogen nucleus is better protected by the cloud of electrons than when the water molecule binds with other molecules with hydrogen bonds.
The temperature affects the configuration of the molecules and thus, the protective electron clouds around the hydrogen atoms.
The heating increases the protection layer in the interval of temperature typical of the thermal treatments.
Temperature processes shift the resonance frequency, measured as the translation of the peaks in water spectrum. But the resolution in space and time is low.
The phase shift is a second method relating the change in temperature to the phase shift of the image from the initial phase, at known temperature.
The experimental *in vivo* tests show that the non-homogeneity of organic tissue is a problem because the temperature variation does not maintain its linearity and that the breath motion artefact has not yet solutions.

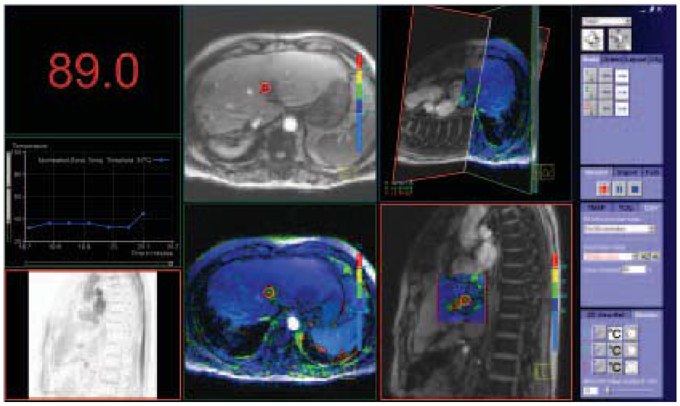

Figure 6.2: MRI thermometry with the PRF method during liver laser ablation [30].

6.2 Invasive methods for temperature monitoring

This kind of method provides for the sensitive element to be in direct contact with the area of ablation.
It is the most common procedure to monitor the temperature during the thermal treatment.

6.2.1 Thermocouples

Wide measurement range, good accuracy, fast response, small dimensions and low cost are the qualities of the thermocouples making them to be widely diffused.
On the contrary, the measurement are punctual and, moreover, the metal of which they are made is a disadvantage because absorbs the laser IR-radiation, this involves the heating of the metallic structure of the thermocouple which means that the sensor overestimates the temperature of the tissue (error).
The thermocouples can be either protected, which means more strength, but long response time and more invasiveness; or unprotected, which means small dimensions and rapid response, but more fragility.
The Seebeck effect is the basis of this kind of sensor. It consists of the generation of current due to thermal transmission within a conductive wire. The temperature varies the distribution of the electrical charges inside the conductor, generating a voltage. The Seebeck coefficient depends only on the material of the wire.
The thermocouple is composed of two wires of different metals joined together and the voltage at the extremities of the entire wire is the sum of the voltages on each conductor, according to the Kirchhoff's circuit law.
The sensitivity of the thermocouple is 40 µV/°C.
The error in the temperature measurement (overestimation) is not negligible (10-20 °C, depending on the distance from the laser source), thus it is necessary to fix it, considering that the heating due to the laser absorption is very rapid. In fact, the increase in temperature

can be split in fast (increase cause by absorption) and slow response time. The correction consists in subtracting the value of the fast response [29].
Another method of correction is the switching on and off the laser repeatedly and measuring the artefact as the average of the values acquired during many tests [29].

6.2.2 Fibre-optic sensors (FOS)

This kind of sensor is not so common as thermocouples because of its high-cost and the relative recent diffusion in the medical world. But in the last years they have been more affordable and thus, more employed [27, 33, 20, 34, 35, 36, 37, 38, 39].

Fibre Bragg Gratings

The FBGs are in-fibre components, realized creating periodical variation of the refractive index of the fibre optical core. The FBGs are introduced in Chapter 4. The results of the *in vivo* tests with the FBG-sensors are satisfying in agreement with the results from a reference sensor, both during cryoablation and hyperthermal ablation. The sensors have been protected from strain, inserting the optical fibre with FBGs in a probe.
The error due to strain is negligible also in the case in which the sensor is not protected and the system is stationary (*ex vivo* tests).
In fact, during the *in vivo* tests without the external protection, the breath movements can introduce non-negligible errors (2.3 °C).
The issue of the use of the Fibre Bragg Gratings is the expensiveness of the optical interrogators and the fact that the strain is detected and cannot be distinguished from the temperature variation, leading to sensitivity to breath motions.
But the great advantages of FBG are the electromagnetic compatibility, typical of the optical fibres, allowing the employment in MRI-based thermometry studies and the use under MR imaging; the rapid response, the good temperature resolutions (0.1 °C) [29] and the small size, in fact the arrays are sequences of FBGs which means high density of sensing points (1 mm of resolution in space).

Chirped FBGs

This kind of FBG is a variation of the common FBG, because the grating has not a constant periodicity but it varies with a linear profile.
It works as a array of FBG sensors, and thus the spatial resolution is very high but suffers from the limit in spatial detection of the optical interrogator [38].

Fluoroptic sensors

The basic principle of this sensors is the fluorescence time decay of a phosphor sensitive to temperature at the end of an optical fibre.

The temperature affects the time of decaying of the phosphor. The fibre is the way of propagation of the light pulse exciting the phosphor and of the signal from the phosphor, with exponential profile related to the temperature.

The temperature is obtained from a relationship between time decay and temperature. The advantages of fluoroptic sensors are the extension of the temperatures sensed, the electromagnetic compatibility, with the same considerations as for the FBGs, and good accuracy (0.2 °C) [29].

The main disadvantage of the fluoroptic sensors is the artefact, related to the dark coating of the sensing element which is heated by itself. This error in the temperature measurements is negligible only if the laser irradiating tip and the fluoroptic sensor are distant less than 4 mm.

Rayleigh scattering in a SMF

The sensing performed with this technique allows a complete totally distributed sensing of the temperature.

The basic principle is the measurement of the Rayleigh backscatter of a single-mode fibre undergoing change in temperature [27, 20, 35, 38, 40].

The instrument used to detect the Rayleigh backscatter along the length of the optical fibre exploits the swept-wavelength interferometry. This allows sub-millimetric spatial resolution.

The architecture of the instrument consists of a tuneable laser source and an interferometer, in which an arm is the optical fibre to investigate. The laser gets split between the two branches of the interferometer and after having travelled in the branches gets recombined.

The two arms are different in length, so the two light signals do not get at the same time at the recombination coupler and with the same phase. The recombination signal is an interference signal and is split by a polarization controller according to the polarization state (s , p) and then detected. To extract the Rayleigh scattering as a function of time (which means of length of the optical fibre), a Fourier transform is needed.

The temperature changes are, however, in the frequency domain because the variation of temperature shifts the peak of cross-correlation between the signals performed in steady conditions and after the thermal variation.

The shift is finally converted into temperature change with the sensitivity coefficient of the optical fibres: 10 pm/°C.

The error in temperature is 0.5 °C and in position is sub-millimetric.

The advantage is the negligible cost of the SMF, but not the cost of the instrument of detection and measurement.

Part II

Experimental activities

Chapter 7

Optical sensors characterization

The aim of this project is to study and validate two typologies of optical fibre sensors in order to monitor the temperature during the treatment of laser ablation.
The investigated sensors are: two quasi-distributed sensors and a fully distributed sensor.
The reliability of the sensors have been tested with respect to a reference sensor, a thermocouple, the same for all the trials described in the present chapter.
The formers are FBG-arrays inscribed in the core of two single-mode telecom-grade optical fibres with the use of a femtosecond laser (Workshop of Photonics – laser micromachining workstation for laboratory FemtoLAB), in cooperation with the interdepartmental center PhotoNext of Politecnico di Torino (Links Foundation, Turin). The arrays are respectively of 7 and 15 FBGs.
The latter is a standard single-mode optical fibre. At the beginning the measurements have been performed with the fibre covered by the polymeric jacket, but the inconsistent results compared to the reference sensor had lead to a further test with no protective polymeric jacket on the fibre.

The first step has been the characterization of the FBG arrays in a climatic chamber and it is fundamental to relate the temperature with the Bragg wavelength.
To prevent mechanical stresses from acting of the sensors, they have been placed inside a metallic cylinder with the thermocouple.
Then, in another test, the OFDR instrument and the single-mode optical fibre connected to it have been used to measure temperature levels in the climatic chamber to optimize both the instrument and the optical fibre parameters, also in this case the reference sensor has been the thermocouple. The spatial resolution of the instrument has been demonstrated with a final non-thermal test.

7.1 Characterization of FBG array sensors

The first procedure performed is the characterization of the FBG arrays in a climatic chamber.

The characterization phase is fundamental because allows the definition of the parameters describing the relationship between the acquired and the desired quantities (the characteristic line). The acquired quantity is the Bragg wavelength (acquired with the optical interrogator Micron Optics Hyperion si155, see Chapter 5), the desired quantity is the temperature.

The linear relation for each FBG is:

$$\lambda_B = \lambda_0 + kT \tag{7.1}$$

Where

λ_{B} is the current Bragg wavelength;

λ_0 is the Bragg wavelength at temperature 0 °C;

k is the temperature sensitivity in pm/°C; it is the ratio between the input and the output of the sensor. If the sensitivity is high, in isothermal condition (T = constant), the resulting current Bragg wavelength is higher;
T is the temperature.

The aim of the characterization is to determine λ_0 and k, in order to obtain the temperature (the unknown of the study) from the acquired λ_{B}.

To simplify the description the arrays have been labelled:
A: the 7-FBGs-array;
B: the 15-FBGs-array.
The FBGs are numbered starting from the end of the optical fibre.
The distance between the FBGs in the array A is 4-5 mm; between the FBGs in the array B is 2 mm; and the size of each FBG is 1 mm.

The Bragg wavelengths in each superstructure FBG are paced by 4 nm, the Bragg wavelengths in the array A are in the range 1520 nm – 1544 nm, with the lower Bragg wavelength closer to the fibre end; the range in the array B is 1510 nm – 1565 nm, with the higher Bragg wavelength closer to the fibre end.

In Fig. 7.1 and Tab. 7.1 a scheme of the array A in the optical fibre is reported:

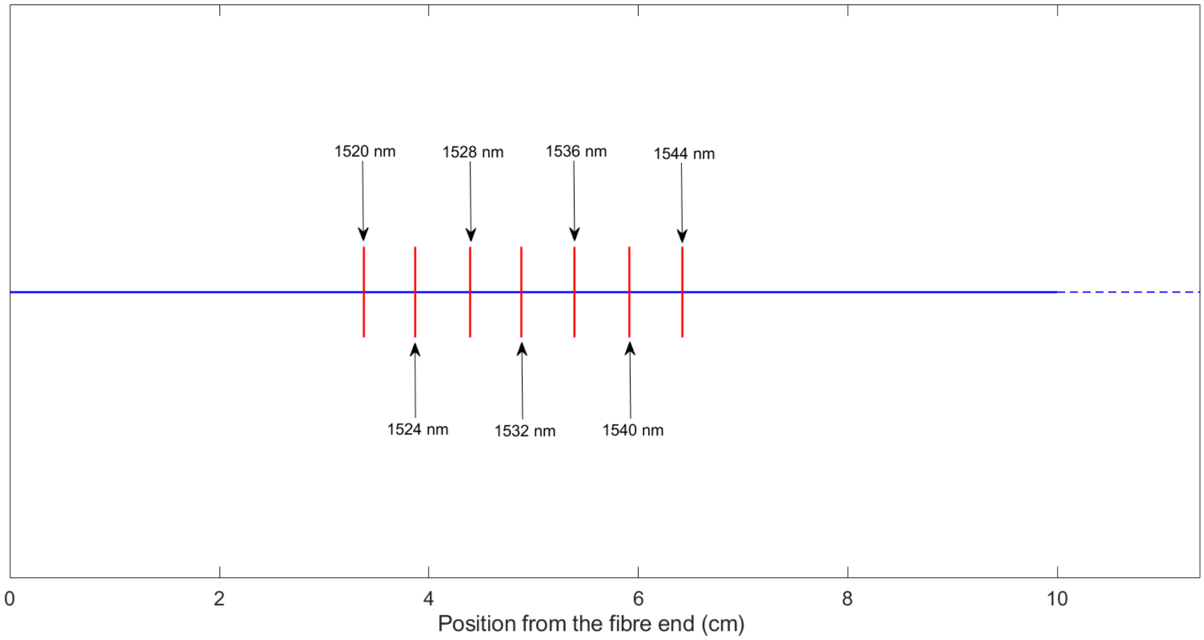

Figure 7.1: Scheme of the 7-FBGs-array (A) optical fibre.

Table 7.1: Scheme of the 7-FBGs-array (A) optical fibre.

FBG wavelength (nm)	Position from the fibre end (cm)
1520	3.38
1524	3.87
1528	4.39
1532	4.88
1536	5.39
1540	5.91
1544	6.42

Fig. 7.2 and Tab. 7.2 reported are a scheme of the array B in the optical fibre.

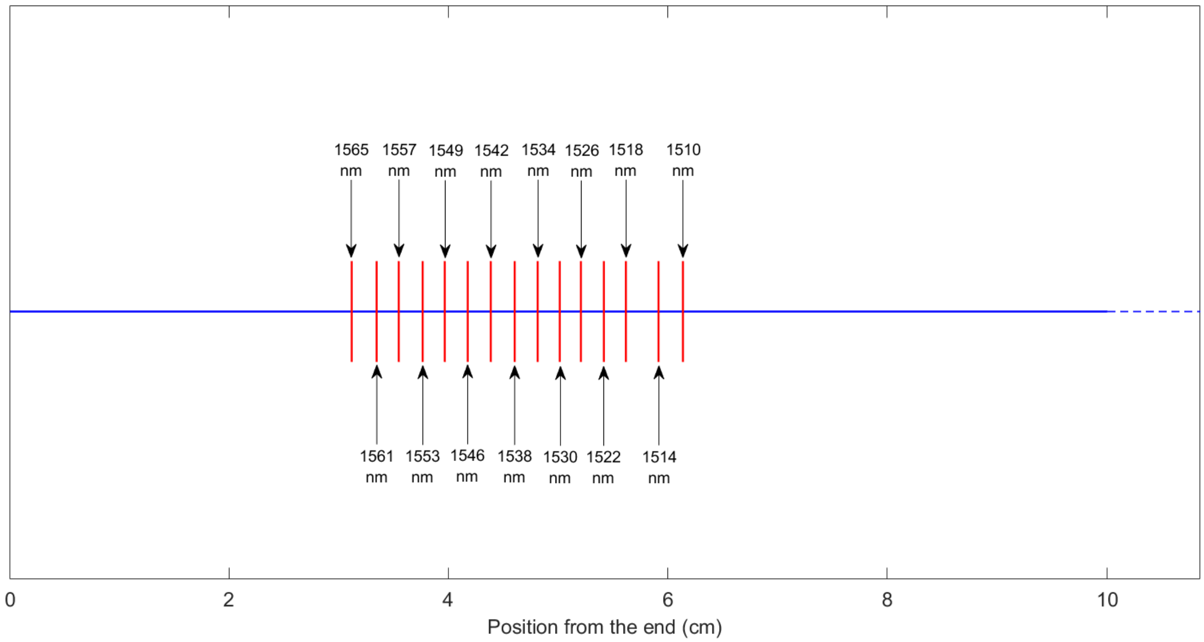

Figure 7.2: Scheme of the 15-FBGs-array (B) optical fibre.

Table 7.2: Scheme of the 15-FBGs-array (B) optical fibre.

FBG wavelength (nm)	Position from the fibre end (cm)
1565	3.11
1561	3.34
1557	3.54
1553	3.76
1549	3.96
1546	4.17
1542	4.38
1538	4.60
1534	4.81
1530	5.01
1526	5.20
1522	5.41
1518	5.61
1514	5.91
1510	6.13

7.1.1 Measurement setup and instrumentation

The setup (Fig. 7.3) is quite simple, the FBGs-array optical fibres are connected to their optical interrogator (Micron Optics) which is controlled via Ethernet connection with a PC provided with the software Enlight. The fibres are connected to channels 1 and 4 of the interrogator.

The fibres are the inserted in a metallic cylinder (diameter 4 cm) placed on the lower shelf of the climatic chamber. The climatic chamber reaches and maintain the set temperature at constant humidity, inside the chamber the air is moved by a big fan. Because of this the metallic cylinder is necessary, to prevent the air flow from moving the fibres causing unwanted strain effects.

In the other side of the cylinder, a J-type exposed-junction thermocouple is inserted, making sure it does not touch the optical fibres, causing false results.

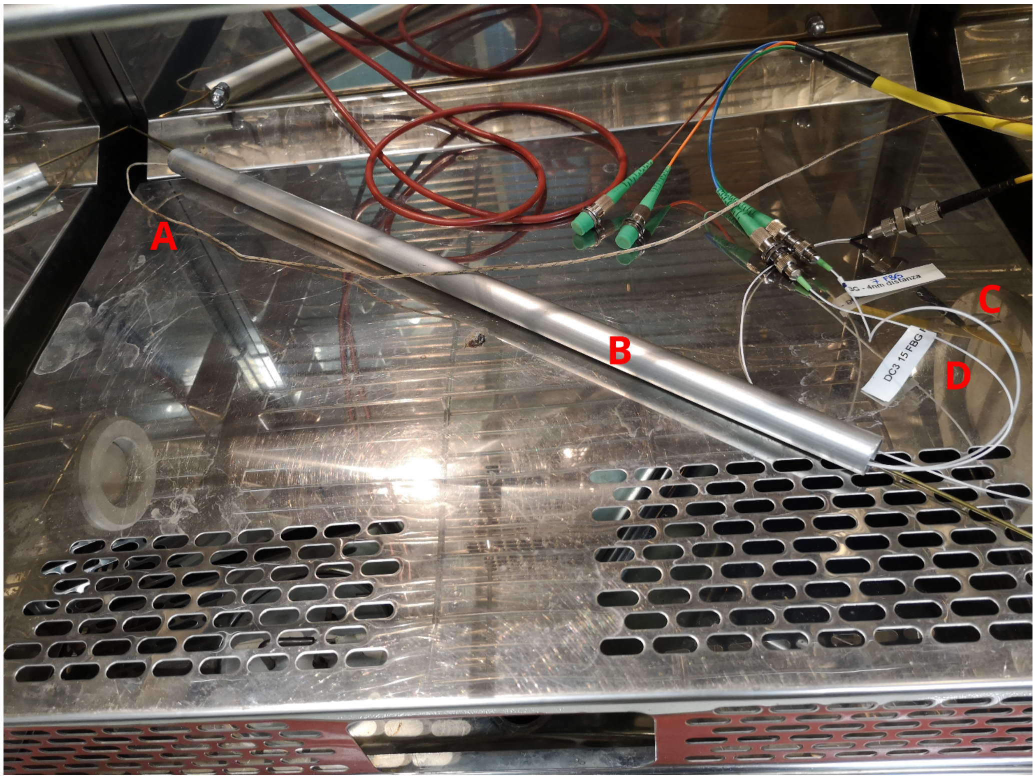

Figure 7.3: Setup inside the climatic chamber:
A. Thermocouple – B. Metallic cylinder – C. 7-FBGs-array (A) optical fibre – D. 15-FBGs-array (B) optical fibre.

Then the thermocouple connected to its relative measurement device is powered via the USB connection and the software displaying the temperature and allowing the data saving is self-launched. The user sets the type of the thermocouple (J-type in this case) and the time

interval for data saving (5 s).
The climatic chamber is turned on and the temperature levels subsequently set are: 25 °C, 35 °C, 45 °C, 55 °C, 65 °C, and the return to 25 °C. Each step consists in a transient phase and in a stable level at constant temperature, the sensors have been investigated in steady state, allowing the temperature and the sensors to stabilize. The return to the initial temperature allows to evaluate the hysteresis of every single FBG.

The instrumentation needed for the procedure is:

- Climatic chamber Vötsch VC 4018, the chamber is maintained at constant temperature and humidity as set by the user.
- Optical interrogator Micron Optics HYPERION si155, described in Chapter 5. Acquisition rate: 1 kHz; data saving interval in a text file: 5 s.
- National instrument J-type exposed-junction thermocouple with the measurement device NI USB-TC01: the USB port powers up the device and transfers data to the self-launched software for graphical view and data saving (data saving interval: 5 s). The exposed-tip junction thermocouple provides a fast response and it is convenient for rapid temperature changes.
    - Resolution: 0.0625 °C typical;
    - Temperature error: less than 1.5 °C ($T > 0$ °C);
    - Maximum sample rate: 4 S/s;
    - ADC resolution: 20 bits.
- Metallic cylinder (diameter: 4 cm) to protect the optical fibres from the effect of the air movement.

Since the temperature set in the climatic chamber and the temperature measured by the thermocouple are not perfectly matching, the temperatures indicated in the following operations are the ones set in the climatic chamber but the reference sensor temperatures (the real temperatures) have been considered for the characterization of the FBGs.
The acquired wavelength by the Micron Optics optical interrogator are saved in a text file structured in lines. Each line is an acquisition and begins with date and time in order to manage the temporal evolution of the Bragg wavelength of each FBG.
The Bragg wavelengths corresponding to every single stable thermal level have been mediated in the post-processing to reduce the noise of the signal and the least fluctuation of temperature of the chamber. The quantity of mediated values at every temperature level is not the same because of the different duration of them.

The characteristic parameters describing the behaviour of an FBG are the sensitivity k and the constant λ_0.
The constant λ_0 (nm) is the Bragg wavelength of the considered FBG at $T = 0$ °C and the

proportionality coefficient k (nm/°C) is the slope of the interpolating line.
The characteristic parameters are obtained applying the Matlab® function `polyfit` to the heating phase of the process. The inputs required are the temperature (x-axis value), the wavelength (y-axis value) and the degree of the polynomial; the output returned is the polynomial which best fits the data.

The temperature error has been obtained as the absolute value of the difference between the temperature of the reference sensor (thermocouple) and the temperature from the calibration line, during the heating phase. The hysteresis, instead, is the error in temperature obtained in case of cooling of the sensor to the initial temperature and it is higher than the temperature error, as expected.

7.1.2 Results

Fig. 7.4 represents the temperature profile measured and saved by the thermocouple.

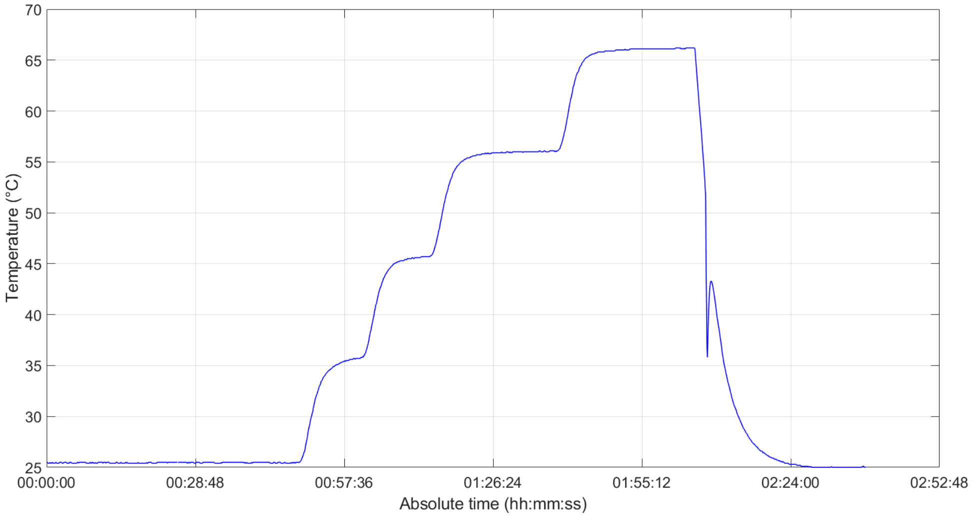

Figure 7.4: Temperature profile measured and saved by the thermocouple.

Tab. 7.3 reports the set temperature in the climatic chamber and the real temperature measured with the reference sensor (the thermocouple):

Table 7.3: Set and real temperature thermocouple.

CLIMATIC CHAMBER	THERMOCOUPLE
25 °C °C	25,459 °C
35 °C	35,67 °C
45 °C	45,56 °C
55 °C	55,96 °C
65 °C	66,07 °C
25 °C	25,01 °C

It is reported an example (Fig. 7.5) of the wavelength profile acquired during the entire characterization procedure (the most distal FBG from the fibre end in the array B - FBG 15B):

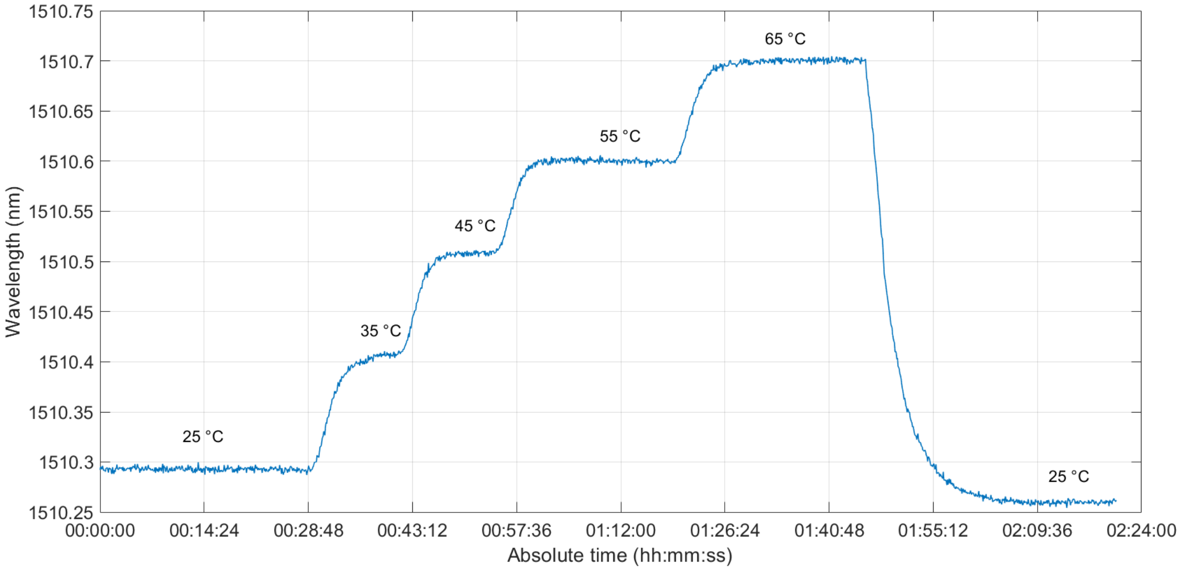

Figure 7.5: Wavelength profile acquired during the entire characterization procedure - FBG 15B.

The values of the Bragg wavelength for each FBG at each thermal step are reported in Tabs. 7.4, 7.5.

Table 7.4: Average wavelengths (nm) for each temperature level array A - channel 1.

	FBG 1	FBG 2	FBG 3	FBG 4	FBG 5	FBG 6	FBG 7
25 °C	1520,204	1524,405	1527,981	1532,21	1536,198	1539,932	1544,271
35 °C	1520,316	1524,516	1528,091	1532,323	1536,309	1540,042	1544,383
45 °C	1520,407	1524,608	1528,184	1532,414	1536,402	1540,136	1544,476
55 °C	1520,509	1524,712	1528,289	1532,519	1536,507	1540,243	1544,583
65 °C	1520,614	1524,818	1528,395	1532,625	1536,614	1540,35	1544,689
25 °C	1520,171	1524,374	1527,948	1532,176	1536,165	1539,901	1544,239

Table 7.5: Average wavelengths (nm) for each temperature level array B - channel 4.

	FBG 1	FBG 2	FBG 3	FBG 4	FBG 5	FBG 6	FBG 7	FBG 8
25 °C	1510,293	1514,138	1518,04	1521,923	1525,974	1529,997	1533,668	1537,945
35 °C	1510,408	1514,253	1518,155	1522,039	1526,091	1530,114	1533,785	1538,061
45 °C	1510,508	1514,354	1518,258	1522,142	1526,192	1530,216	1533,889	1538,163
55 °C	1510,6	1514,448	1518,349	1522,234	1526,283	1530,309	1533,981	1538,256
65 °C	1510,7	1514,548	1518,449	1522,335	1526,385	1530,409	1534,082	1538,358
25 °C	1510,26	1514,108	1518,008	1521,891	1525,94	1529,964	1533,636	1537,911

	FBG 9	FBG 10	FBG 11	FBG 12	FBG 13	FBG 14	FBG 15
25 °C	1541,674	1545,71	1549,464	1553,673	1557,424	1561,486	1565,274
35 °C	1541,789	1545,827	1549,581	1553,791	1557,542	1561,604	1565,392
45 °C	1541,893	1545,931	1549,686	1553,894	1557,646	1561,708	1565,497
55 °C	1541,986	1546,025	1549,778	1553,987	1557,739	1561,802	1565,591
65 °C	1542,087	1546,127	1549,881	1554,089	1557,841	1561,906	1565,695
25 °C	1541,639	1545,676	1549,429	1553,639	1557,39	1561,452	1565,239

The interpolating line and the real acquired wavelength for the FBG-15B of the example are compared in Fig. 7.6.

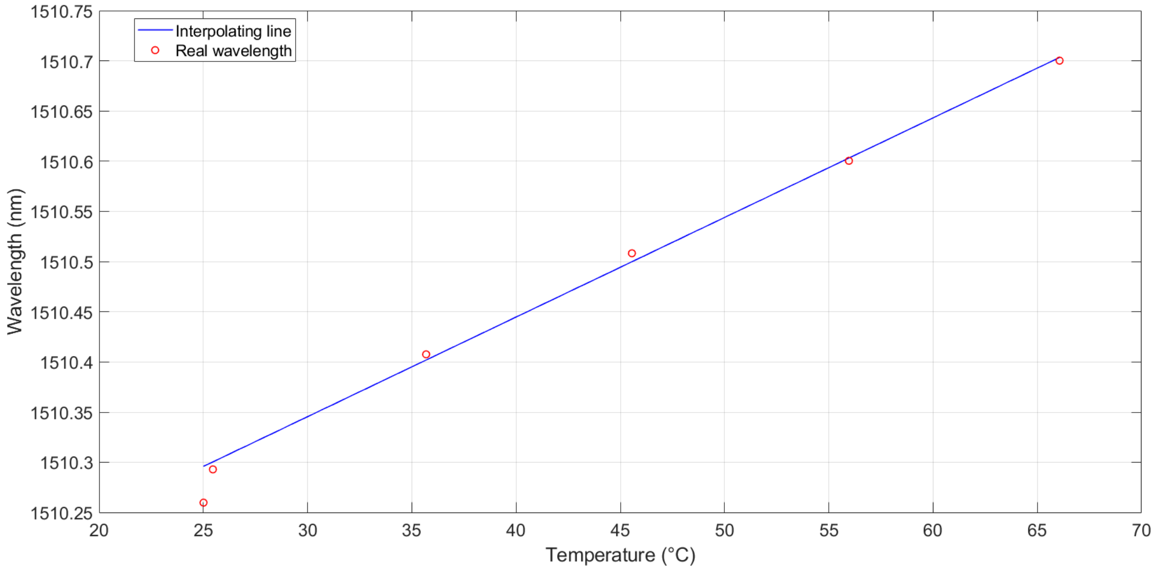

Figure 7.6: The interpolating line and the real acquired wavelength for the FBG 15B.

The calibration line, and its parameters, are the results of the characterization procedure.

Table 7.6: Parameters of calibration line - FBG 15B.

$\lambda_B = \lambda_0 + \mathrm{kT}$
$\lambda_0 = 1519.95\,\mathrm{nm}$
$\mathrm{k} = 0.01\,\mathrm{nm/°C}$
$max\ error = 0.66\,°\mathrm{C}$
$hysteresis = 3.23\,°\mathrm{C}$

The resultant λ_0, k and temperature error for each FBG are reported in Tabs. 7.7, 7.8, 7.9, 7.10.

Table 7.7: λ_0 and k – 7-FBGs-array (A) optical fibre.

	FBG 1	FBG 2	FBG 3	FBG 4	FBG 5	FBG 6	FBG 7
k (nm/°C)	0,01	0,01	0,01	0,01	0,01	0,01	0,01
λ_0 (nm)	1519,95	1524,15	1527,73	1531,96	1535,94	1539,67	1544,01

Table 7.8: Temperature error (°C) 7-FBGs-array (A) optical fibre.

	FBG 1	FBG 2	FBG 3	FBG 4	FBG 5	FBG 6	FBG 7
25 °C	0,37015	0,213986	0,151173	0,298136	0,225373	0,139637	0,194821
35 °C	0,663077	0,516718	0,420319	0,634522	0,524844	0,425427	0,492566
45 °C	0,095868	0,232114	0,228224	0,217359	0,205323	0,276383	0,248826
55 °C	0,31149	0,222466	0,192955	0,268429	0,255522	0,156916	0,192945
65 °C	0,11443	0,151848	0,152034	0,149402	0,161374	0,147509	0,144026
25 °C	3,22562	2,889406	2,984185	3,207625	3,03997	2,706391	2,891573

Table 7.9: λ_0 and k – 15-FBGs-array (B) optical fibre.

	FBG 1	FBG 2	FBG 3	FBG 4	FBG 5	FBG 6	FBG 7	FBG 8
k (nm/°C)	0,01	0,01	0,01	0,01	0,01	0,01	0,01	0,01
λ_0 (nm)	1510,05	1513,89	1517,79	1521,68	1525,73	1529,75	1533,42	1537,67

	FBG 9	FBG 10	FBG 11	FBG 12	FBG 13	FBG 14	FBG 15
k (nm/°C)	0,01	0,01	0,01	0,01	0,01	0,01	0,01
λ_0 (nm)	1541,43	1545,46	1549,21	1553,42	1557,17	1561,23	1565,02

Table 7.10: Temperature error (°C) 15-FBGs-array (B) optical fibre.

	FBG 1	FBG 2	FBG 3	FBG 4	FBG 5	FBG 6	FBG 7	FBG 8
25 °C	0,769356	0,740066	0,780421	0,790153	0,830707	0,832446	0,810437	0,746697
35 °C	0,560335	0,538294	0,505431	0,536654	0,623191	0,591627	0,541887	0,525312
45 °C	0,834574	0,788965	0,960081	0,932751	0,902317	0,904846	0,961864	0,868338
55 °C	0,286922	0,24578	0,332147	0,331435	0,366866	0,270099	0,324749	0,341226
65 °C	0,338631	0,341413	0,352944	0,347817	0,327935	0,393927	0,368566	0,305727
25 °C	3,65232	3,302686	3,584449	3,593686	3,786833	3,694003	3,543995	3,685371

	FBG 9	FBG 10	FBG 11	FBG 12	FBG 13	FBG 14	FBG 15
25 °C	0,737433	0,746429	0,796257	0,815265	0,827606	0,741166	0,756071
35 °C	0,486558	0,503336	0,520653	0,573643	0,558188	0,510056	0,530506
45 °C	0,893576	0,877484	0,982684	0,91864	0,978778	0,892383	0,888785
55 °C	0,313162	0,294793	0,360153	0,31308	0,339091	0,366394	0,360673
65 °C	0,329538	0,339598	0,346926	0,363937	0,370268	0,294878	0,302545
25 °C	3,752656	3,67491	3,802144	3,70444	3,7097	3,693184	3,725091

7.1.3 Observations

The thermal characterization is a quite long but necessary procedure in order to describe each punctual sensing element of the quasi-distributed temperature sensor.
The structure of the data text file saved by the optical interrogator is simple and easy to manage in Matlab®. Each acquisition is stored in a text line of the file, starting with date and time.
The characteristic line describing each FBG shows a direct proportionality between the Bragg wavelength and the temperature (Eq. 7.1). The experimental coefficient k reflects the value reported in FBG literature [**page 99**, 21].

7.2 Temperature sensing with the fully distributed sensor

The optical fibre sensor used for the totally distributed temperature sensing is a single-mode optical fibre (SMF-28).
The instrument used is the OBR 4600 by Luna Technologies®, an optical backscatter reflectometer based on the OFDR technology (Chapter 5).
Due to its internal structure (an interferometer), it senses only temperature changes referring the measurements to the reference arm response (the reference temperature).

The *temperature change* is obtained from the *spectral shift* as follows:

$$\Delta T = -\frac{\overline{\lambda}}{cK_T}\Delta\nu \tag{7.2}$$

Where
$\overline{\lambda}$ is the central wavelength of the scan range of the tuneable laser
(in this instrument is ∼1550 nm);
c is the velocity of the light ($\sim 3 \cdot 10^8$ m/s);
$K_T = 6.45 \cdot 10^{-6}$ °C^{-1} is the temperature calibration constant;
$\Delta\nu$ is the spectral shift;

The negative sign is due to the relationship:

$$\frac{\Delta\lambda}{\lambda} = -\frac{\Delta\nu}{\nu} \tag{7.3}$$

7.2.1 Measurement setup and instrumentation

The procedure for the execution of the test begins with the daily calibration of the OBR with the provided golden reflection tip.
Then in the OBR software the following parameters are set:

- Scan range of the tuneable laser: 1547.988 nm – 1590.731 nm.
  It is the range of wavelengths swept by the laser to interrogate the optical fibre connected.
- Gain: 12 dB;
- Group index: 1.47, the typical value for standard SMF-28 optical fibre.

The following steps are the definition of the sensing parameters:

- Sensing range: 2 m, included the end of the fibre.

  It is the length of the portion of the optical fibre on which the instrument performs sensing;
- Gauge length: 1 cm.
  It is the length of the boxcar window for the cross-correlation operation required by the instrument to perform the sensing.
- Sensor spacing: 0.5 cm.

The sensing option of the software requires a reference acquisition, because the instrument senses the temperature (or the strain) change from the reference.
Briefly, the instrument is based on the OFDR technology, thus measured spectral quantities. When the condition of the investigated optical fibre gets altered, the response of the fibre to the tuneable laser interrogation changes.
Since the OBR detects a spectral response, the change from the reference trace is a spectral shift. It is the maximum of the cross-correlation operation between the reference trace and the current trace. The length of the fibre on which is operated the cross-correlation is set in *sensing range* and the distance between them is the *sensor spacing*. The ratio between them is the quantity of points collected in the sensing procedure.

After the reference acquisition it is necessary to select the portion of the fibre on which perform the sensing. A vertical cursor is placed on the upper graph, it is the centre of a highlighted tract as long as the sensing range.
In the lower graph, automatically is calculated the selected measurement (temperature change) with respect to the reference trace.
At this point, an easy LabVIEW$^{\text{TM}}$ program implemented to control remotely the instrument in order to select the measurement and the time interval of the data saving is launched. Its effect is the disabling of the OBR software interface and the creation of a data file for each

acquisition. In the data file the data and the time of the acquisition are reported in the header and then the position in the fibre is saved with the relative sensing quantity.

The subsequent temperature levels set are: 25 °C, 35 °C, 45 °C, 50 °C, 55 °C, 65 °C, 75 °C and the cooling to 25 °C and 15 °C (for the OBR the thermal changes are relative to the reference temperature, 25 °C).

As like in the characterization of the FBGs, also in this case only the constant temperature levels have been considered.
The acquisitions for each temperature level are 34. They are mediated in the post-processing in order to obtain a single mean temperature change for each temperature level.

The instrumentation needed Fig. 7.7 for the procedure is:

- Climatic chamber Vötsch VC 4018.
- National instrument J-type exposed-junction thermocouple with the measurement device NI USB-TC01 (it is connected to a PC).
- Optical backscatter reflectometer OBR 4600 by Luna Technologies®.
- Software OBR V.3 with the *Distributed sensing option*, the software is installed on a specific PC.
- LabVIEW™ remote control program installed on the PC connected to the OBR.
- Standard single-mode optical fibre SMF-28 with the polymeric jacket.

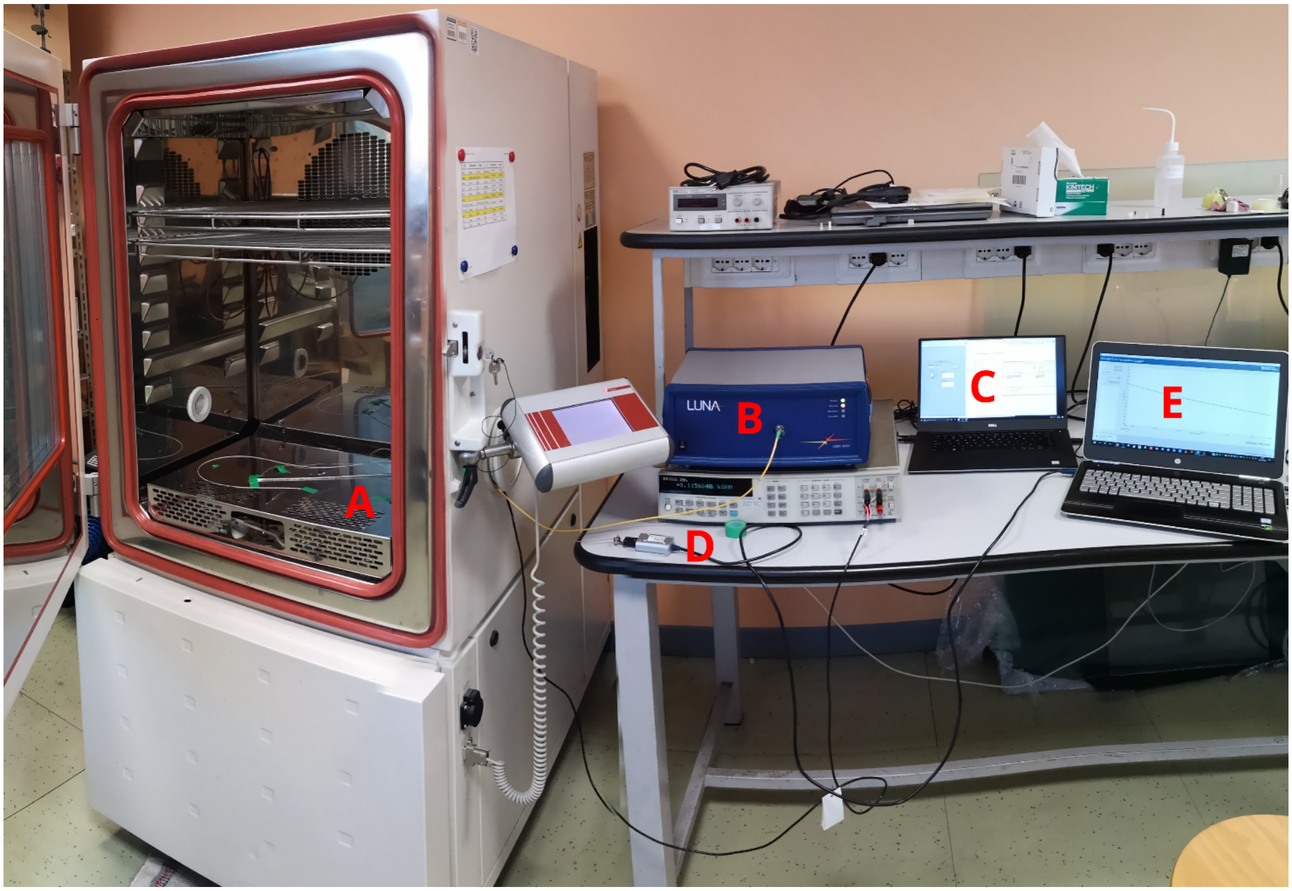

Figure 7.7: The instrumentation needed for the procedure.
A. Climatic chamber containing the SMF-28 optical fibre and the thermocouple; B. Optical backscatter reflectometer; C. PC with OBR V.3 software and LabVIEW$^{\mathrm{TM}}$ remote control program; D. Measurement thermocouple device; E. PC powering and saving thermocouple data.

7.2.2 Results

Fig. 7.8 represents the temperature profile measured by the thermocouple.

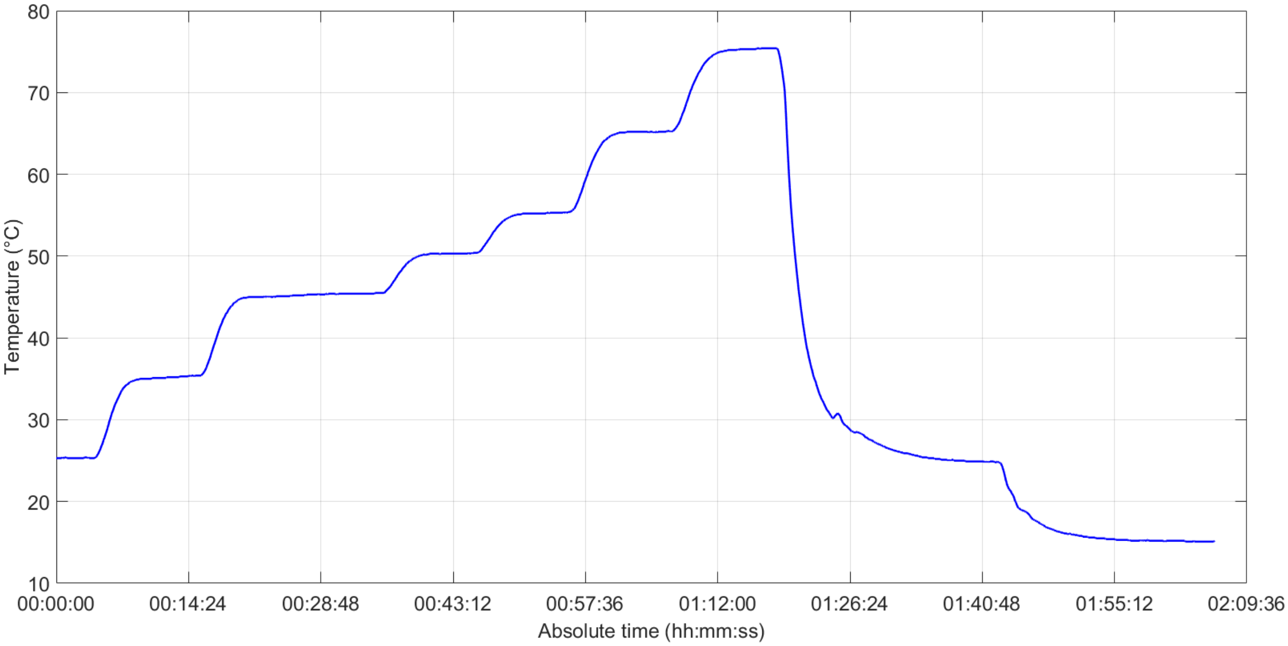

Figure 7.8: Temperature profile measured by the thermocouple.

In Tab. 7.11 is reported the comparison between the set temperatures in the climatic chamber and measured by the reference sensor.

Table 7.11: Set and real temperature.

CLIMATIC CHAMBER	THERMOCOUPLE
25 °C	25.3 °C
35 °C	35.3 °C
45 °C	45.4 °C
50 °C	50.3 °C
55 °C	55.3 °C
65 °C	65.2 °C
75 °C	75.35 °C
25 °C	24.95 °C
15 °C	15.25 °C

As like in the characterization of the FBGs, also in this case only the constant temperature levels have been considered.

Fig. 7.9 shows the temperature change along the entire sensing range extension.

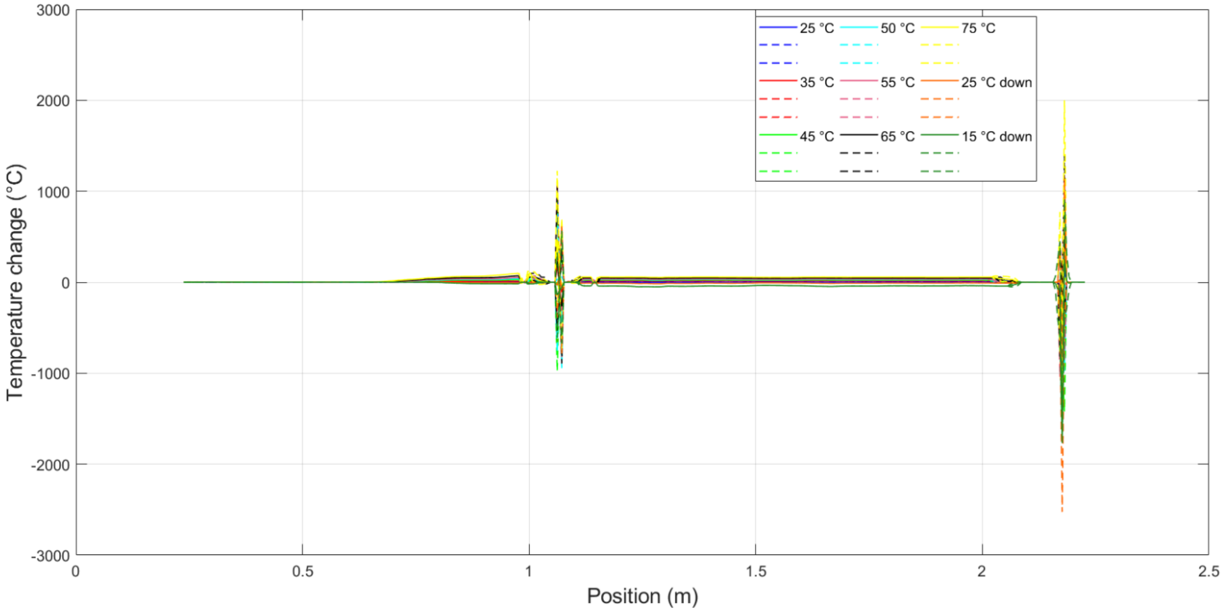

Figure 7.9: Temperature change along the entire sensing range extension.

Considering the central portion of the fibre, the changes in temperature detected are (Fig. 7.10):

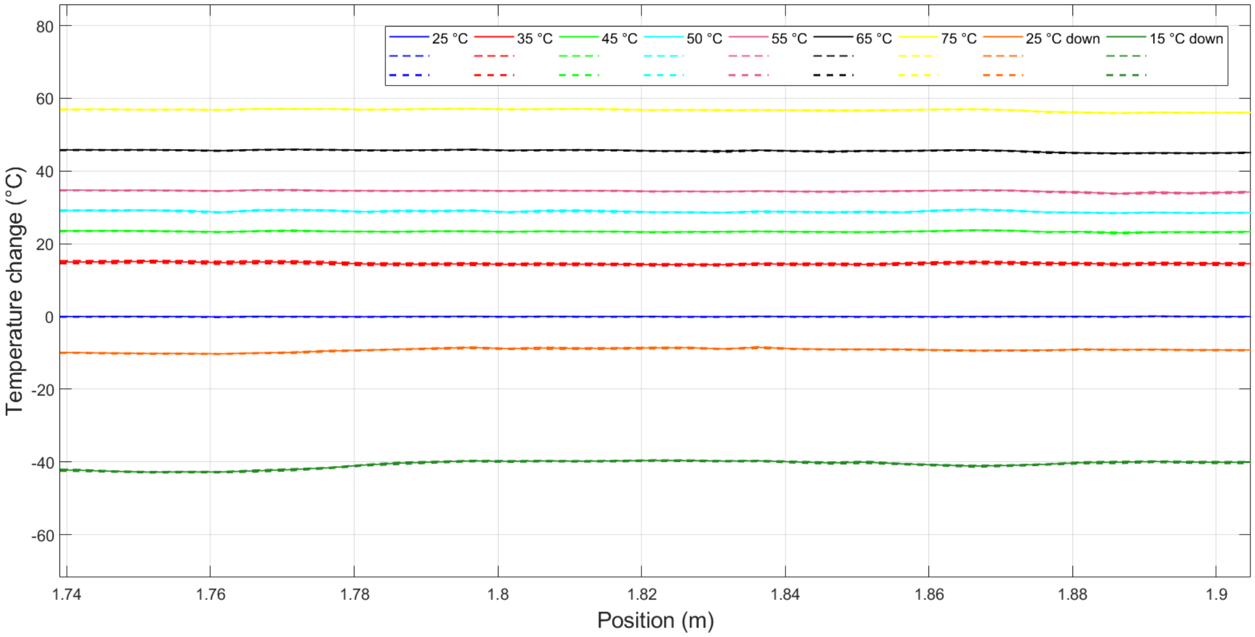

Figure 7.10: The changes in temperature detected in the central portion of the fibre. For each temperature, the solid line is the mean value, the dashed lines the positive and negative standard deviations.

Tab. 7.12 shows the comparison between the reference sensor measurements and the distributed sensor.

Table 7.12: Comparison of the measurements between reference and distributed sensors.

REFERENCE SENSOR	DISTRIBUTED SENSOR (T_{REF}=25.3 °C)
25.3 °C	25.28 °C
35.3 °C	39.88 °C
45.4 °C	48.69 °C
50.3 °C	54.21 °C
55.3 °C	59.79 °C
65.2 °C	70.88 °C
75.35 °C	82.09 °C
24.95 °C	16.08 °C
15.25 °C	−15.40 °C

7.2.3 Observations

The two high peaks shown in the temperature change in Fig. 7.9 are due to the connector of the fibre (the investigated optical fibre is connected to the instrument with a fibre patch cable because of the instrument connector is delicate and it could be damaged by recurrent removals) and to the end of the fibre itself. They are caused by the strong backscattering of the laser light and this makes the near length (10 cm - 20 cm) unreliable for sensing operations.

In the zoom of the acquired temperature change it is notable that the measurements are very precise (the standard deviations are almost zero) but they are not accurate because the resulting temperature are inconsistent with the temperature measured by the thermocouple. The cause of these discrepancies is attributable to the polymeric jacket covering the optical fibre. In fact, both the heating and the tension lead to negative spectral shift and thus, positive temperature change; whereas the cooling and the compression lead to positive spectral shift and thus, negative temperature change. (The softening of the polymer causes traction, the cooling causes compression).

The analysed optical fibre cannot be considered suitable for temperature sensing because of the unreliable measurements, and for this reason a further test has been performed with the same setup but analysing a SMF-28 optical fibre withou the polymeric jacket.

7.3 Temperature sensing with the fully distributed sensor without polymeric jacket

A possible cause for the high temperature errors of the previous distributed sensor is the polymeric jacket causing strain because itself is affected by the temperature changes.

Thus, the trial has been executed with the same set-up and steps of the previous one, but in this case a standard single-mode optical fibre SMF-28 without the polymeric jacket is investigated.

The parameters set in the OBR software interface are:

- Sensing range: 2.5 cm (the end of the optical fibre is included);
- Gauge length: 1 cm;
- Sensor spacing: 0.5 cm.

The temperature steps have been reduced to 25 °C, 50 °C, 75 °C and cooling to 25 °C.

Also in this trial the acquisition performed and mediated in the post-processing are 34 for each temperature level.

7.3.1 Results

Fig. 7.11 shows the temperature profile measured by the reference sensor (thermocouple).

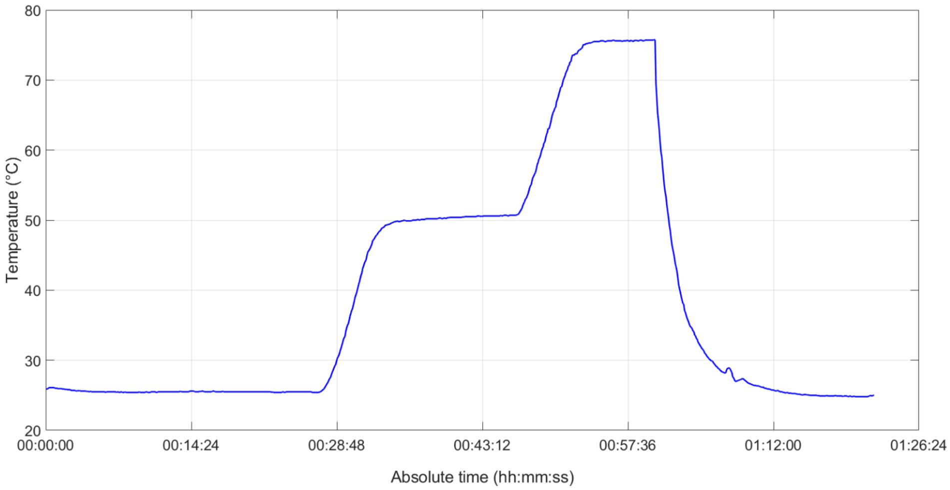

Figure 7.11: Temperature profile acquired by the thermocouple.

In Tab. 7.13 the temperature set in the climatic chamber and the real temperature detected by the reference sensor are reported:

Table 7.13: Set and real temperature (°C).

CLIMATIC CHAMBER	THERMOCOUPLE
25 °C	25.5 °C
50 °C	50.45 °C
75 °C	75.58 °C
25 °C	24.95 °C

Fig. 7.12 shows a central portion of the optical fibre.

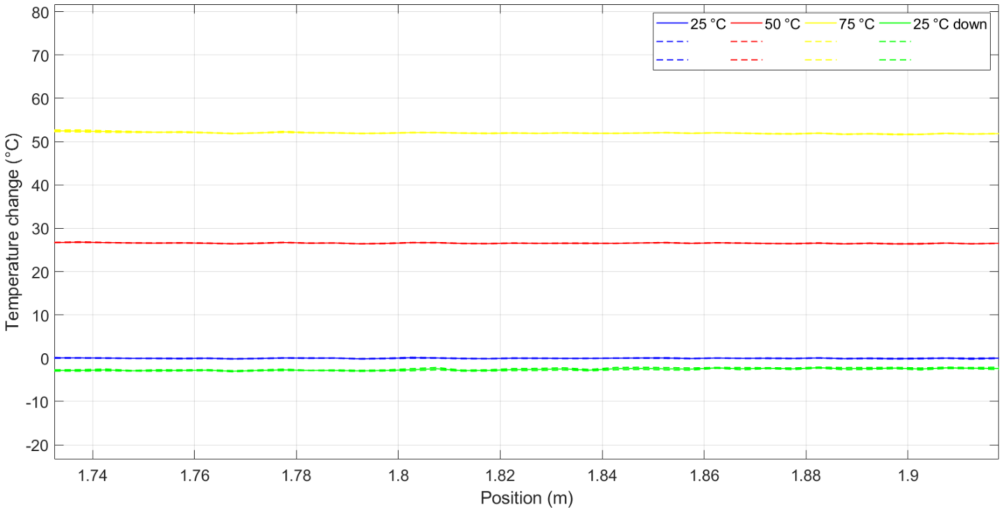

Figure 7.12: Central portion of the optical fibre.

Tab. 7.14 reports the values of the reference sensor measurement and the distributed bare sensor:

Table 7.14: Comparison of the measurements between the reference and the bare distributed sensors.

REFERENCE SENSOR	DISTRIBUTED SENSOR (T_{REF} = 25.5 °C)
25.5 °C	25.46 °C
50.45 °C	52.05 °C
75.58 °C	77.48 °C
24.95 °C	22.91 °C

7.3.2 Observations

The consideration about the accuracy and the precision of the sensing instrument are confirmed.
Moreover, it is worth noting that the absence of the polymeric jacket is beneficial because the temperature changes are more consistent with the applied temperatures. Even in this case, as like for the FBGs, there is a hysteresis due to the cooling of the sensor to the initial temperature.
The fully distributed sensing is an innovative typology for optical fibre sensors.
The high sensitivity of the instrument (0.8013 °C/GHz) allows high thermal resolution. The sensitivity is dimensionally the ratio °C/GHz because of the working principle relating the temperature change to the spectral shift with respect to the reference trace.

This optical fibre has suitable properties for sensing the temperature change, as seen by the results which present a gap not higher than 2 °C with respect to the reference measurements.

7.4 Additional tests to increase the spatial resolution

During the laser ablation procedure, it is necessary to measure the temperature with high resolution in space because the temperature decays with a rapid negative slope.
Using the same optical fibre of the previous trial (without polymeric jacket) different tests at room constant temperature (25 °C) have been performed.
The sensing range parameter has been maintained 2 m, the only changed parameters have been the *gauge length* and the *sensor spacing*. The sensor spacing is responsible of the spatial resolution, it can be seen in the number of points saved in the text file of each acquisition.
The selected gauge length is 0.999 cm.
The value of the sensor spacing increasing the spatial resolution up to 7 points per millimetre is 0.016 cm (Fig. 7.13) [38].

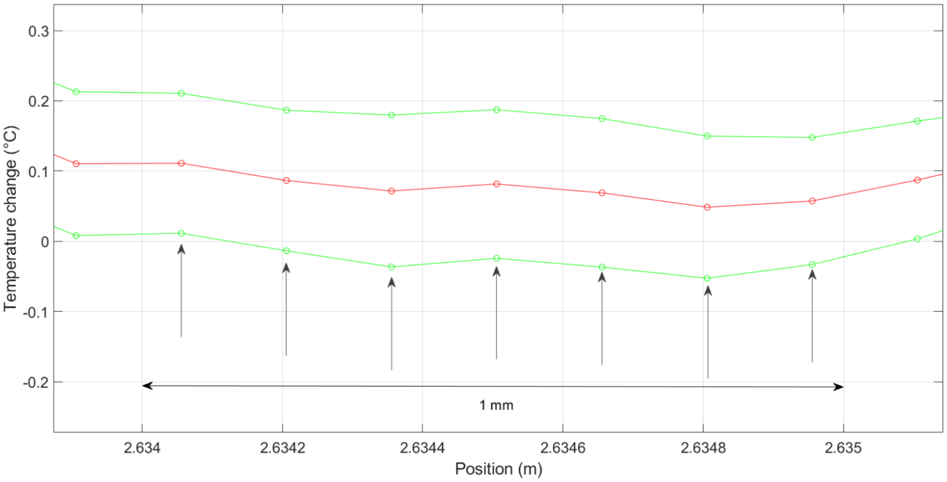

Figure 7.13: High spatial resolution (7 points in 1 mm).

7.4.1 Observations

The high spatial resolution achieved is beneficial for the laser ablation temperature monitoring.
The gauge length (0.999 cm) and the sensor spacing (0.016 cm) here evaluated have been maintained for the following tests.

Chapter 8

Optical fibre sensors behaviour in linear temperature distribution

The sensing capabilities of both the types of sensors described in the previous chapter have been tested on an *ad-hoc* setup with a metallic cantilever used to generate a linear thermal gradient.

The compared sensors are the FBG-array B, the fully distributed sensor without the polymeric jacket and two thermocouples.

Three tests are performed:

1. A preliminary test in the climatic chamber to evaluate the possible presence of the strain on the optical fibre sensors inserted into a thin glass capillary;
2. A comparative test of the sensors with the generation of a linear thermal gradient when they are simply covered with thermal grease;
3. A further comparative test of the sensors with the generation of a linear thermal gradient when they are inserted in the thin glass capillary and covered by thermal grease.

8.1 Measurement setup and instrumentation

The thermal gradient is obtained along the central tract of a thin (2 mm) aluminium bar shaped in order to obtain a larger smaller horizontal rectangle with larger quadrangular areas at the extremities.

The central tract is sized 4 cm × 1 cm (Fig. 8.1 - A), is fixed to a polystyrene block sized 4.9 cm × 6.2 cm × 4 cm (Fig. 8.2 – H), has been milled to obtain a groove to host the optical fibres and drilled in three points spaced by 1 cm in which three thermocouples are fixed (Fig. 8.1 – B).

The larger areas are maintained at different temperatures during the test, inducing the generation of the thermal gradient.

Fig. 8.1 shows the top view of the setup.

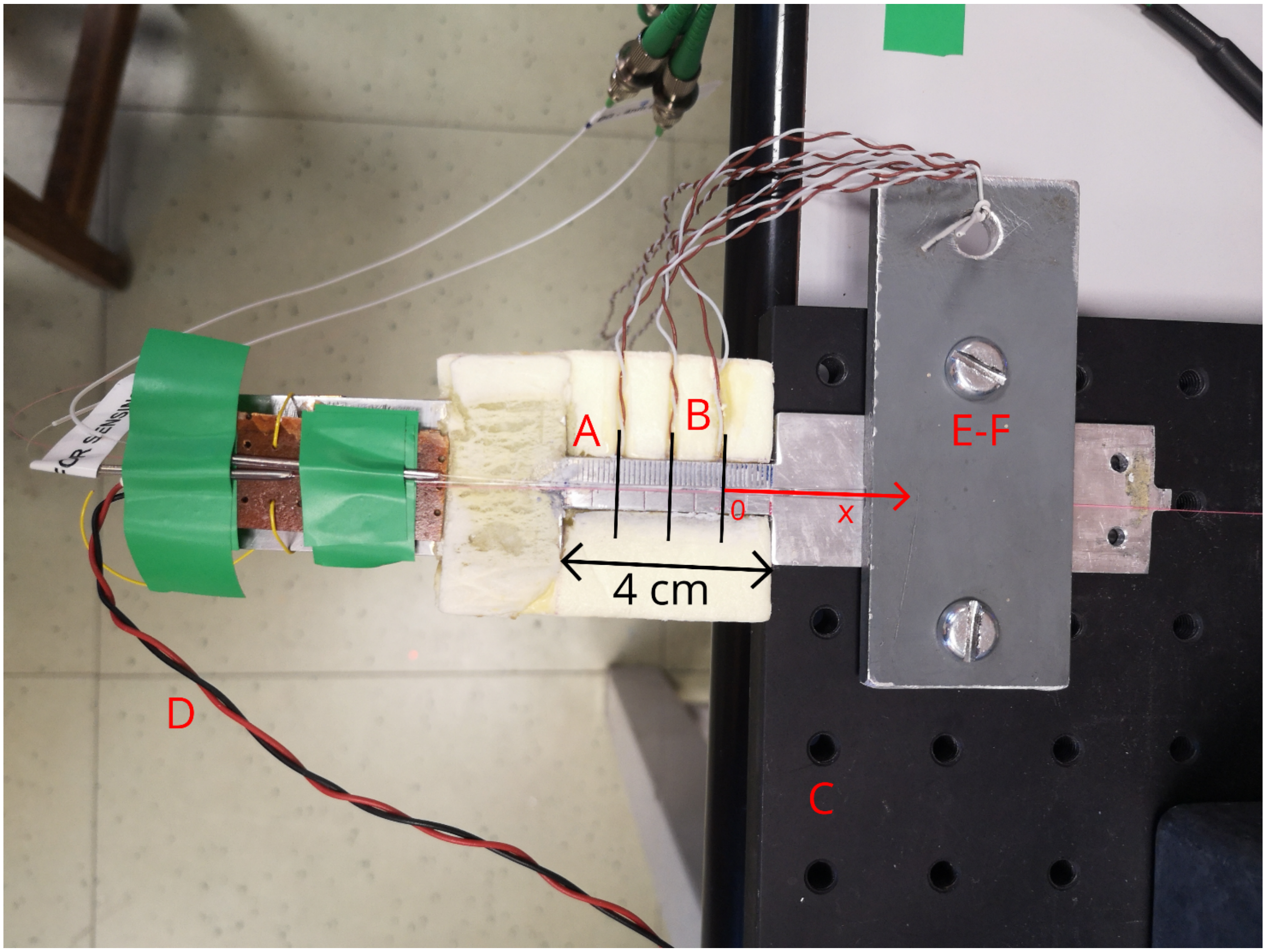

Figure 8.1: Top view of the setup.

The right side of the setup (in the top view) is the cold side, it is fixed with a transverse bar with two skews (Fig. 8.1 – E-F) to a large solid metal breadboard (Fig. 8.1 - C) with high thermal inertia.
The left side of the setup in Fig. 8.1 is the hot side.

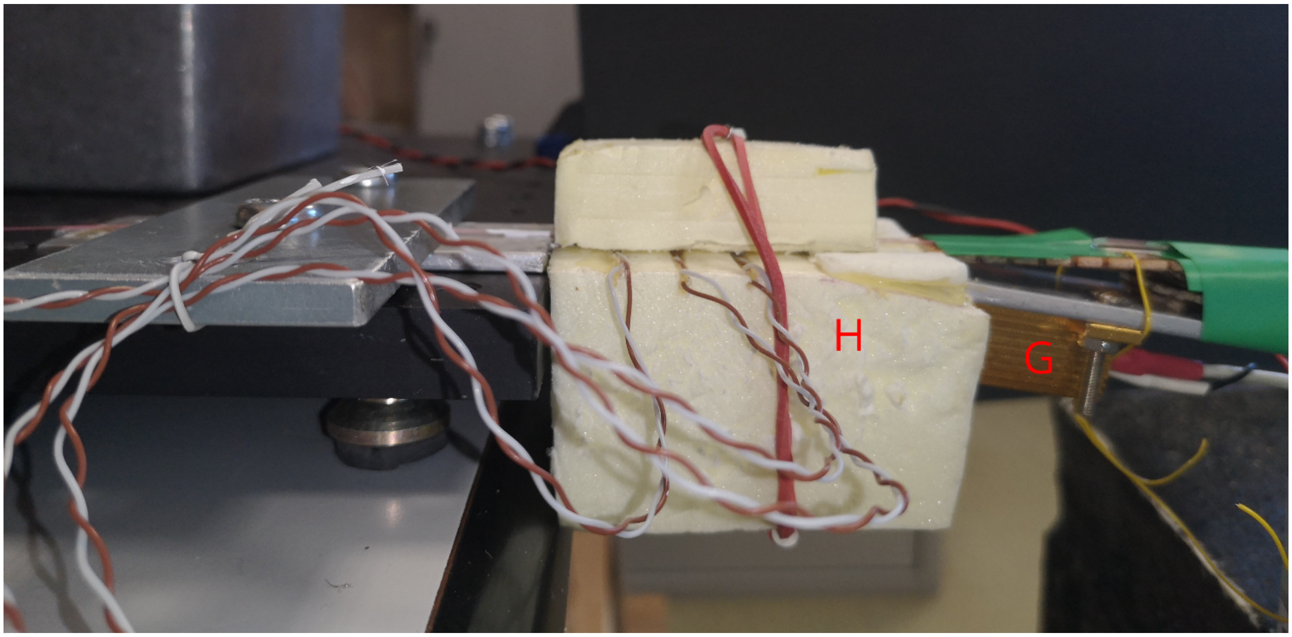

Figure 8.2: Left side of the setup.

In the side view it is shown the resistor (Fig. 8.2 – G) fixed under the side of the setup brought at high temperature by Joule effect.
The $4\,\Omega$ resistor is powered by the power supply connected with the wires D of Fig. 8.1, the dissipated power $P{=}RI^2$ heats that side of the bar.
The central 4-cm-long bar is between a thermal source (the powered resistor) and a thermal sink (the metal breadboard). The temperature profile is, thus, linear along the central bar (Fig. 8.3).

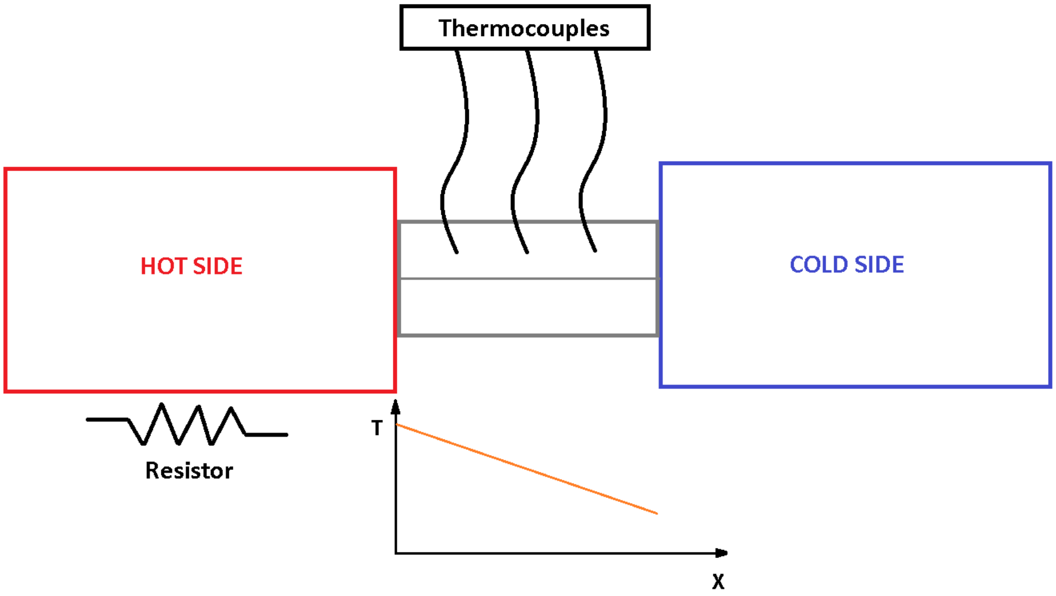

Figure 8.3: Scheme of the obtained temperature profile.

The instrumentation needed for the procedure is:

- The setup described above;
- Two National instrument T-type exposed-junction thermocouples with the measurement devices NI USB-TC01; the thermocouples have been placed in the first and third holes drilled in the metallic bar. The data saving interval is 1 s. Two points are sufficient to interpolate a linear profile.
  - Resolution: 0.0625 °C typical;
  - Temperature error: less than 2.5 °C2.5 (T$>$ 0 °C);
  - Maximum sample rate: 4 S/s;
  - ADC resolution: 20 bits.
- DC power supply HP E3610A. It is necessary to cause the resistor to dissipate heat and increasing the temperature of the hot side.
- Optical interrogator Micron Optics HYPERION si155, described in Chapter 5. Acquisition rate: 1 kHz; data saving interval in a text file: 1 s.
- Optical backscatter reflectometer OBR 4600 by Luna Technologies®, described in Chapter 5.
- Software OBR V.3 with the *Distributed sensing option.*

- LabVIEW^{TM} remote control program installed on the PC connected to the OBR.
- Climatic chamber Vötsch VC 4018.
- Thin glass capillary: $\sim$ 1 mm external diameter, 10 cm length.
- Thermal grease.

The placing of the sensors has a common aspect for all the tests executed: the distributed sensor protrudes for a chose fixed length of 29.7 cm out of the analysed central portion of the bar because of the high reflection at the end of the fibre which causes the OBR instrument to be ″blind″ .

8.2 Climatic chamber

This test is preliminary, it is to indagate the possible presence of strain induced by the contact with the capillary and/or the contact with the other sensor.
The single-mode optical fibre (the distributed sensor) and the array B (quasi-distributed sensor) have been placed inside the capillary and in the groove of the setup and covered with the small polystyrene block kept in place by an elastic rub in order to to reduce temperature changes due to air convection, the array A has been placed on the surface of the lower shelf of the climatic chamber. The distributed sensor protrudes for 29.7 cm out of the studied central portion 4 cm-long of the aluminium bar, for the reason explained above.
The data from the FBGs are acquired with the Micron Optics interrogator, remote controlled via the Ethernet connection with a PC in a different room. The channels to which the sensors are connected are the number 1 and number 4.
The peak detection rules set for the channels 1 and 4 are the same (130), identifying the peaks of 1.0 nm in width.
The acquisition time interval is set 1 s.
The OBR needs to be daily calibrated using the provided gold reflective tip, after that the investigated optical fibre sensor is connected, the parameters for sensing are set:

- Sensing range: 0.8 m;
- Gauge length: 0.999 cm;
- Sensor spacing: 0.016 cm.

Then the vertical cursor in the upper graph of the OBR software is placed in order to highlight the portion long 0.8 m (sensing range) of interest of the fibre.
At the initial temperature, in steady state, the reference trace is acquired.
The data saving now can be started, the remote control LabVIEW^{TM} program disables the OBR software interface and saves the data files.
Each acquisition generates a single text file beginning with the information header containing

also date and time of the acquisition.
The number of points to be sensed and saved is high (sensing range/sensor spacing = 0.8 m/0.016 cm = 5000 points) and slows the saving process.
The thermocouples are self-powered by the USB connection to the PC and their software self-launches. The user selects the temperature logging option, set the type of thermocouple connected (in this case both the thermocouples are T-type) and the data saving time interval (1 s).
Some initial acquisitions are performed for the three instruments at steady state and constant temperature. Then the experiment proceeds varying the temperature of the climatic chamber.
Four steps of temperature have been set: 20 °C, 35 °C, 50 °C and cooling to 20 °C.
The temperature has been measured also by the two thermocouples, assumed as reference sensors (Tab. 8.1).

Table 8.1: Set and real temperature of the test.

CLIMATIC CHAMBER	THERMOCOUPLES
20 °C	20 °C ; 20 °C
35 °C	36.2 °C ; 36.3 °C
50 °C	51.1 °C ; 51.2 °C
20 °C	20.9 °C ; 21 °C

To compare the values of temperature by the sensors, the temperature change from the OBR has been added to the initial temperature (20 °C).
In this case it is possible to compare also the array A with the other sensors because the temperature in the climatic chamber is constant everywhere.
The time for the entire systems to become isothermal with the chamber has been waited, as confirmed by the stability reached by the sensors.

8.2.1 Results

Figs. 8.4 and 8.5 represent the temporal evolution of the temperature acquired by the quasi-distributed sensors.

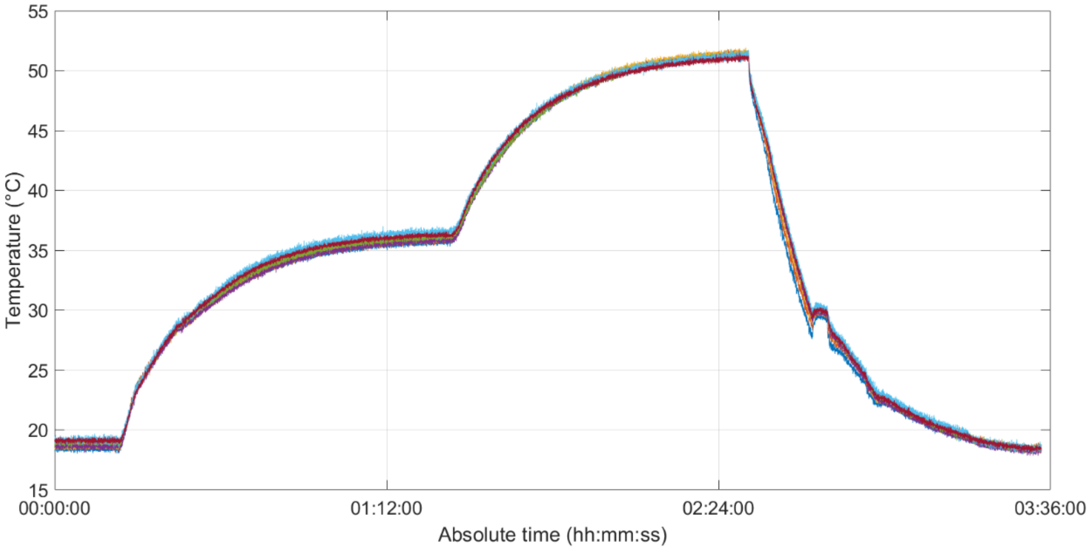

Figure 8.4: Temporal evolution of the temperature profile of FBGs in the array A.

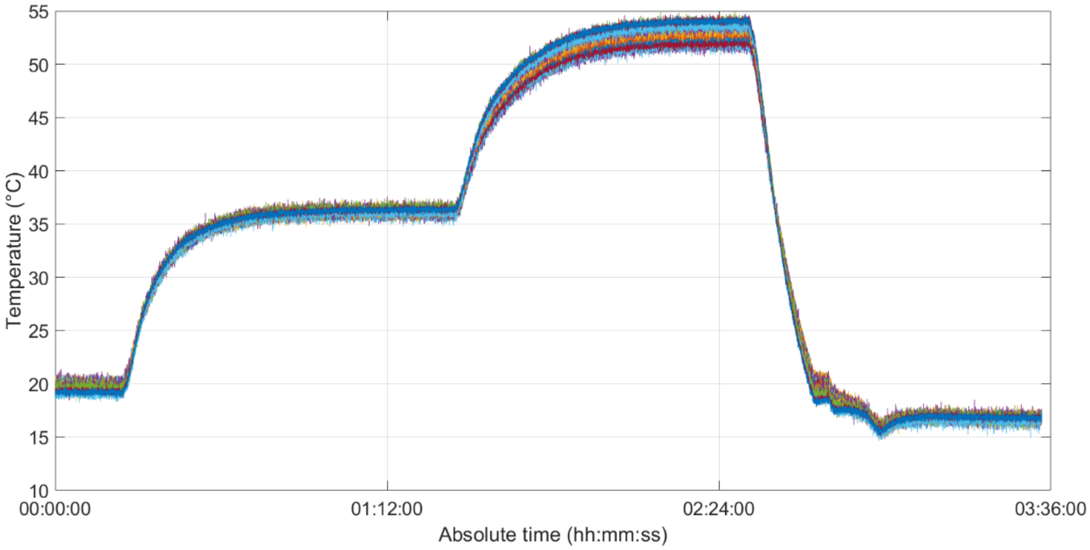

Figure 8.5: Temporal evolution of the temperature profile of the FBGs in the array B.

The data from the four sensors have been post-processed with a Matlab® code and compared in the following graphs and tables (Figs. 8.6, 8.7, 8.8, 8.9; Tabs. 8.2, 8.3, 8.4, 8.5). The x-axis has the origin in the colder thermocouple and its direction is toward the cold side of the setup.

The errors are the gap between the measured values of the thermocouple and each sensor.

Level 1: 20 °C**;** 20 °C

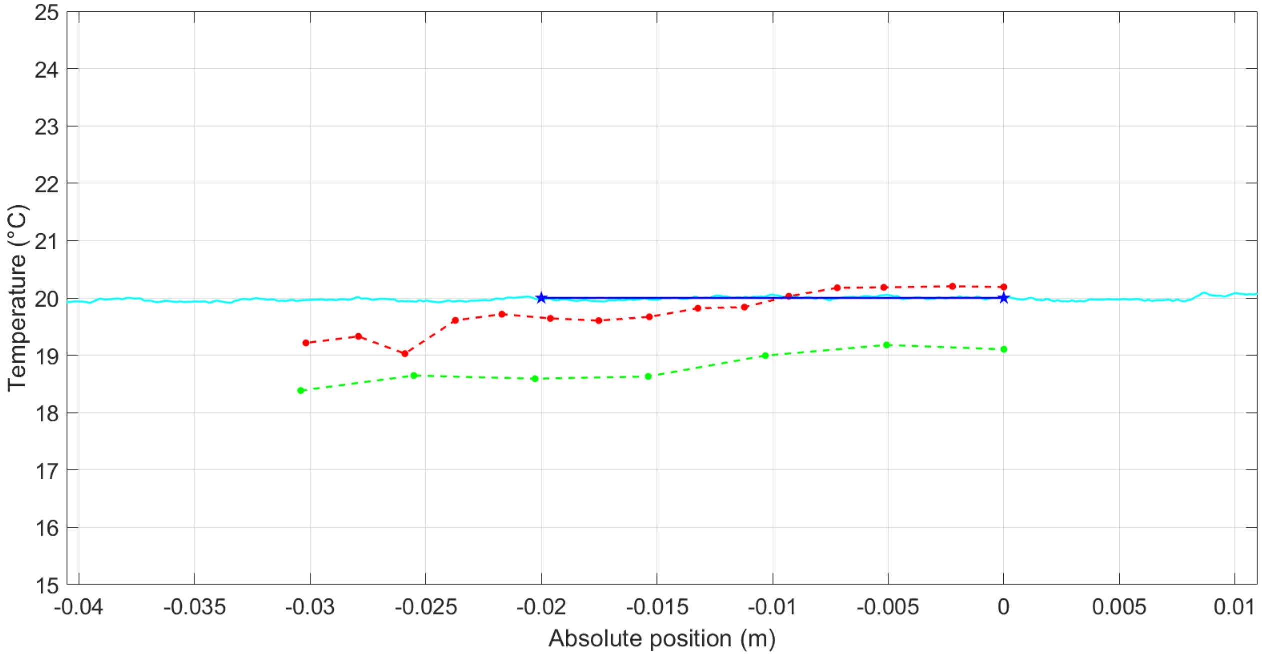

Figure 8.6: Level 1: 20 °C; 20 °C.
The cyan solid line is the temperature sensed by the distributed sensor (added with 20 °C);
the red dotted line is the temperature sensed by the array B inserted in the capillary with the distributed sensor. The bigger points are the FBGs;
the green dotted line is the temperature sensed by the array B;
the two blue stars are the thermocouple temperature values.

Table 8.2: Level 1: 20 °C; 20 °C.

	x = −0.02 m	x = 0 m
Array B	−0.36 °C	+0.19 °C
Array A	−1.41 °C	−0.9 °C
Distributed sensor	−0.02 °C	0 °C

Level 2: 36.2 °C**;** 36.3 °C

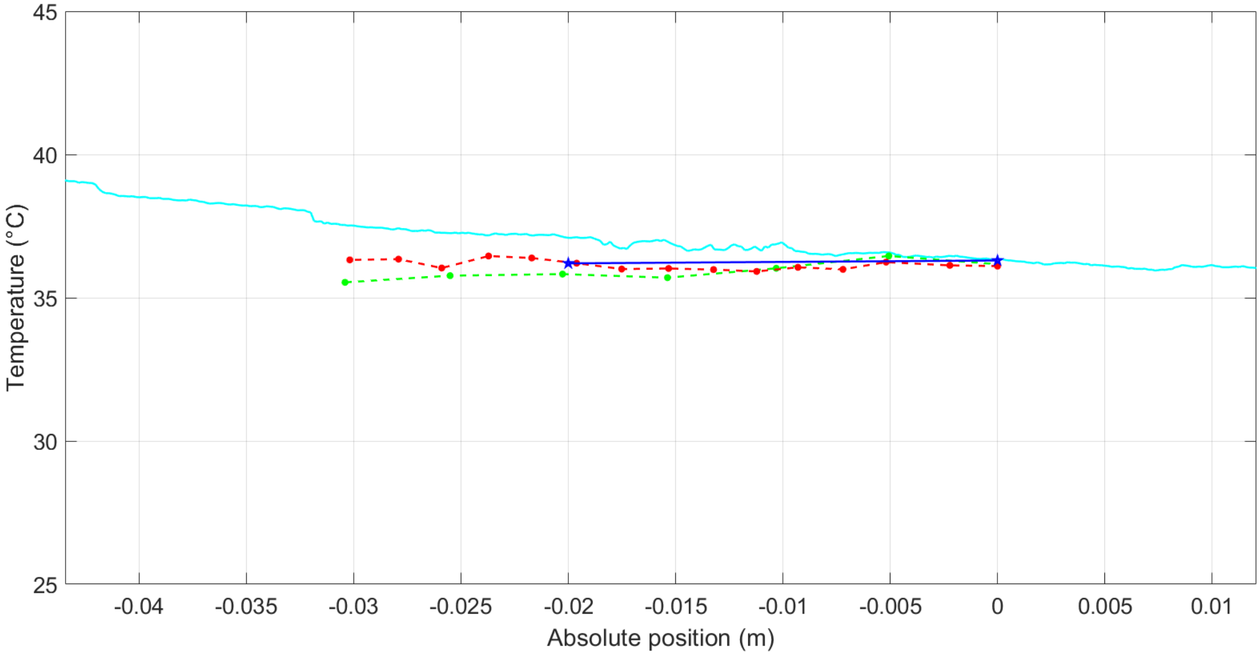

Figure 8.7: Level 2: 36.2 °C; 36.3 °C.
The cyan solid line is the temperature sensed by the distributed sensor (added with 20 °C);
the red dotted line is the temperature sensed by the array B inserted in the capillary with the distributed sensor. The bigger points are the FBGs;
the green dotted line is the temperature sensed by the array B;
the two blue stars are the thermocouple temperature values.

Table 8.3: Level 2: 36.2 °C; 36.3 °C.

	x = −0.02 m	x = 0 m
Array B	+0.01 °C	−0.2 °C
Array A	−0.38 °C	−0.13 °C
Distributed sensor	+0.9 °C	+0.04 °C

Level 3: 51.1 °C**;** 51.2 °C

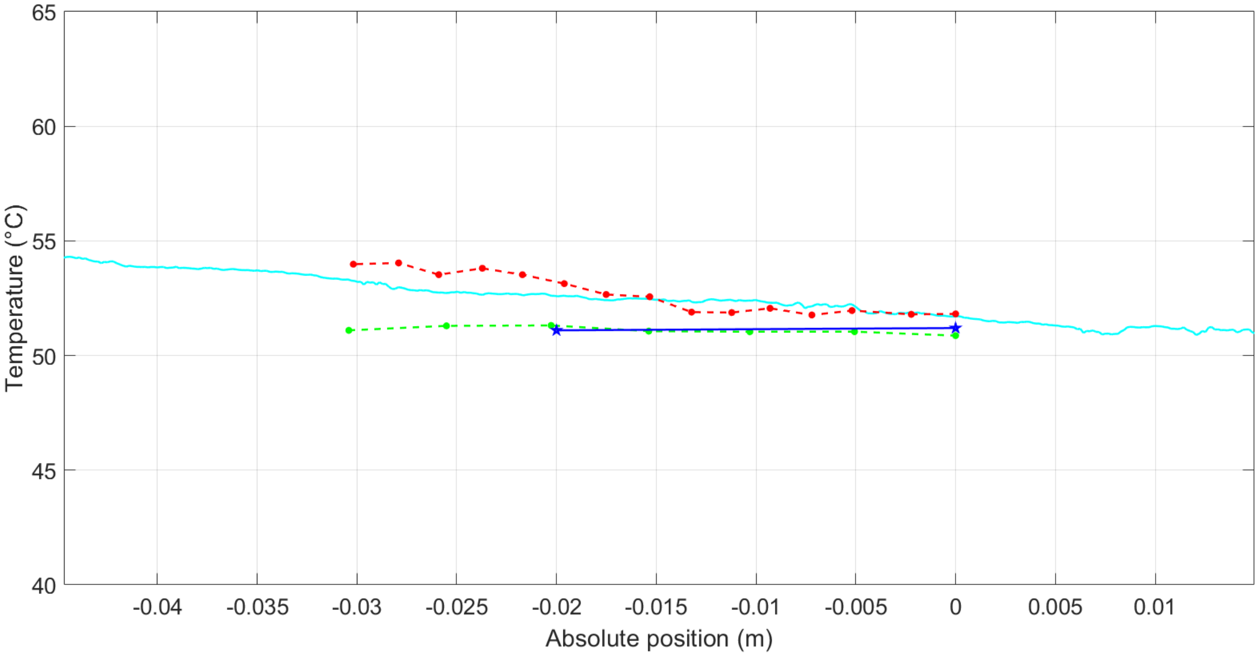

Figure 8.8: Level 3: 51.1 °C; 51.2 °C.
The cyan solid line is the temperature sensed by the distributed sensor (added with 20 °C);
the red dotted line is the temperature sensed by the array B inserted in the capillary with the distributed sensor. The bigger points are the FBGs;
the green dotted line is the temperature sensed by the array B;
the two blue stars are the thermocouple temperature values.

Table 8.4: Level 3: 51.1 °C; 51.2 °C.

	x = −0.02 m	x = 0 m
Array B	+2.04 °C	0.62 °C
Array A	+0.21 °C	−0.33 °C
Distributed sensor	+1.5 °C	+0.5 °C

Level 4: Cooling to 20.9 °C**;** 21 °C

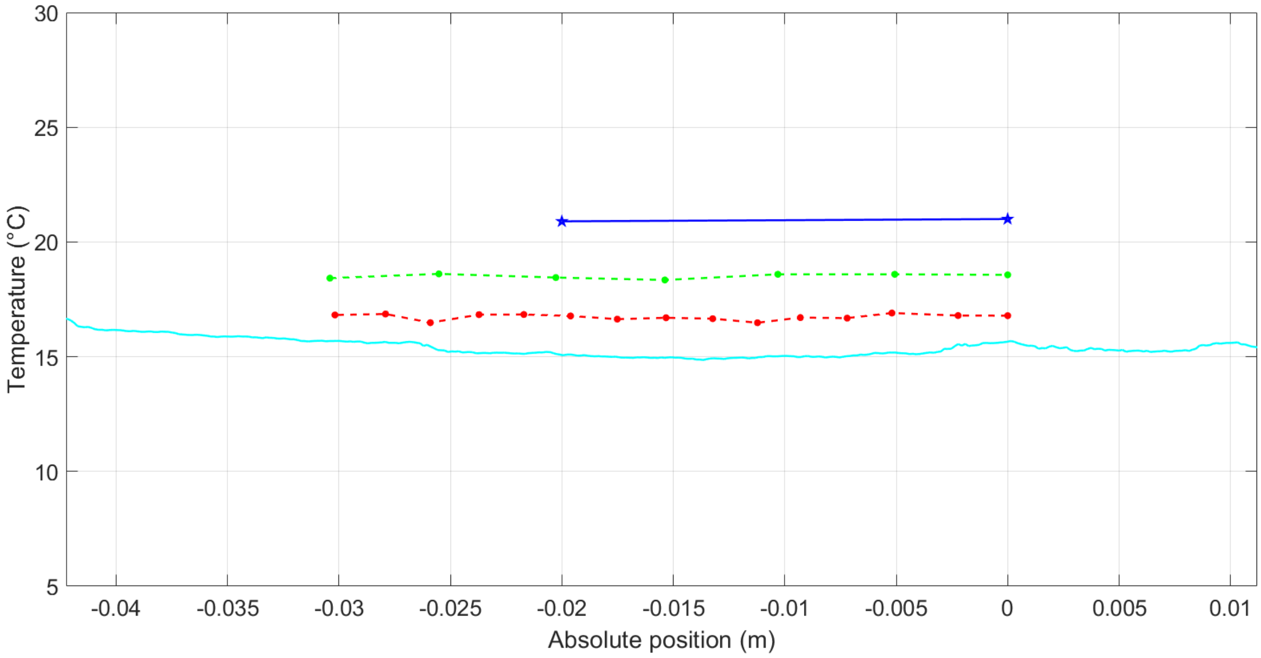

Figure 8.9: Level 4: Cooling to 20.9 °C; 21 °C.
The cyan solid line is the temperature sensed by the distributed sensor (added with 20 °C);
the red dotted line is the temperature sensed by the array B inserted in the capillary with the distributed sensor. The bigger points are the FBGs;
the green dotted line is the temperature sensed by the array B;
the two blue stars are the thermocouple temperature values.

Table 8.5: Level 4: Cooling to 20.9 °C; 21 °C.

	x = −0.02 m	x = 0 m
Array B	−4.12 °C	−4.21 °C
Array A	−2.45 °C	−2.43 °C
Distributed sensor	−5.81 °C	−5.35 °C

8.2.2 Observations

The results obtained show that the strain has not a negligible effect of the sensors.
The higher errors are obtained in the last step, showing that the optical fibres sensors have a hysteresis error. But the flatness of the profile is mantained.
The insertion of the sensors in the glass capillary prevents the strain from occurring due to

the upper polystyrene covering but it is probable that internal strain effects occur either due to the heated fibres friction each other or to the possible unwanted contact of the fibre with the glass of the capillary, leading thus to the temperature errors.

In the heating phase the errors are lower than the acceptance range, but become an issue when the temperature is cooled down to the initial level.

Both of the sensor present hysteresis, showed by the high temperature error, the temperature profiles are consistent with the constant temperature of the entire aluminium bar but are shifted by a negative offset which leads to the underestimation of the real temperature.

In this thesis project the hysteresis has not been investigated.

8.3 Tests with linear temperature gradient

This section is about the tests of the investigated sensors in condition of linear temperature gradient.

As previously described, the thermal gradient is obtained exploiting the Joule effect, the resistor dissipates the power power $P{=}R\ I^2$ and heats the central 4 cm-long aluminium bar. The heat flows from the hot side to the cold side and generates a linear thermal gradient.

Two temperature points measured by the thermocouples are sufficient to describe the linear profile.

The acquisitions by the instruments (Thermocouple, Micron Optics, OBR) are performed in the same way as the first test described and are started at the initial steady state, at constant temperature. Then the power supply is turned on and the resistor starts to dissipate. The power provided is the product of the current and the voltage supplied by the power supply. The control has mainly managed varying the current. When the high temperature level has been achieved the current is slightly varied to make the resistor dissipate heat which maintains the same thermal gradient for at least 5 minutes.

Two comparative tests are performed:

- Test with thermal grease;
- Test with capillary and thermal grease.

8.3.1 Thermal grease directly on the sensors

The sensors are placed directly in the groove on the central metallic bar, spread with the thermal grease and covered with the smaller polystyrene block, kept in place by an elastic rub to prevents the air convection to change the temperature. The distributed sensor protrudes of 29.7 cm out of the 4 cm-long central bar, as in the previous test.

The lower temperature level is the room temperature: the thermocouple measure 24.2 °C ($x = 0$ m) and 24.4 °C ($x = -0.02$ m).

At the higher temperature level, the thermocouples measure 0 °C ($x = 0$ m) and 47.54 °C ($x = -0.02$ m).

8.3.2 Results

The temperature profile measured by the thermocouples along the duration of the entire test is represented in Fig. 8.10:

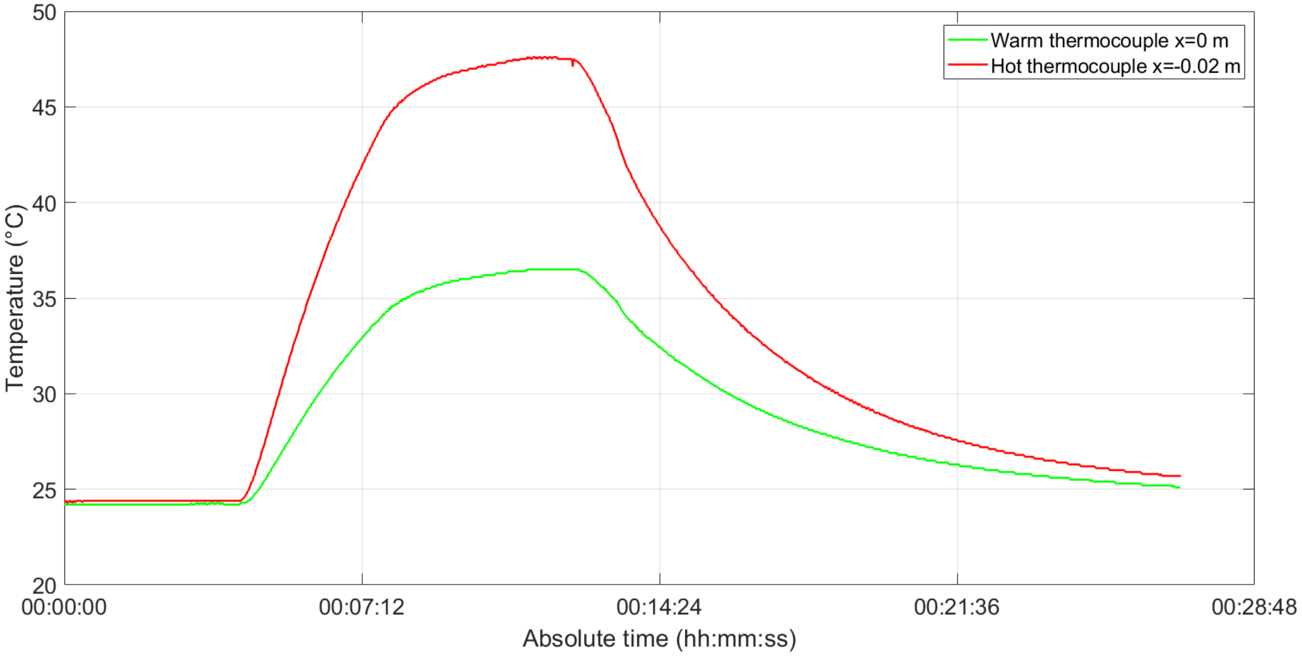

Figure 8.10: Temperature profile measured and saved by the thermocouples.

The comparison between the measurements of the sensors are post-processed with Matlab® code.

Fig. 8.11 is the initial steady state at constant room temperature.

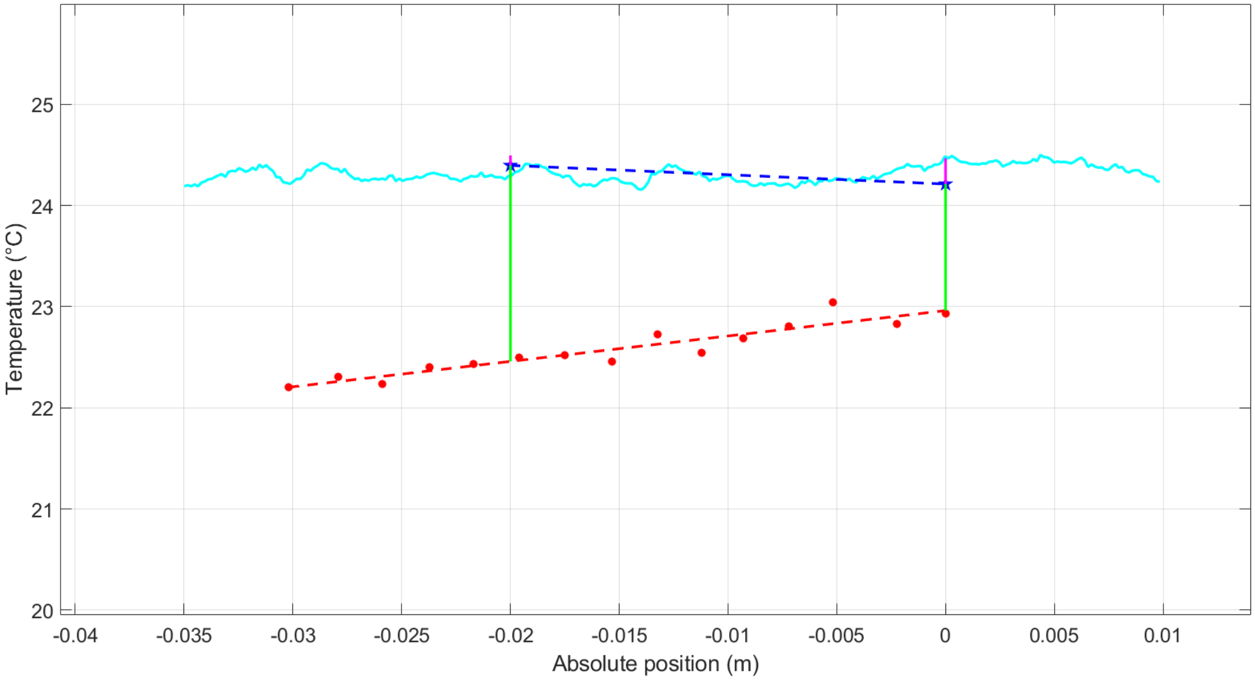

Figure 8.11: Test with thermal grease. Initial steady state at constant room temperature. The cyan solid line is the temperature sensed by the distributed sensor (added with 24.3 °C); the red dotted line is the temperature sensed by the array B. The bigger points are the FBGs; the two blue stars are the thermocouple temperature values.
The vertical bars indicate the temperature error of each sensor with respect to the relative thermocouple.

Tab. 8.6 reports the initial errors in temperature.

Table 8.6: Test with thermal grease. Temperature error of the initial steady state at constant room temperature.

	x = −0.02 m	x = 0 m
Array B	−1.94 °C	−1.25 °C
Distributed sensor	−0.1 °C	0.25 °C

Fig. 8.12 is the linear profile maintained for about 5 minutes.

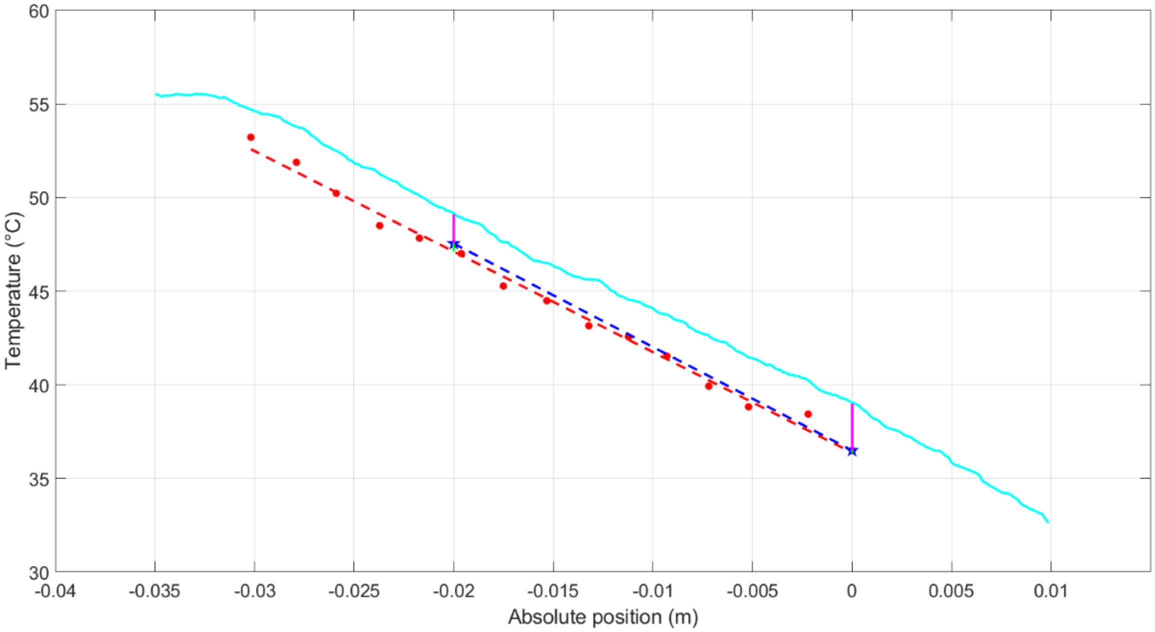

Figure 8.12: Test with thermal grease. Linear profile maintained for about 5 minutes.
The cyan solid line is the temperature sensed by the distributed sensor (added with 24.3 °C);
the red dotted line is the temperature sensed by the array B. The bigger points are the FBGs;
the two blue stars are the thermocouple temperature values.
The vertical bars indicate the temperature error of each sensor with respect to the relative thermocouple.

Tab. 8.7 reports the errors in temperature at the plateau temperature level.

Table 8.7: Test with thermal grease. Temperature error of the linear profile maintained for about 5 minutes.

	x = −0.02 m	x = 0 m
Array B	−0.43 °C	−0.12 °C
Distributed sensor	1.26 °C	2.5 °C

8.3.3 Observations

The quasi-distributed sensors present a reduction of the error of the measured temperature with the increase of the temperature. The dispersion of the values around the interpolating line is maintained with the increase of the temperature.
On the other hand, the distributed sensor decreases the accuracy (the error increases) with

the increase of the temperature but at the same time improves the precision (less fluctuations).
It is worth noting that the quasi-distributed sensors gains the initial gap and its slope corresponds to the slope of the reference thermal gradient.
At the plateau temperature the three profiles have the same slopes.
Even though the distributed sensor deviates a little from the reference profile at high temperature, its error is moderate and lower than a possible acceptable error of ± 3 °C.

8.3.4 Sensors in the glass capillary covered with thermal grease

The sensors are now inserted in a thin glass capillary (the distributed sensor protrudes of 39.7 cm out of the central bar, as explained in the introductory explanation), placed in the groove on the central metallic bar, coated with the thermal grease and covered with the smaller polystyrene block, kept in place by an elastic rub to avoid the air convection reduce the temperature changes.
The instruments perform some acquisitions at the initial steady state, at constant temperature.
Then the power supply is turned on and the resistor starts to dissipate.
The temperature level is achieved and maintained for some minutes with the control of the current in order to make the thermal gradient stay constant.
The initial temperatures measured by the thermocouples are 22.05 °C ($x = 0\,\mathrm{m}$) and 22.30 °C ($x = -0.02\,\mathrm{m}$).
The plateau thermal level is reached and maintained for about 8 minutes the thermocouples measure 35.148 °C ($x = 0\,\mathrm{m}$) and 46.61 °C ($x = -0.02\,\mathrm{m}$).

8.3.5 Results

The temperature profile measured by the thermocouples along the duration of the entire test is represented in Fig. 8.13.

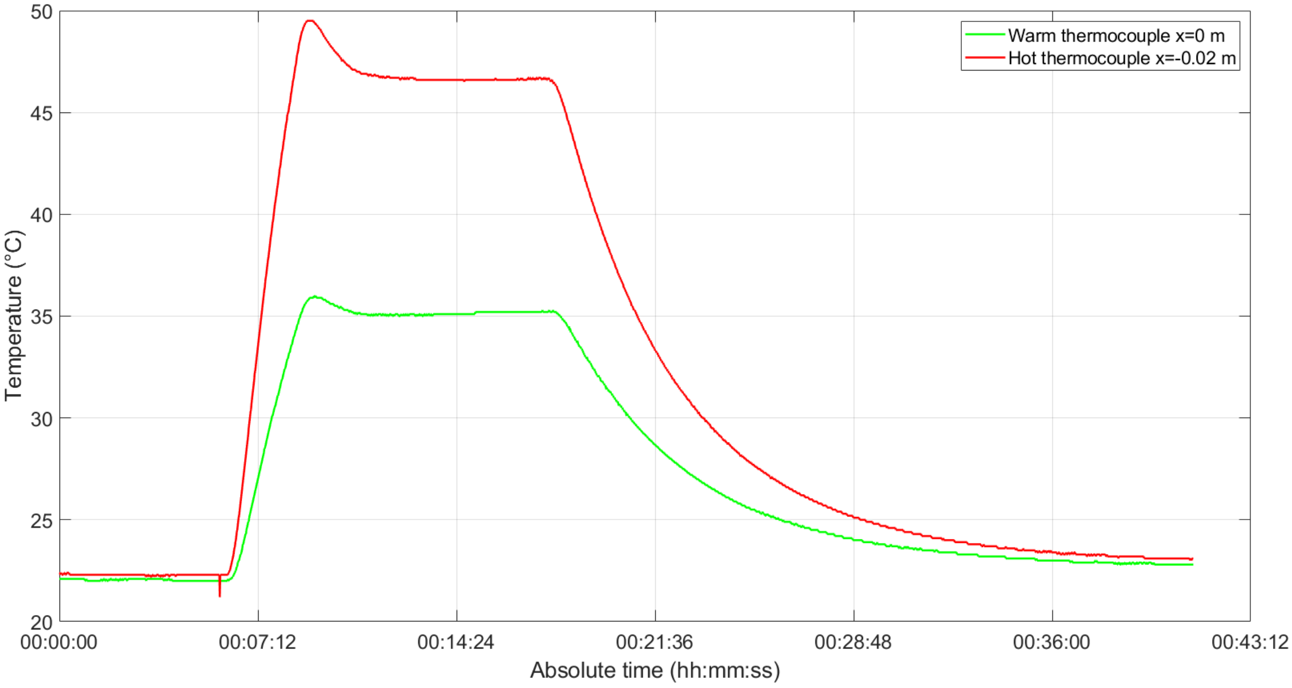

Figure 8.13: Temperature profile measured and saved by the thermocouple.

The comparison between the measurements of the sensors are post-processed with Matlab® code.

Fig. 8.14 is the initial steady state at constant room temperature.

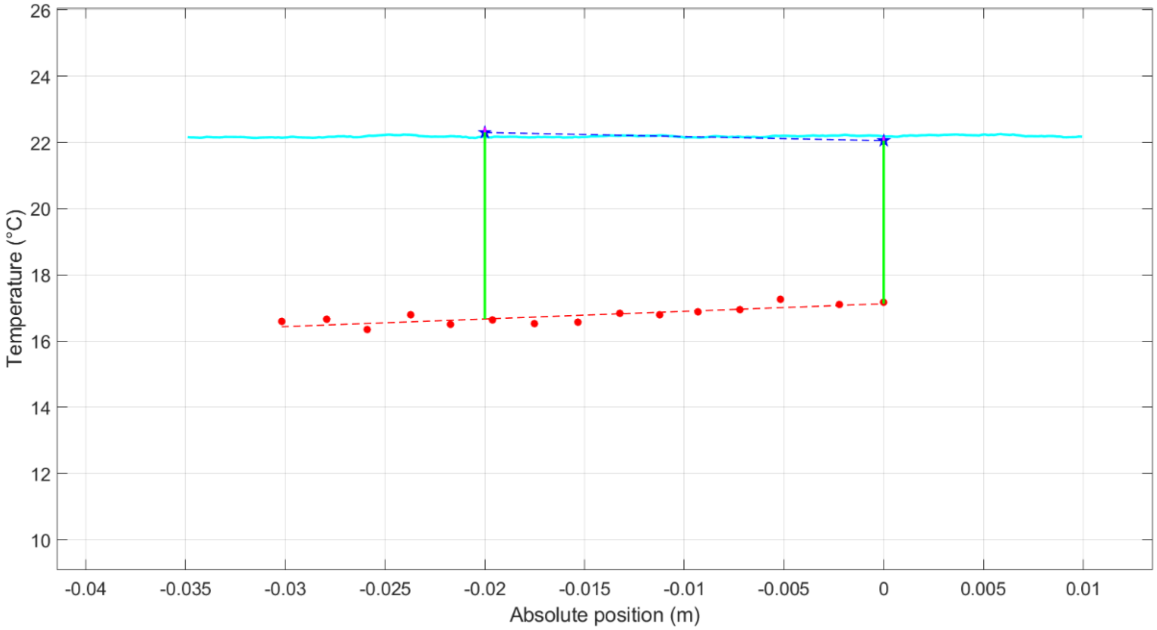

Figure 8.14: Test with capillary. The initial steady state at constant room temperature.
The cyan solid line is the temperature sensed by the distributed sensor (added with 22.2 °C);
the red dotted line is the temperature sensed by the array B. The bigger points are the FBGs;
the two blue stars are the thermocouple temperature values.
The vertical bars indicate the temperature error of each sensor with respect to the relative thermocouple.

Tab. 8.8 reports the initial errors in temperature.

Table 8.8: Test with capillary. Temperature error of the initial steady state at constant room temperature.

	x = −0.02 m	x = 0 m
Array B	−5.63 °C	−5.93 °C
Distributed sensor	−0.14 °C	0.12 °C

Fig. 8.15 is the linear profile maintained for about 8 minutes.

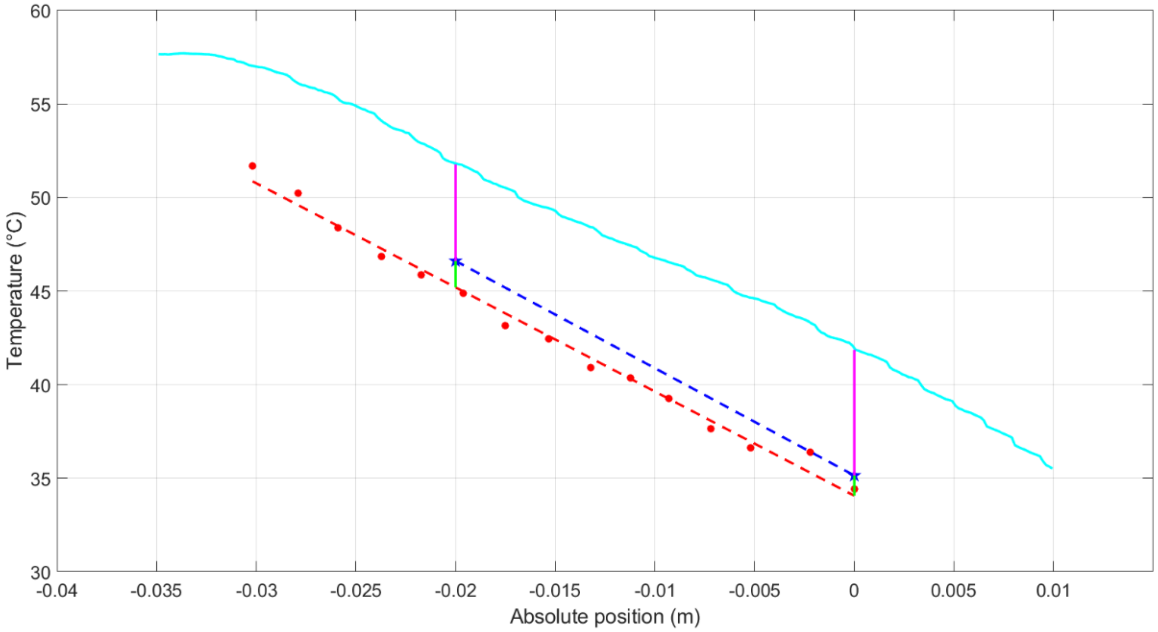

Figure 8.15: Test with capillary. Linear profile maintained for about 8 minutes.
The cyan solid line is the temperature sensed by the distributed sensor (added with 22.2 °C);
the red dotted line is the temperature sensed by the array B. The bigger points are the FBGs;
the two blue stars are the thermocouple temperature values.
The vertical bars indicate the temperature error of each sensor with respect to the relative thermocouple.

Tab. 8.9 reports the errors in temperature at the plateau level.

Table 8.9: Test with capillary. Temperature error of the linear profile maintained for about 8 minutes.

	x = −0.02 m	x = 0 m
Array B	−1.41 m	−1.08 m
Distributed sensor	5.16 m	6.71 m

8.3.6 Observations

As like in the previous similar test, the quasi-distributed sensor presents a high negative error with respect to the thermocouples reference measurements and, with the increase of the temperature, it regains almost all the error and follows the slope of the imposed thermal gradient.

The distributed sensor behaves in the same fashion as the previous test but worsens from the point of view of the error at high temperature. Even though the fluctuations are basically absent, confirming the high precision of the distributed sensing instrument.
A possible reason for the increase in the errors in this test, compared to the test with the fibres not inside the capillary, is the stain induced by the friction of the two fibres inside the capillary and by a contact force on the fibres by the capillary.
The strain effect cannot be distinguished by the temperature effect because they cause the same phenomenon, the shift of wavelength reaching the detector.

The results obtained without the insertion of the fibres inside the capillary lead to choose the use of them directly on the surface to measure the temperature, as bare sensors. And thus, it is possible to consider the possibility to employ these temperature sensors to measure the temperature during the laser ablation procedure.

Chapter 9

Experimental tests on ex-vivo bovine liver

The previous trials have showed promising results for the use of quasi-distributed and totally distributed optical fibre sensors.
The trail described in this chapter is the last for the thesis project.
It consists in the laser ablation of an *ex-vivo* bovine liver to test the sensing capabilities of the optical fibre sensors in a non-uniform condition.
The temperature measurements during the thermal ablation procedures are fundamental to monitor the progress and to optimize the results of the treatment in order to achieve a complete tumour ablation preventing from recurrences.

9.1 Setup measurements and instrumentation

The trial has been executed on a sliced *ex-vivo* bovine liver.
The setup can be divided in two main parts: the laser generation and delivery and the temperature measurements.

9.1.1 Laser generation and delivery

To emit and delivery the laser light has been used:

- High-power laser diode containing two diodes emitting different laser radiations (915 nm and 1470 nm)
- Multi-mode optical fibre patch cable (model M38L01 by Thorlabs Inc.)

The specifications are:

- Core: 200 µm;
- Cladding: 225 µm;
- Coating: 500 µm;
- Numerical aperture: 0.39;
- SMA-SMA connectors;
- Bare fibre terminator (model BFT1 by Thorlabs Inc.);
- Bare multi-mode optical fibre (HUV by CeramOptec® GmbH).

  The specifications are:

  - Core: 200 µm;
  - Polymeric cladding: 230 µm;
  - Polymeric coating: 500 µm;

- Bare multi-mode optical fibre (HUV by CeramOptec® GmbH).
  The specifications are the same of the multi-mode fibre above.
  In this case, the fibre has been damaged in the last 2 cm length with a NeHe laser, in order to remove the coating and the cladding and emit 64% of the laser light power laterally (and the remaining 36% from the final end).

The ablation procedure has been performed used a high-power laser diode. The laser module contains two laser diodes emitting laser radiation with different wavelengths in the infra-red spectrum: 915 nm (in the near infra-red spectrum) [37] and 1470 nm (in the short wavelength infra-red spectrum). The module contains a third diode whose emission is in the visible spectrum (green light) and has a supportive function of indicating where the laser is directed. The power is provided to each diode separately and the intensity of the laser beam is set either with a potentiometer on the instrument case or applying a voltage in the range 0-5 V. The maximum working temperature for the laser module is 55 °C and is controlled with an internal temperature sensor (LM35, sensitivity 10 mV/°C).
The device generates the laser radiation if the applied current is higher than a certain threshold. The laser radiation is guided to the target area in the liver through a sequence of optical fibres.
The sequence is composed by: a multi-mode optical fibre patch cable (SMA-SMA) connected to the laser module and a bare fibre optic terminator with SMA connector in which in inserted the bare multi-mode optical fibre (tip).

9.1.2 Temperature measurement

The temperature measurements have been performed with:

- array A described and characterized in Chapter 7;
- array B described and characterized in Chapter 7;
- Single-mode optical fibre without polymeric jacket described in the Chapter 7;
- Optical interrogator Micron Optics Hyperion si155 acquiring the Bragg wavelengths of the FBGs-array fibres connected to the channels 1 and 4 respectively. It has been controlled via Ethernet connection with a PC provided with the software Enlight.
  - Acquisition rate: 1 kHz;
  - Time interval data saving: 1 s.
- Optical backscatter reflectometer OBR4600 by Luna Technologies®. It is equipped with a portable PC, to which is connected via USB cable. The software OBR V.3 has been used to set the parameters and to perform the reference acquisition for the sensing mode, then it has been used a LabVIEW™ remote control program to perform acquisitions and to the data saving.

The parameters set in the OBR software interface are:

- Scan range of the tuneable laser: 1547.988 nm – 1590.731 nm;
- Gain: 12 dB;
- Group index: 1.47;
  - Sensing range: 1.9 m;
  - Gauge length: 0.999 cm;
  - Sensor spacing: 0.016 cm.
- Thermal imaging camera A325sc by FLIR® System, Inc.

The camera has been mounted on a tripod over the test location in order to frame the liver slice from above. The frame dimensions are: 21.6 cm × 15.2 cm.
The camera has been connected to a PC and some images and Matlab® matrices have been acquired and saved. The dimension of each pixel is 0.065 cm × 0.065 cm.
The quasi-distributed sensors have been placed parallel (array A) and perpendicular (array B) to the delivery multi-mode fibre on the bovine liver slice.
The OBR has a single connector and can perform sensing measurements on one optical fibre, for this reason, the fully distributed sensor is a single, long optical fibre and has been curved and crossed on the liver slice to be close to the quasi-distributed sensors.

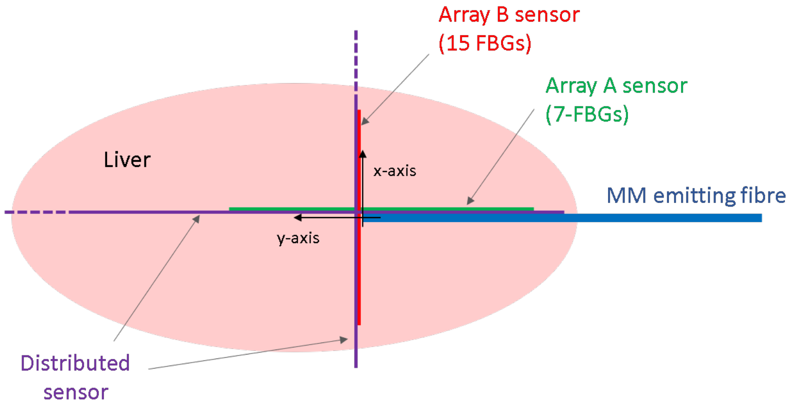

Figure 9.1: Scheme of the position of the delivery and sensing optical fibres on the liver slice.

The fibres have been placed manually without the capillary [40], therefore it is possible (and sometimes wanted) a distance between sensors in the same orientation; the delivery fibre as well could be placed with a slight, but still present, tilt.

With the configuration of the sensors described it has been possible the comparison between the quasi-distributed and the fully distributed optical fibre sensors in a non-uniform condition.

The reference system has been considered with the origin coincident with the delivery fibre end, the y-axis directed towards the direction of the laser radiation and the perpendicular x-axis is directed as a clock-wise 90-degrees-rotation of the y-axis, as shown in Fig. 9.1. The test has been performed after the OBR calibration with the gold reflective tip.

A slice of bovine liver has been placed on a plastic sheet.

The delivery and the sensing fibres have been placed on the liver slice and then covered with another slice to avoid the occurring of the air convection.

The reference trace for the distributed sensing has been acquired and the acquisitions of the three sensors have been started.

The laser has been set in power, emission mode and time duration of the procedure and turned on.

All the people in the space surrounding the workbench have been provided with protective glasses suitable for the infra-red wavelength.

The thermal camera has been used to roughly monitor in real-time the thermal evolution of the procedure.

Different tests have been performed:

1. Laser power: 2 W;

   λ : 915 nm;

   Duration: 3 minutes;

   Continuous wave emission;

   Un-damaged delivery fibre (only emission from the top).

2. Laser power: 2 W;

   λ : 915 nm;

   Duration: 3 minutes;

   Continuous wave emission;

   Damaged delivery fibre (lateral and top emission).
   This test has been continued without moving the setup configuration, increasing the power to 3.5 W for 3 minutes.

3. Laser power: 7 W;

   λ : 915 nm;

   Duration: 3 minutes;

   Pulsed wave emission;

   Frequency: 10 Hz;

   Duty cicle= 50%;

   Damaged delivery fibre (lateral and top emission).

The thermal camera images have been exploited to compare the investigated sensors with a reference sensor. But the temperature measurements have been exploited at the conclusion of each test. This because of the fact that the presence of the covering second slice to avoid the air convection effect to distort the acquisitions. In fact, a side effect of the second slide covering the setup is a reduced infra-red radiation detected by the camera.
To compare the sensors, the slices have been separated. The acquisitions of the fibre sensors in the seconds before the slice separation have been compared to the matrix acquisition of the camera in the few seconds after the slide separation [37]. The sensor acquisitions after the separation of the slices cannot be considered because of the strain induced with the moving of the setup.

9.2 Results

The results reported are the acquisitions during the laser ablation procedure and the final comparison with the thermal camera matrices saved at the end of the test, after the separation of the liver slices.
Since the FBG optical interrogator acquires less point than the distributed sensing instrument, the data saving is faster and there are more values in the same time unit. In the final comparison of each test are reported 30 seconds of FBG measurements and the measurement (or measurements) by the distributed sensing apparatus.
The reported tests have been performed only with the laser radiation at $\lambda = 915\,\text{nm}$ because the other higher laser wavelength $\lambda = 1470\,\text{nm}$ damaged irreversibly the sensors, making the

comparisons impossible.
The times reported are absolute time variation from the beginning of the test.

Test 1

Time: minute 1:20

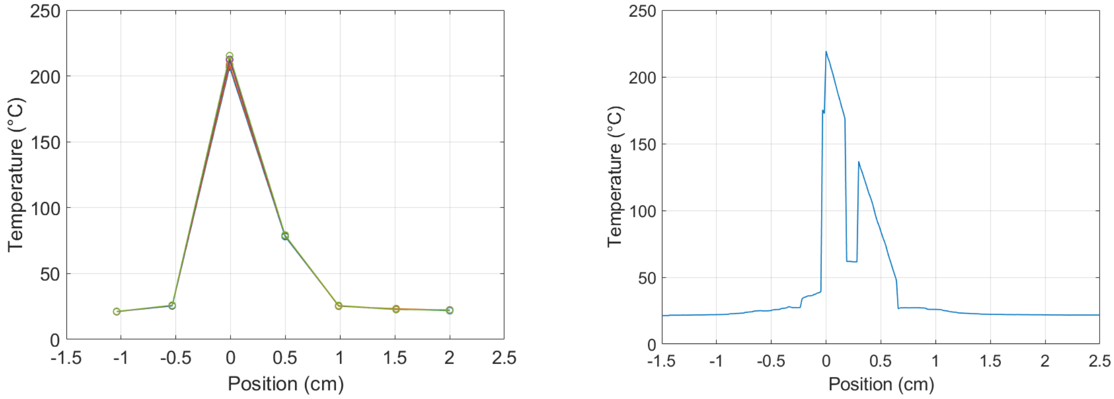

(a) Array A **(b)** Distributed sensor

Figure 9.2: Test 1 - minute 1:20. Temperature of the quasi-distributed and fully distributed sensors parallel to the delivery fibre.

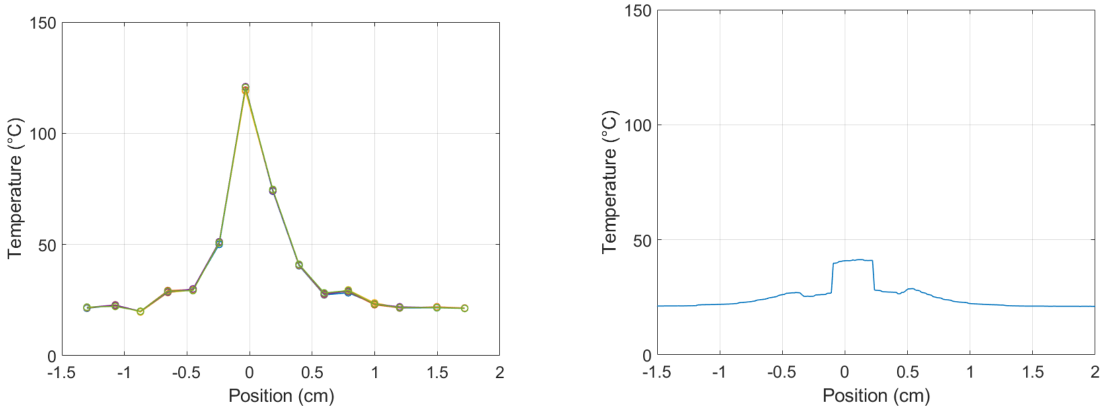

(a) Array B **(b)** Distributed sensor

Figure 9.3: Quasi-distributed and fully distributed sensors perpendicular to the delivery fibre. The distance between the sensors is 5 mm.

End of the test

The thermal camera acquired the matrix at minute 4:38 after the beginning of the test. The FBG acquisitions are in the 30-seconds-time interval (from minute 4:08 to minute 4:38) and the distributed sensor 13 seconds (minute 4:25) before the slice separation.

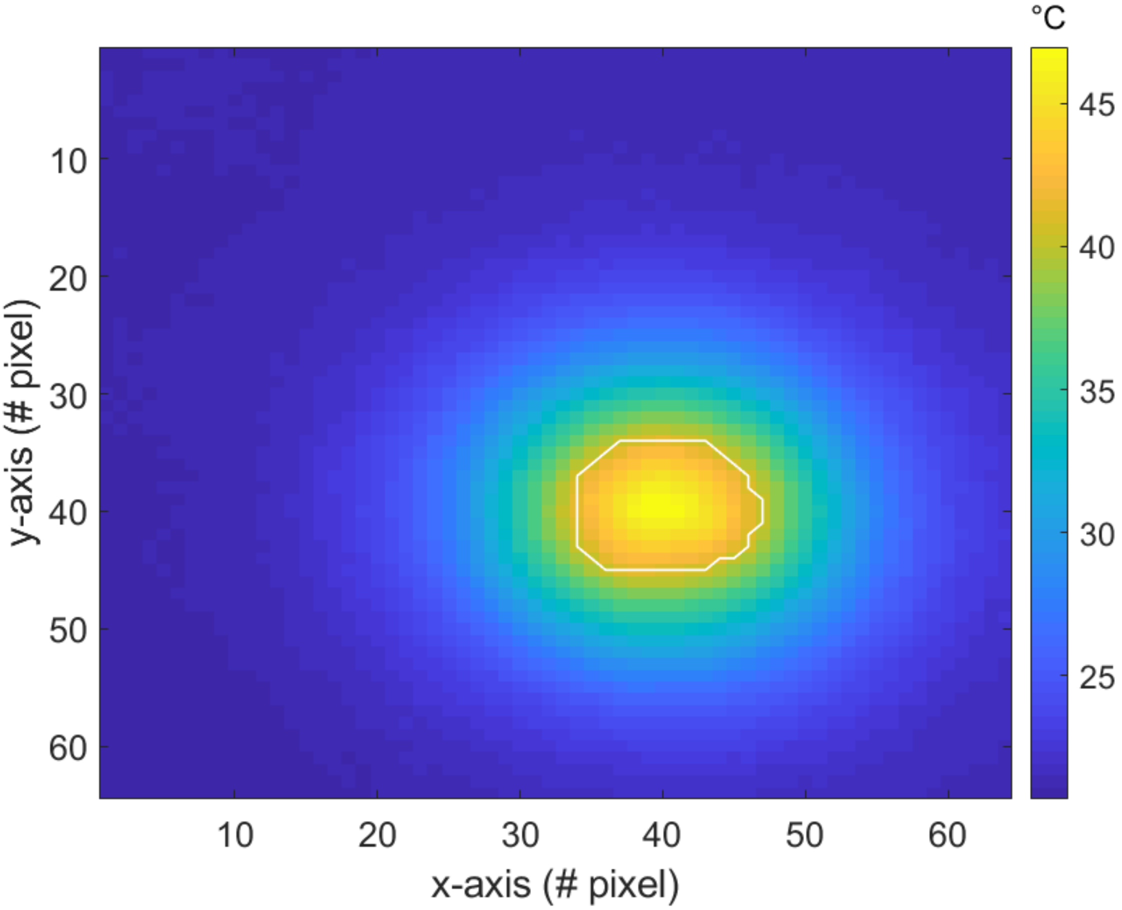

Figure 9.4: Test 1. Image from the matrix of the thermographic camera.

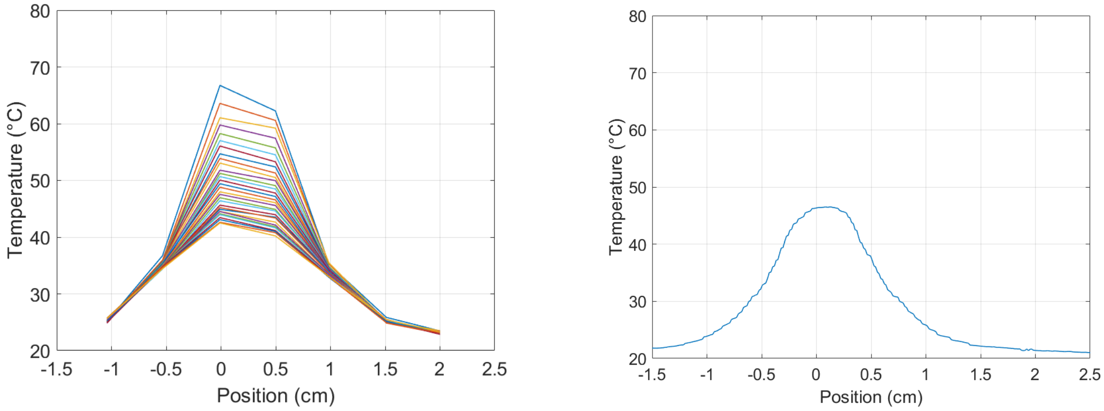

(a) Array A - minutes 4:08-4:38 **(b)** Distributed sensor - minute 4:25

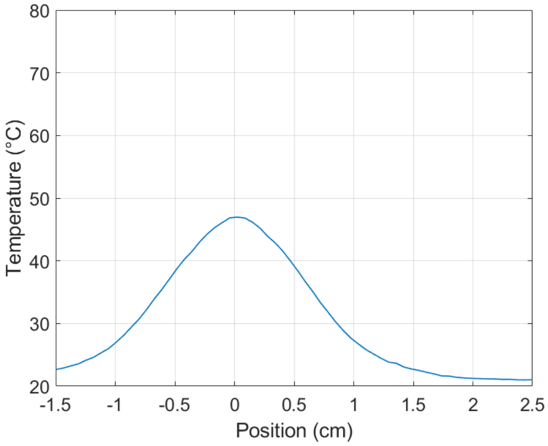

(c) Thermal camera - minute 4:38

Figure 9.5: Comparison of the temperatures measured along the parallel axis to the delivery fibre at the end of test 1.

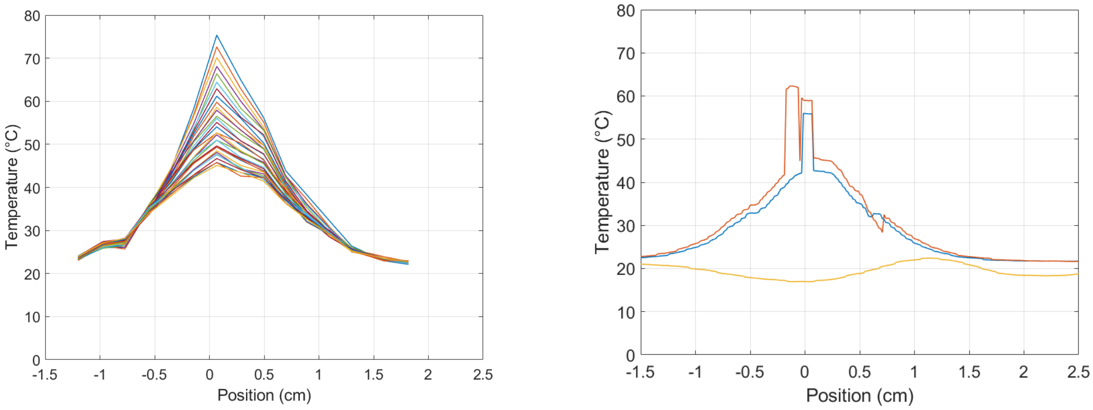

(a) Array B - minutes 4:08-4:38 **(b)** Distributed sensor - minutes 3:14; 3:54; 4:25

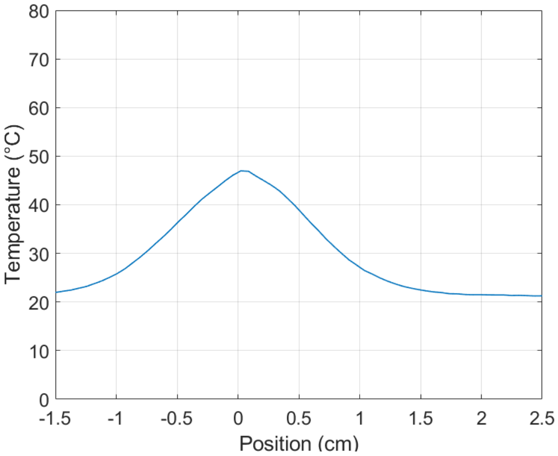

(c) Thermal camera - minute 4:38

Figure 9.6: Comparison of the temperatures measured along the orthogonal axis to the delivery fibre at the end of test 1. The distance between the optical fibre sensors is 5 mm.

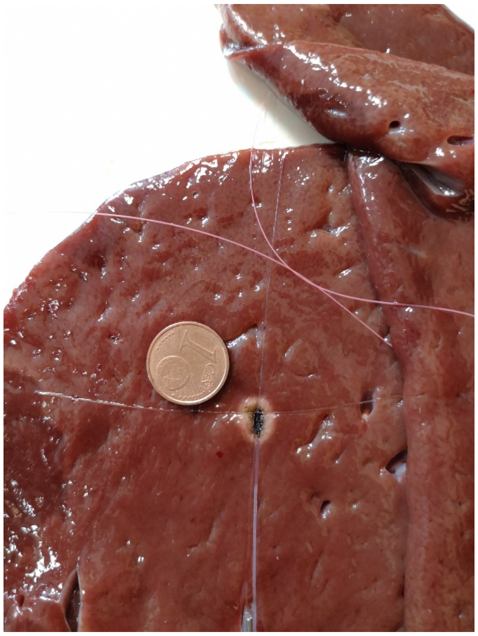

Figure 9.7: Lower slice at the end of test 1.

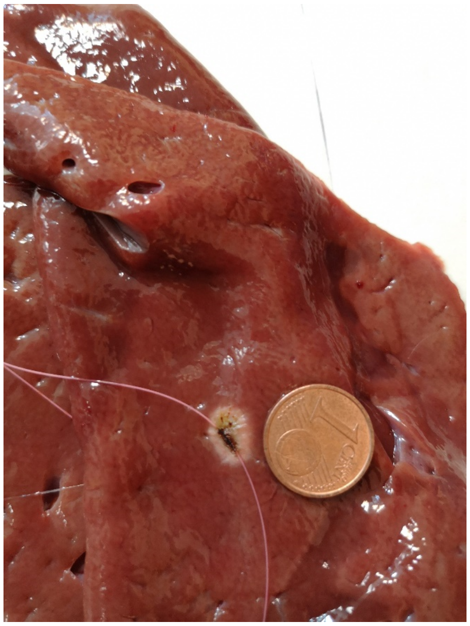

Figure 9.8: Upper slice at the end of test 1.

Test 2

Time: minute 0:55

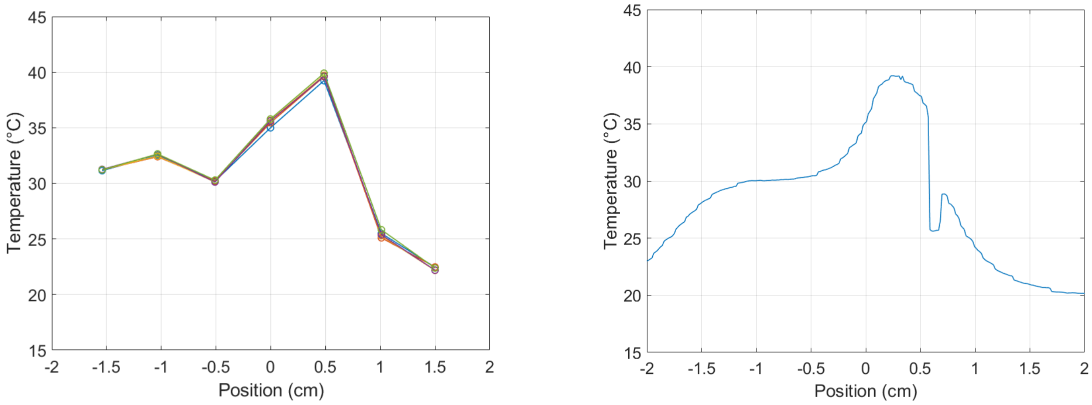

(a) Array A **(b)** Distributed sensor

Figure 9.9: Test 2 - minute 0:55. Temperature of the quasi-distributed and fully distributed sensors parallel to the delivery fibre.

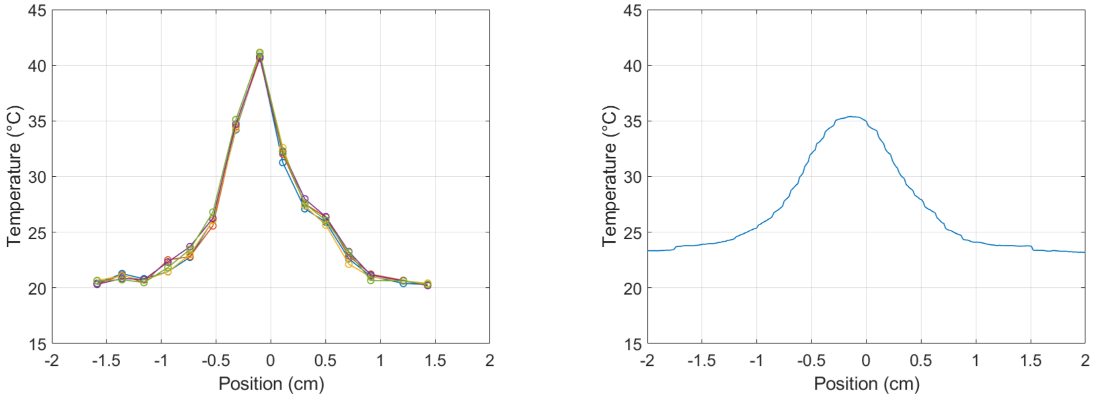

(a) Array B **(b)** Distributed sensor

Figure 9.10: Test 2 - minute 0:55. Temperature of the quasi-distributed and fully distributed sensors perpendicular to the delivery fibre.
The distance between the sensors is 1 mm.

Time: minute 1:22

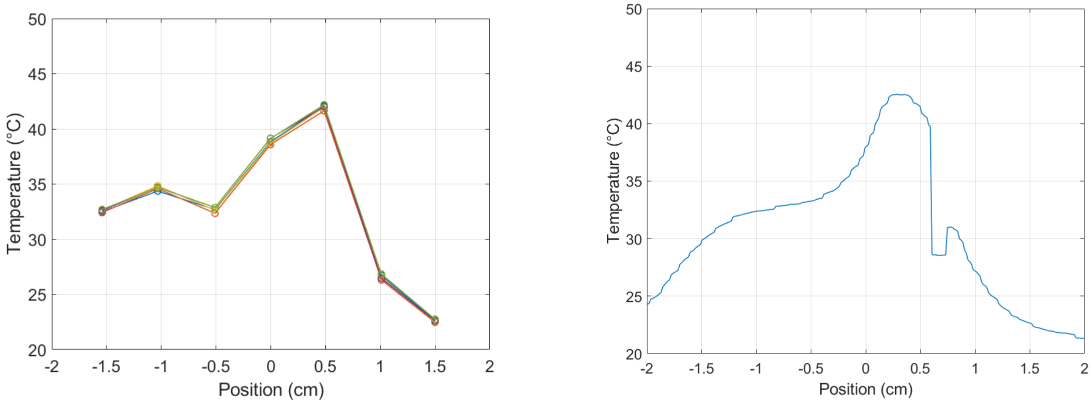

(a) Array A **(b)** Distributed sensor

Figure 9.11: Test 2 - minute 1:22. Temperature of the quasi-distributed and fully distributed sensors parallel to the delivery fibre.

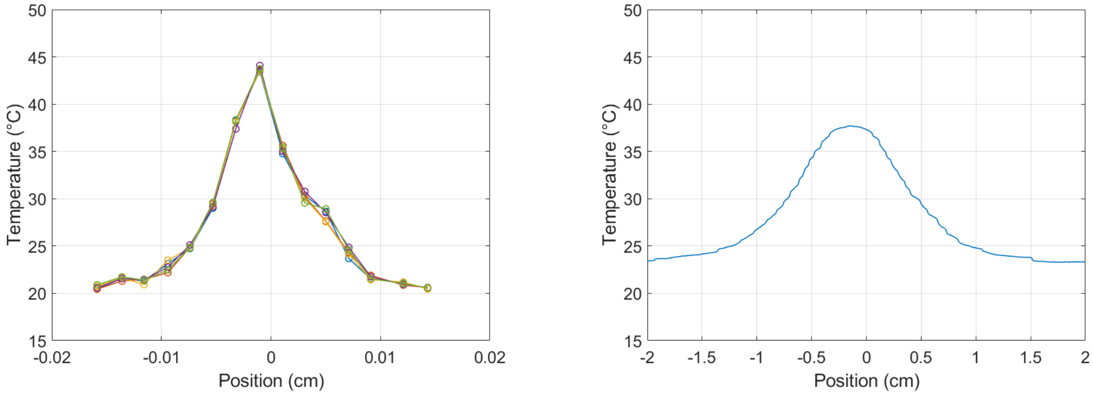

(a) Array B **(b)** Distributed sensor

Figure 9.12: Test 2 - minute 1:22. Temperature of the quasi-distributed and fully distributed sensors perpendicular to the delivery fibre.
The distance between the sensors is 1 mm.

Time: minute 2:47

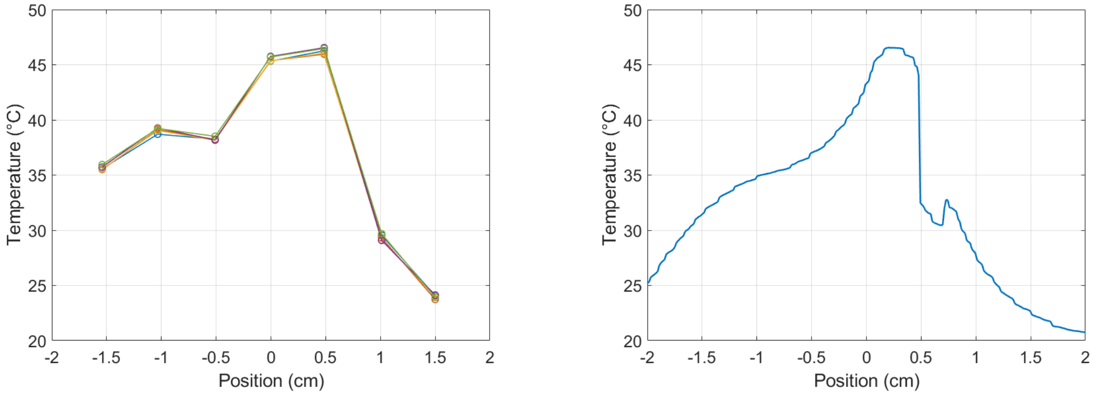

(a) Array A **(b)** Distributed sensor

Figure 9.13: Test 2 - minute 2:47. Temperature of the quasi-distributed and fully distributed sensors parallel to the delivery fibre.

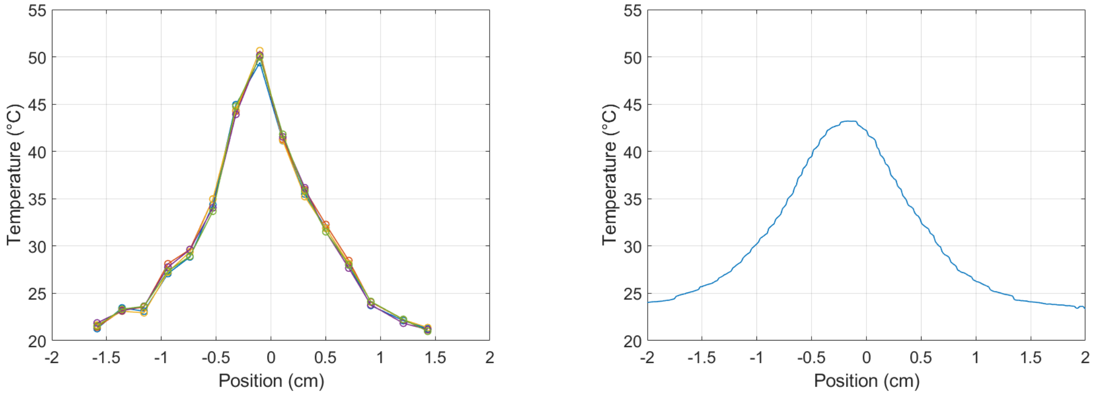

(a) Array B **(b)** Distributed sensor

Figure 9.14: Test 2 - minute 2:47. Temperature of the quasi-distributed and fully distributed sensors perpendicular to the delivery fibre.
The distance between the sensors is 1 mm.

Time: minute 3:15

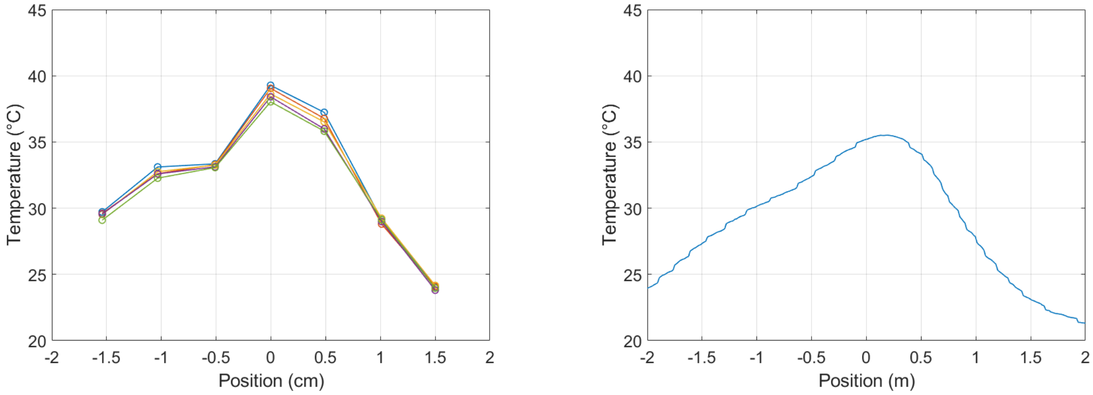

(a) Array A **(b)** Distributed sensor

Figure 9.15: Test 2 - minute 3:15. Temperature of the quasi-distributed and fully distributed sensors parallel to the delivery fibre.

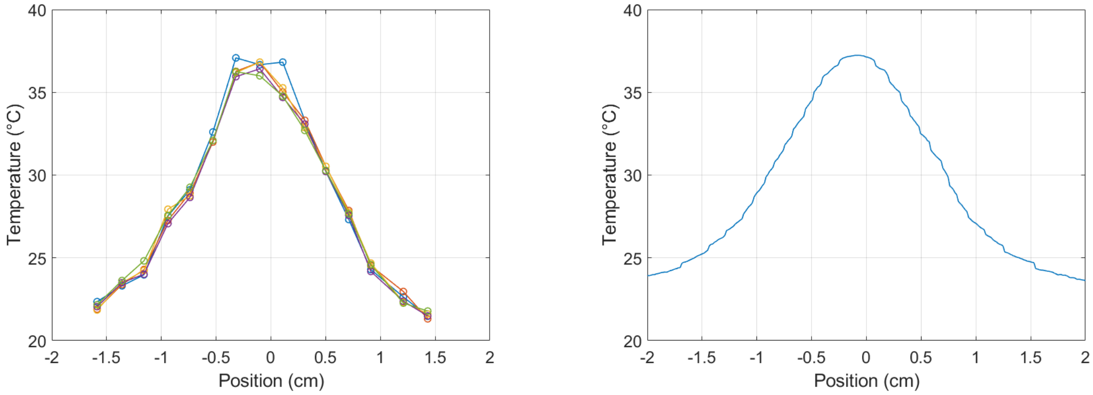

Figure 9.16: Test 2 - minute 3:15. Temperature of the quasi-distributed and fully distributed sensors perpendicular to the delivery fibre.
The distance between the sensors is 1 mm.

Time: minute 3:44

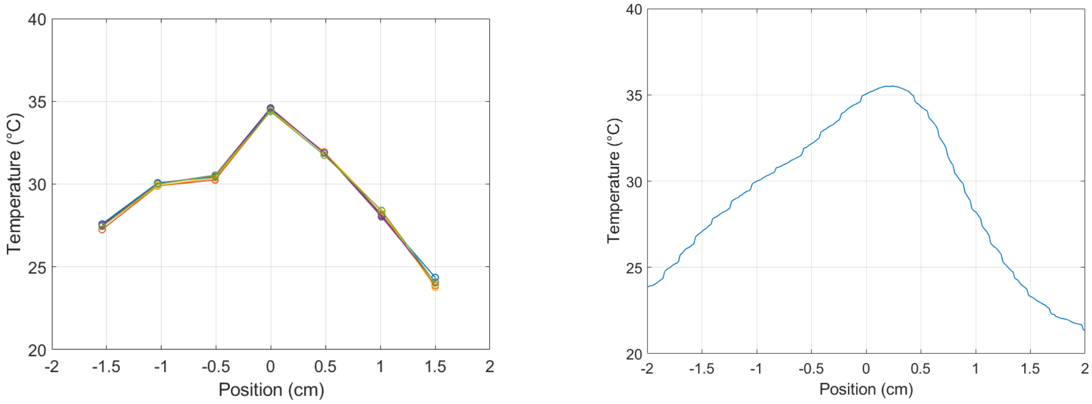

(a) Array A **(b)** Distributed sensor

Figure 9.17: Test 2 - minute 3:44. Temperature of the quasi-distributed and fully distributed sensors parallel to the delivery fibre.

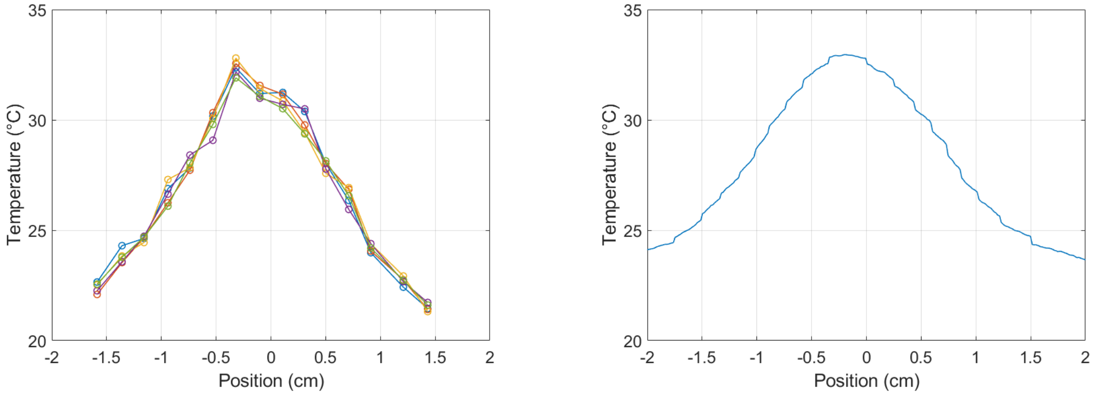

(a) Array B **(b)** Distributed sensor

Figure 9.18: Test 2 - minute 3:44. Temperature of the quasi distributed and fully distributed sensors perpendicular to the delivery fibre.
The distance between the sensors is 1 mm.

End of the test

The thermal camera acquired the matrix at minute 12:51 after the beginning of the test. The FBG acquisitions are in the 30-seconds-time interval (from minute 12:21 to minute 12:51) and the distributed sensor at minutes 12:28 and 12:56.

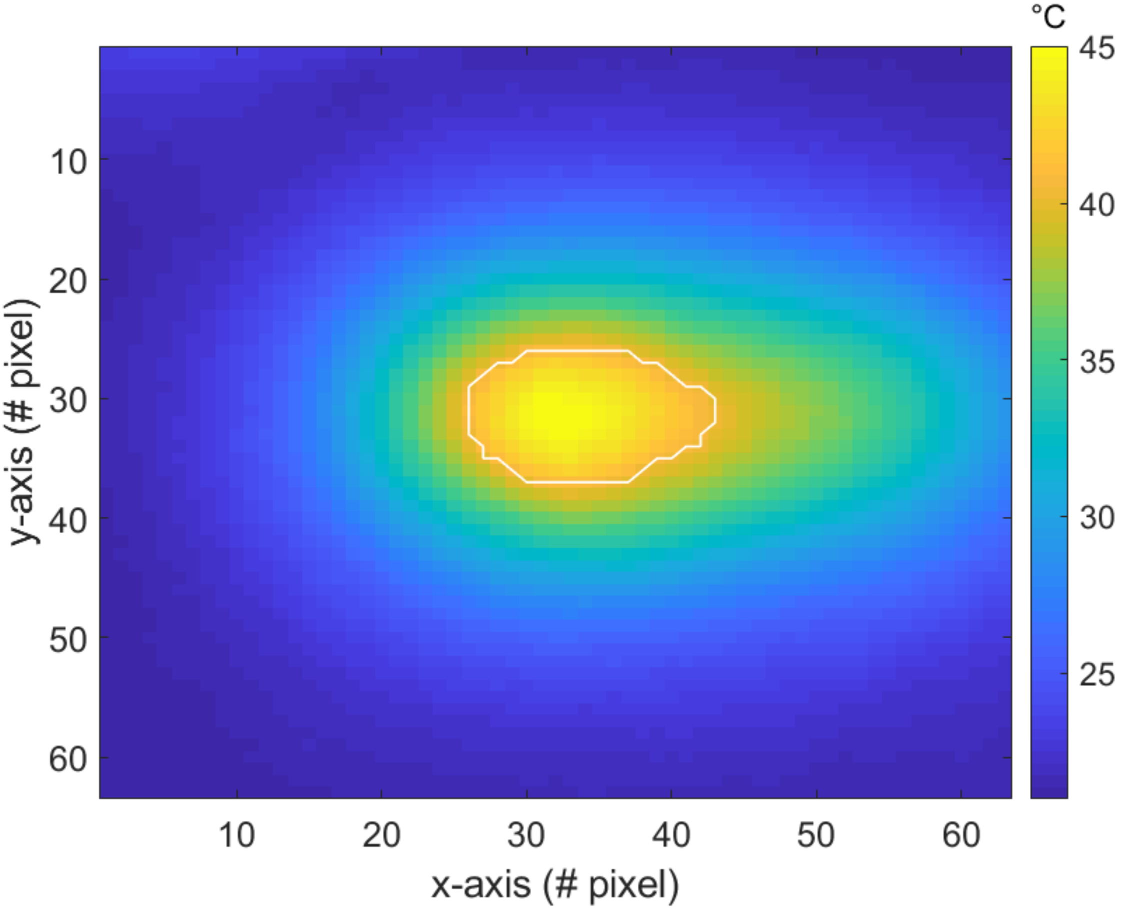

Figure 9.19: Test 2. Image from the matrix of the thermographic camera.

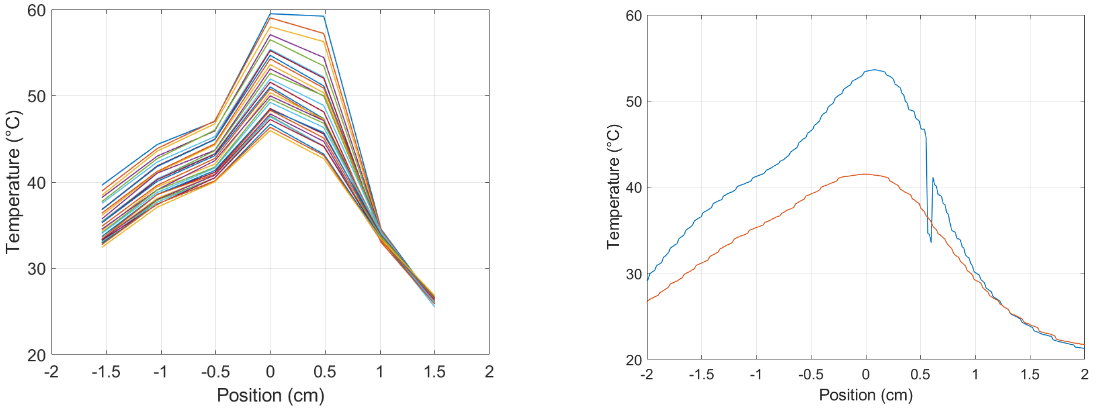

(a) Array A - minutes 12:21-12:51 **(b)** Distributed sensor - minutes 12:28; 12:56

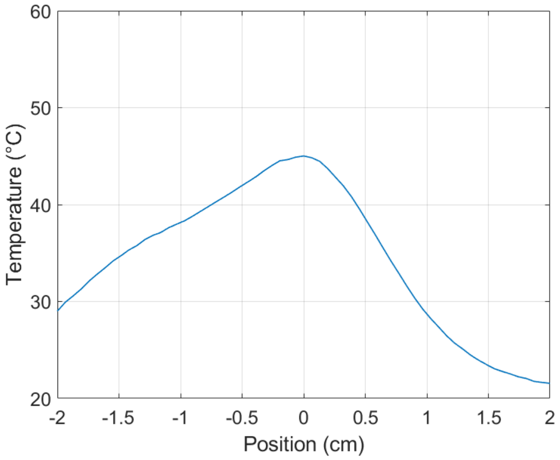

(c) Thermal camera - minute 12:51

Figure 9.20: Comparison of the temperature measured along the parallel axis to the delivery fibre at the end of test 2.

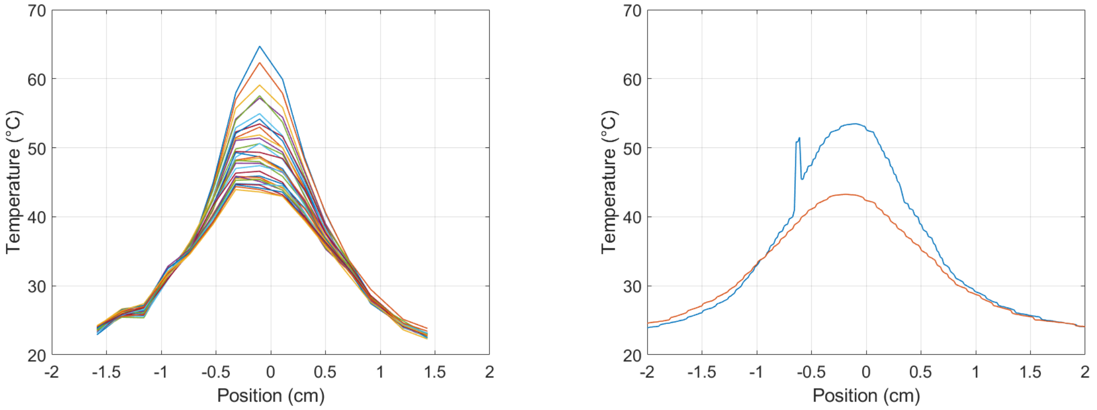

(a) Array B - minutes 12:21-12:51 **(b)** Distributed sensor - minutes 12:28; 12:56

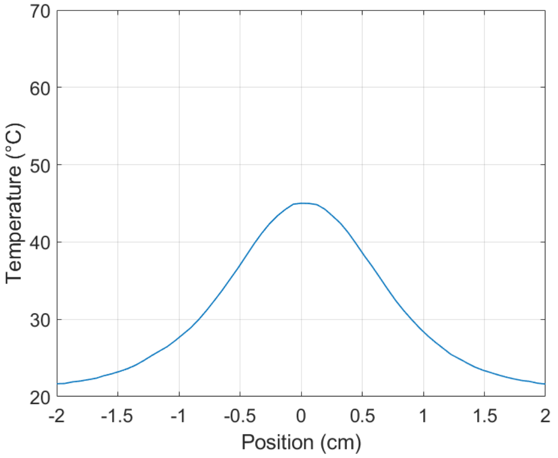

(c) Thermal camera - minute 12:51

Figure 9.21: Comparison of the temperature measured along the orthogonal axis to the delivery fibre at the end of test 2.
The distance between the optical fibre sensors is 1 mm.

Test 3

Time: minute 1:17

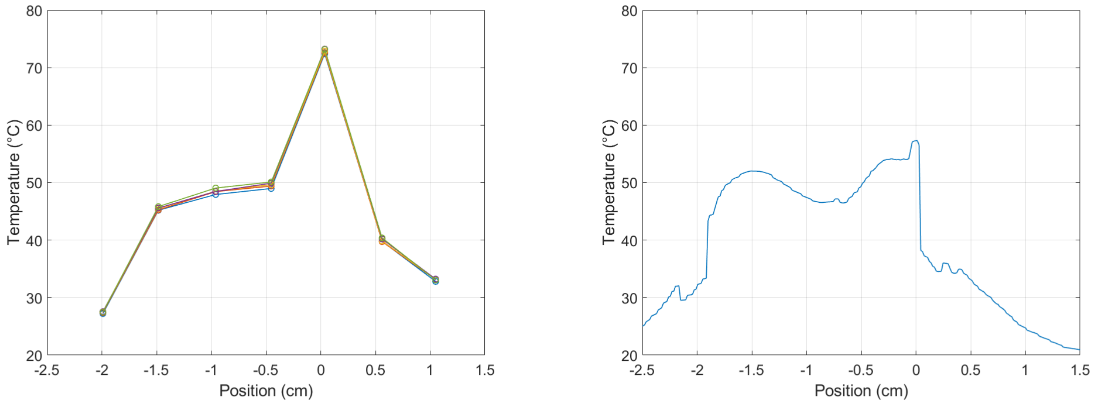

(a) Array A **(b)** Distributed sensor

Figure 9.22: Test 3 - minute 1:17. Temperature of the quasi-distributed and fully distributed sensors parallel to the delivery fibre.
The distance between the sensors is 1 mm.

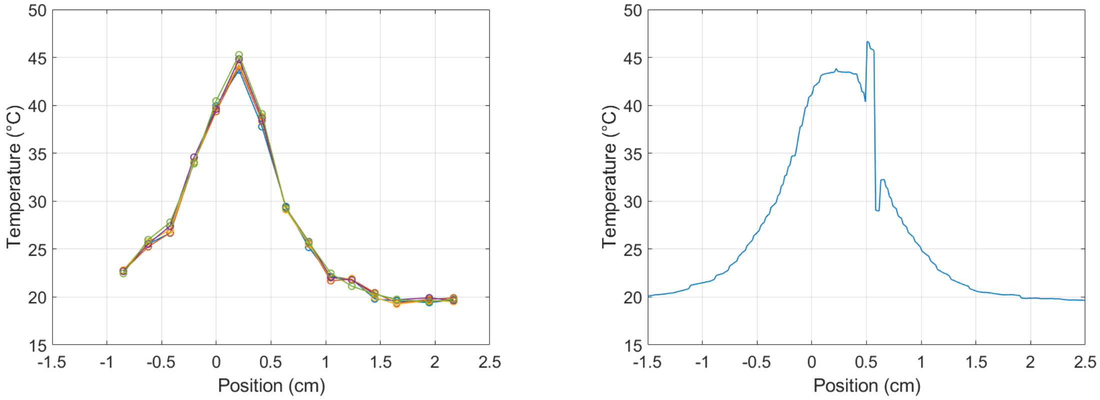

(a) Array B **(b)** Distributed sensor

Figure 9.23: Test 3 - minute 1:17. Temperature of the quasi-distributed and fully distributed sensors perpendicular to the delivery fibre.

Time: minute 1:45

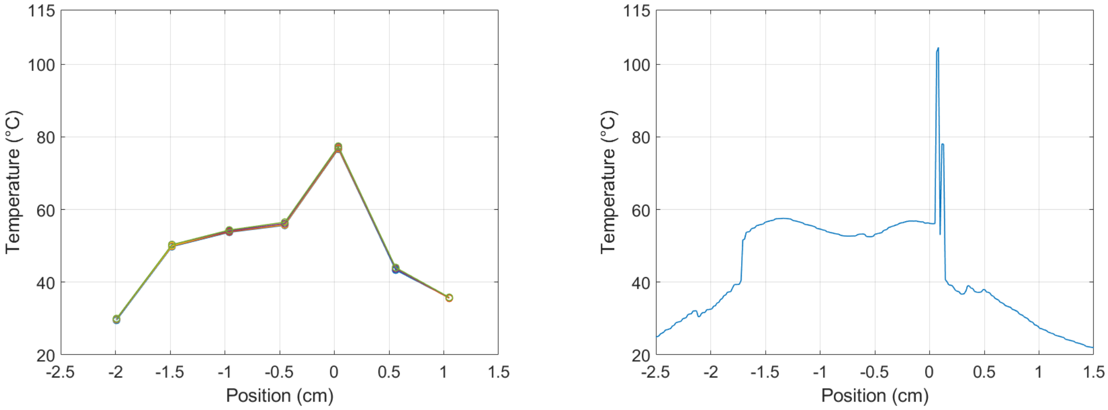

(a) Array A **(b)** Distributed sensor

Figure 9.24: Test 3 - minute 1:47. Temperature of the quasi-distributed and fully distributed sensors parallel to the delivery fibre.
The distance between the sensors is 1 mm.

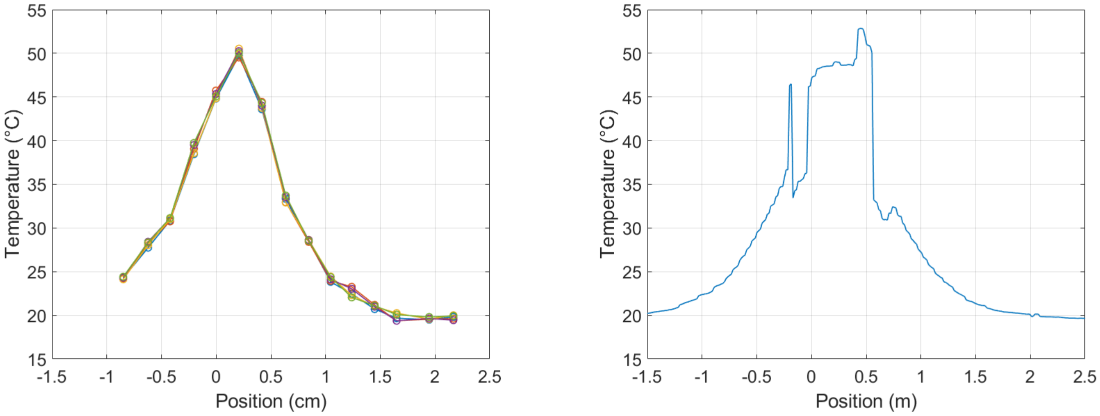

(a) Array B **(b)** Distributed sensor

Figure 9.25: Test 3 - minute 1:47. Temperature of the quasi-distributed and fully distributed sensors perpendicular to the delivery fibre.

Time: minute 2:07

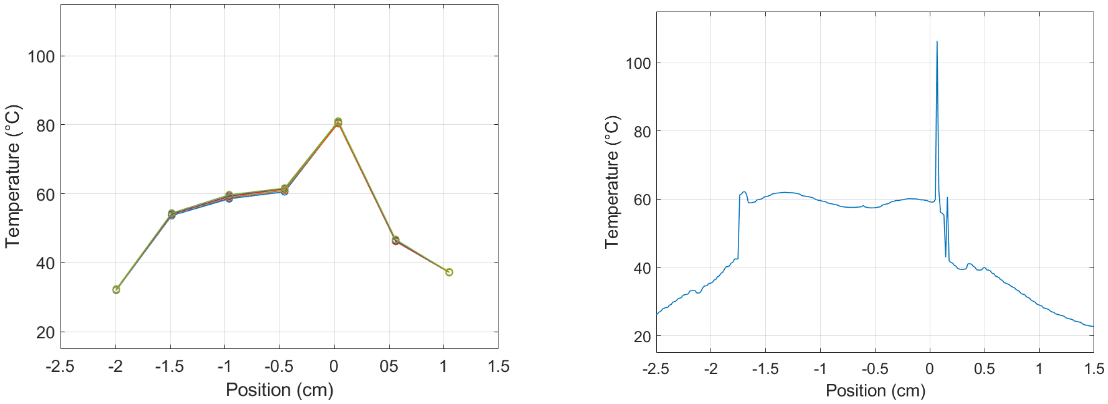

(a) Array A **(b)** Distributed sensor

Figure 9.26: Test 3 - minute 2:07. Temperature of the quasi-distributed and fully distributed sensors parallel to the delivery fibre.
The distance between the sensors is 1 mm.

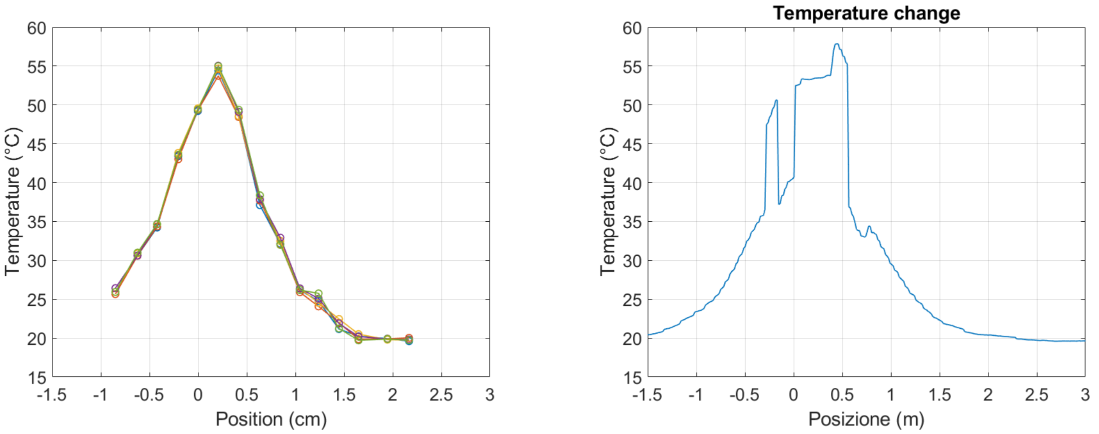

(a) Array A **(b)** Distributed sensor

Figure 9.27: Test 3 - minute 2:07. Temperature of the quasi-distributed and fully distributed sensors perpendicular to the delivery fibre.

Time: minute 2:42

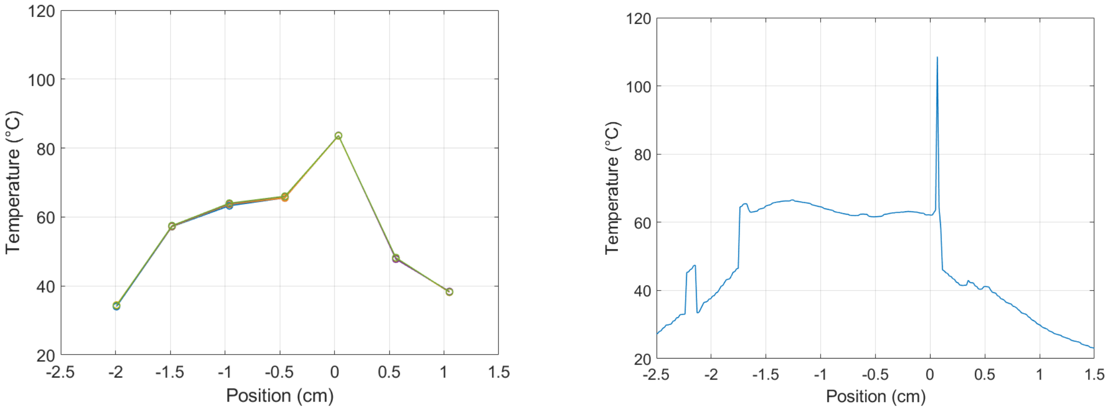

(a) Array A **(b)** Distributed sensor

Figure 9.28: Test 3 - minute 2:42. Temperature of the quasi-distributed and fully distributed sensors parallel to the delivery fibre.
The distance between the sensors is 1 mm.

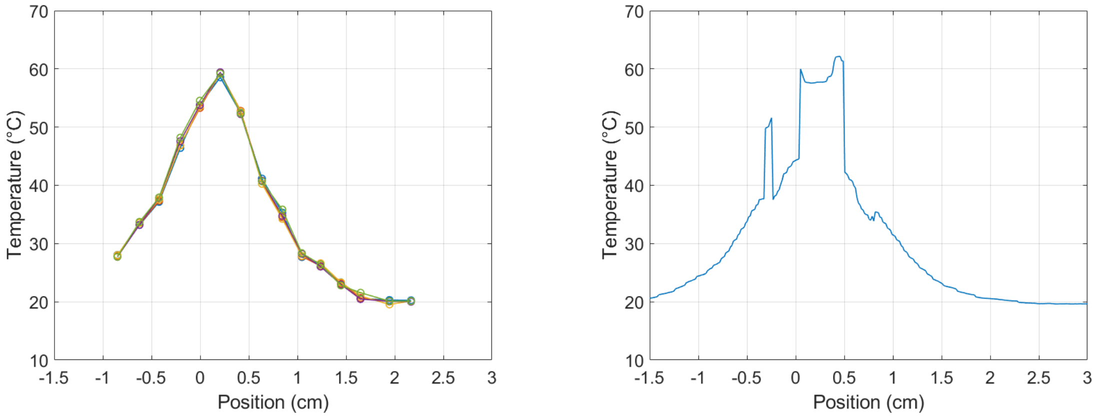

(a) Array B **(b)** Distributed sensor

Figure 9.29: Test 3 - minute 2:42. Temperature of the quasi-distributed and fully distributed sensors perpendicular to the delivery fibre.

Time: minute 3:10

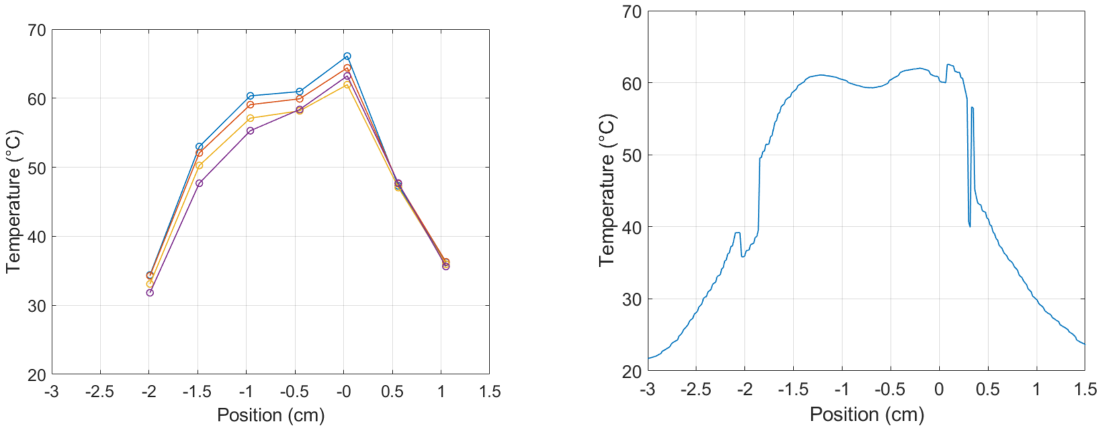

(a) Array A **(b)** Distributed sensor

Figure 9.30: Test 3 - minute 3:10. Temperature of the quasi-distributed and fully distributed sensors parallel to the delivery fibre.
The distance between the sensors is 1 mm.

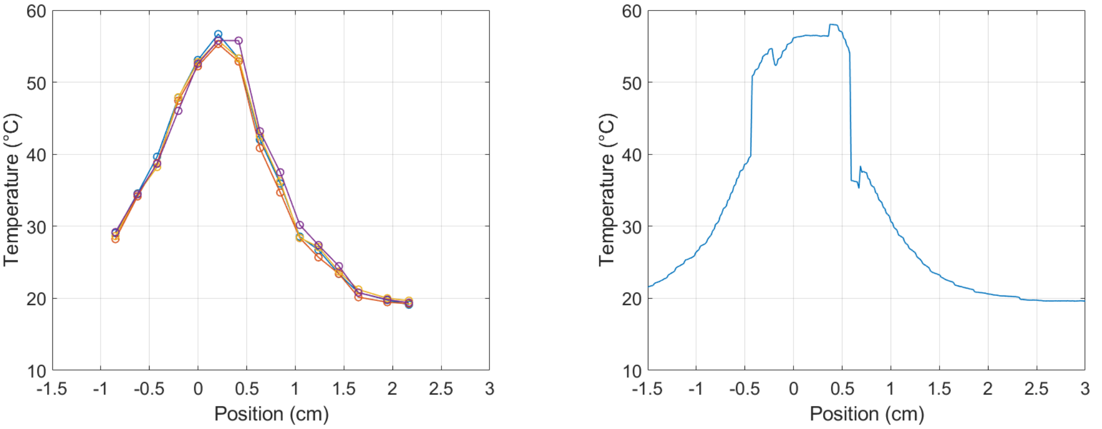

(a) Array B **(b)** Distributed sensor

Figure 9.31: Test 3 - minute 3:10. Temperature of the quasi-distributed and fully distributed sensors perpendicular to the delivery fibre.

End of the test

The thermal camera acquired the matrix at minute 3:21 after the beginning of the test. The FBG acquisitions are in the 20-seconds-time interval (from minute 3:01 to minute 3:21) and the distributed sensor at minutes 3:03, 3:22 and 4:00.

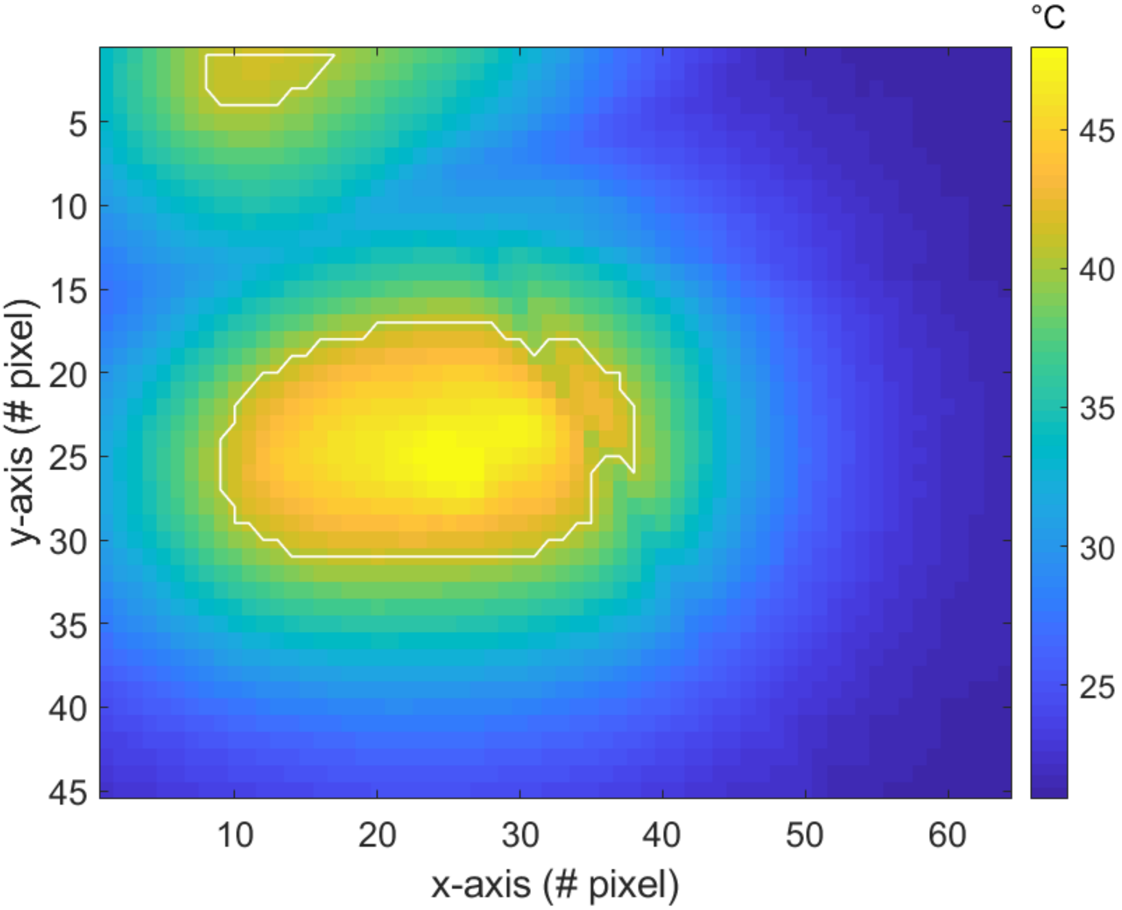

Figure 9.32: Test 3. Image from the matrix of the thermographic camera.

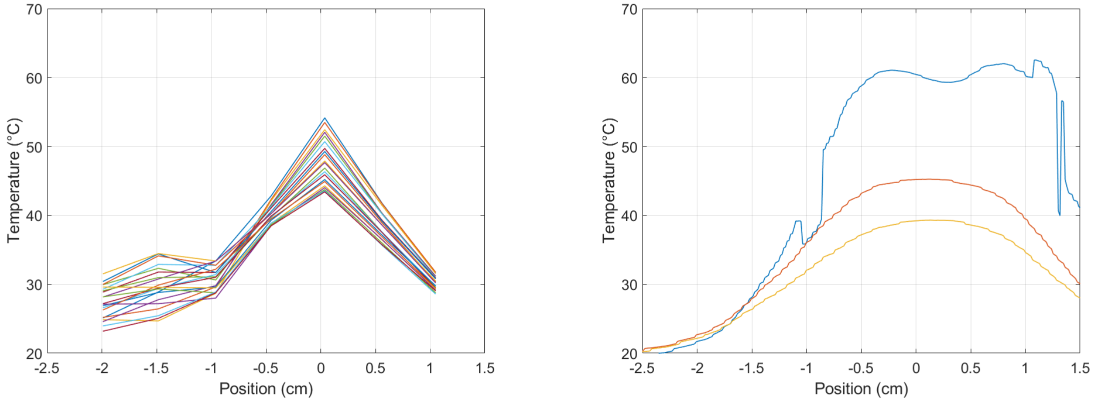

(a) Array A - minutes 3:01-3:21 **(b)** Distributed sensor - minutes 3:03; 3:22; 4:00

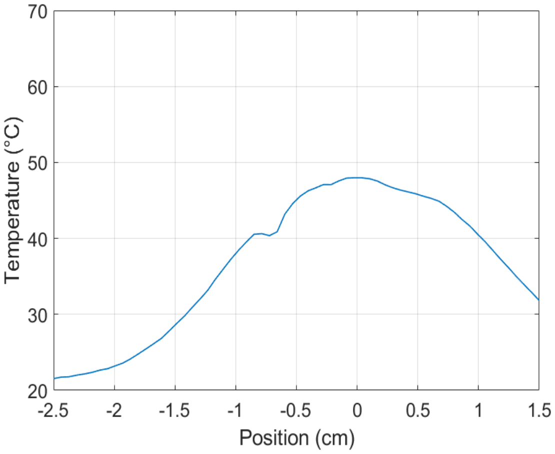

(c) Thermal camera - minute 3:21

Figure 9.33: Comparison of the temperature measured along the parallel axis to the delivery fibre at the end of test 3.
The distance between the sensors is 1 mm.

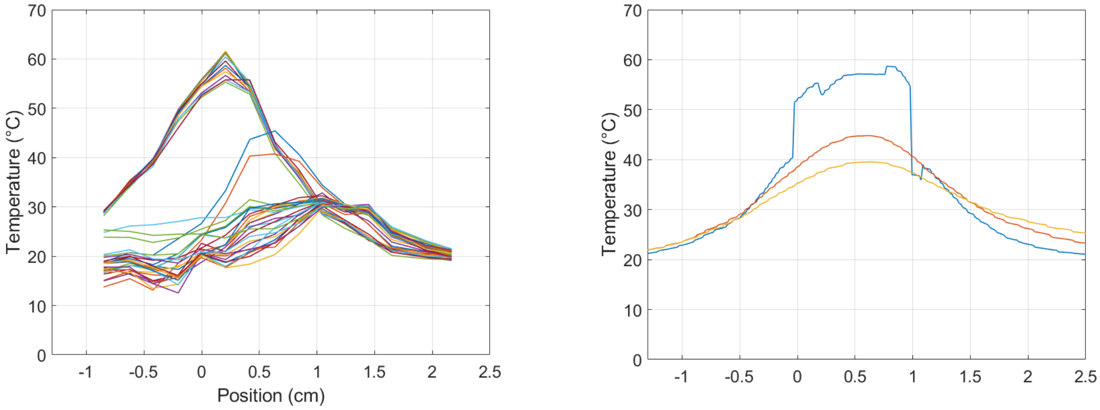

(a) Array B - minutes 3:01-3:21 **(b)** Distributed sensor - minutes 3:03; 3:22; 4:00

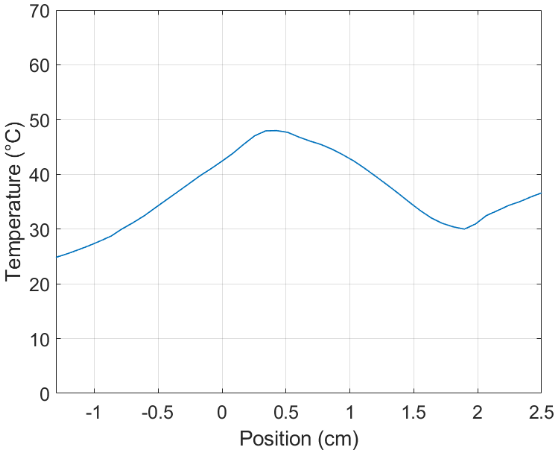

(c) Thermal camera - minute 3:21

Figure 9.34: Comparison of the temperature measured along the orthogonal axis to the delivery fibre at the end of test 3.

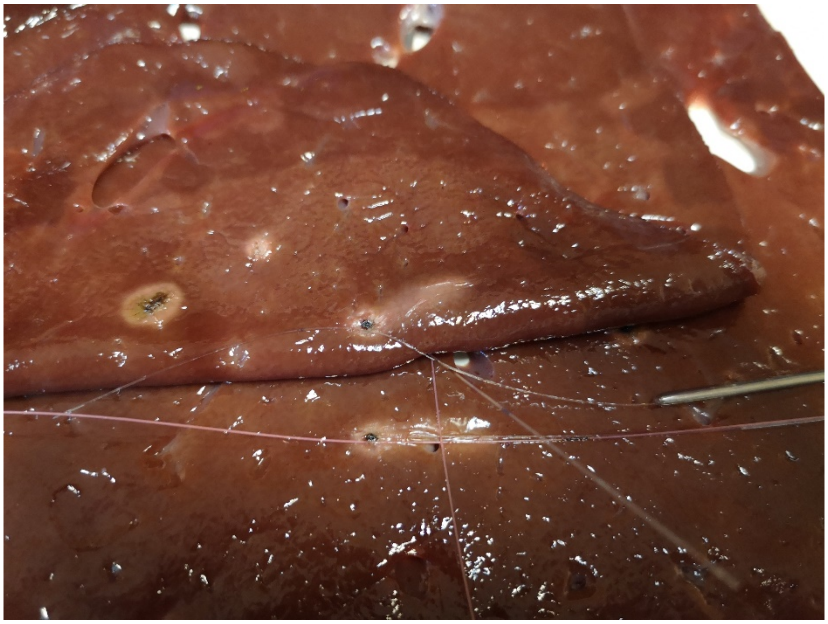

Figure 9.35: Slices at the end of test 3. The slices are close to avoid the fibre damage.

9.3 Observations

The executed tests allow the comparison of the sensing capabilities of the investigated optical fibres sensors in non-uniform thermal conditions and their comparison with the reference temperature sensor (the thermal camera).

The first test is the only one performed with the point-like source and it shows high temperature level reached at the half of the duration of the irradiation. This fact is in agreement with the simulated values.

The ablated area, as seen in Figs. 9.8 and 9.7, is elliptical shaped, sized 9 mm x 7 mm with the major axis parallel to the emitting fibre.

The responses of the parallel sensors are in agreement both from the point of view of the values and from the point of view of the shape. The sharp variation in temperature of the fully distributed sensor is due to the overlap of the optical fibre.

The orthogonal sensors have so different responses because of the strong thermal attenuation of the tissue which causes a steep decrease of the temperature in few millimetres of tissue, confirmed by analytical and experimental results [40, 41].

In the continuous-wave laser emission mode the heat propagates only in a small area in front of the source, as described in Chapter 3.

At the end of the test the measured temperature of the three sensors are in agreement.

The temperature of the tissue decreased rapidly due to the air convection, the temperature measured is lowered confirming that previously the temperature was higher than 60 °C, achieving the cytotoxic desired effect.

The second test has been performed with the damaged delivery fibre which emits laser radi-

ation laterally from the last two centimetres of its length.
The parallel sensors are in contact and, in fact, the profiles and the values are consistent along the entire test. The temperature obtained show that 2 W are not sufficient to ablate the tissue.
The lateral irradiation is visible from the parallel sensor measurements, which have a flat shape in the 2-cm-portion of the delivery fibre. The profile of the temperature corresponding to the damaged portion of the emitting fibre is not perfectly flat due to irregularities in the damaging of the cladding, thus the power is not perfectly distributed along the 2 centimetres. The peak of temperature is due to the emission from the tip (34% of the total power). The orthogonal temperature profile is symmetrical as expected, the temperature gap is due to the distance between the sensors.
The final comparisons are a further confirm of the reliability of the optical fibre sensors, both quasi-distributed and distributed.
The third test with the pulsed-wave laser emission mode increase the tissue temperature to efficient cytotoxic levels. The distance between the sensors placed parallel to the delivery fibre is 1 mm and causes the slight difference in the measured temperatures.
In both parallel and orthogonal fully distributed measurements there are some spurious peaks and valleys, they are due to the overlap of the sensing fibre.

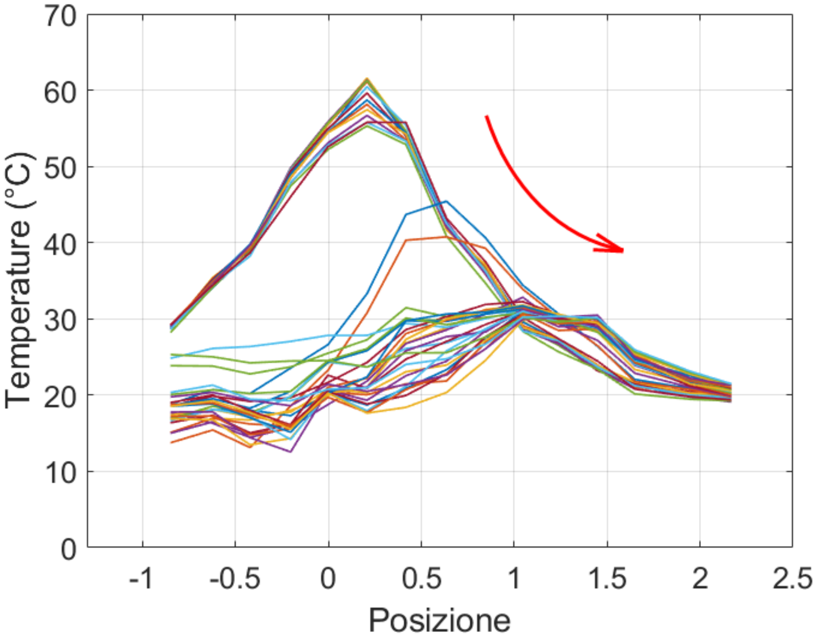

Figure 9.36: Temperature profile at the end of test 3 measured with the array B. The peak moves to different position due to the strain effect of the bending of the slices during their separation.

The final comparison with the thermal camera confirms the previous considerations of

robustness of the temperature acquisition on the optical fibre sensors, with discrepancies in the measured temperature of ±2 °C.
In the orthogonal comparison the FBG-array measures a translation of measurements due to the bending of the fibre causing strain, in fact, the ablation causes the tissue to reach the carbonization, holding the fibre on the upper slice.
To avoid the sensor break, the slices are kept close and thus, the thermal camera detects a close increase of temperature, seen in the portion in the red circle in Fig. 9.37.

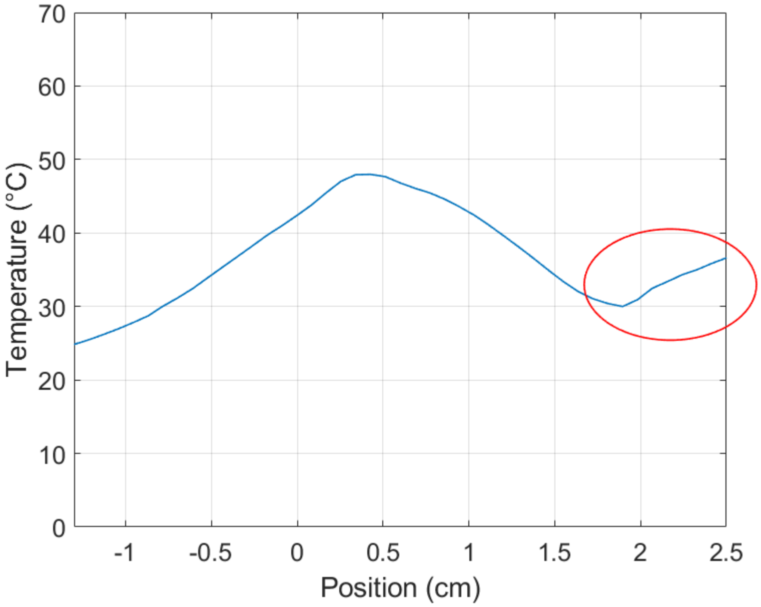

Figure 9.37: Close increase of temperature.

The comparison between tests can be performed only between the second and the third because they are performed with the same delivery fibre.
The second test reaches lower temperature levels because of the low power (2 W) delivered to the tissue and generates a lighter area visible to the eye (sized 5 mm × 5 mm), this is due to the fact that the laser irradiates laterally. The low power level from the tip (36% of the total power) does not induce the tissue carbonization. The pulsed-wave laser of the third test reaches higher temperature because the power is higher (7 W) and the tissue cannot diffuse completely the heat in the short time in which the laser is turned off. The ablated area obtained in this test is the wider, as shown in the images of the thermal camera.
The absolute higher temperature is reached by the first test, as expected, because the whole power is delivered from the tip of the fibre causing also a reduced ablated area.
Two more tests have been performed, with the laser emitting at a higher wavelength (λ= 1470 nm), but cannot be reported and commented from the point of view of this work because the irradiation caused the optical fibres to break. The temperature acquired by the fully dis-

tributed sensor before of the breakage show that the cytotoxic effect has been achieved (in the continuous-wave emission).
Summarizing the reported tests, the higher temperature is reached with the un-damaged tip because the power is emitted in the same point; the wider irradiated area is obviously reached with the damaged delivery fibre and the third test reaches cytotoxic effect in a wider area thanks to its combination of high power and distributed irradiation.

In conclusion, it is possible to state that the optical fibre temperature sensors are quite reliable in the measurements and further studies can be conducted to improve the precision and maybe to distinguish the strain and the temperature effects in order to correct part of the errors affecting the measurements.

Chapter 10

Conclusions

The Master's thesis project relied on an aspect of the laser ablation of hepatic cancer: the temperature monitoring, fundamental during the procedure to allow the surgeon to adjust the parameters in order to reach the cytotoxic effect without carbonization of the tissue.
The optical fibre sensors considered and compared are quasi-distributed and fully distributed optical fibres.
The quasi-distributed temperature sensors are based on the fibre Bragg gratings.
The FBGs are in-fibre components realized with a periodical change of the refractive index inside the fibre core. The periodical structure has a notch filter response, when interacts with the laser light causes the reflection of a specific wavelength, called Bragg wavelength. The Bragg wavelength varies depending on the temperature and the strain applied to the fibre.
The FBGs investigated for this project are superstructure FBG (7 and 15-FBGs-arrays) inscribed in the core of telecom-grade optical fibres which are double cladding optical fibres. Due to their dimension and to the fact that they are realized in the core with a millimetric space.
The FBGs are interrogated with the optical interrogator Micron Optics HYPERION si155, by Luna Technologies®.
Its source is a tuneable laser going in input to an optical circulator and to the FBG-array. The reflected light at the Bragg wavelength of each FBG, through the optical circulator, reaches a photodiode. The detected optical power is at the end converted into analogic voltage.
The instrument is connected to the ethernet connection in order to send data to the relative software, ENLIGHT Sensing Analysis Software.
Before the experimental activities, the FBG-array optical fibres have been characterized in the climatic chamber: their Bragg wavelengths shift with the change of temperature in a linear fashion. Thanks to the use of a reference temperature sensor (a J-type thermocouple) and to a Matlab® script, the parameters λ_0 and k describing the thermal behaviour of each FBG have been obtained.
The distributed temperature sensor is a standard single-mode optical fibre SMF-28.
The instrument measuring the temperature of the single-mode fibre is Luna OBR4600, by Luna Technologies®.

It is a Coherent Optical Frequency Domain Reflectometer (C-OFDR). Its optical source is a tuneable laser which sweeps the frequency in time with linearity. The generated signal is split in two paths by a coupler: the first is the reference signal of the interferometer and the second is guided to the optical fiber to investigate. The presence of a mirror at the end of the reference arm and Rayleigh backscattering phenomenon in the measurement path causes two reflection signals that are recombined in a coupler with interference due to the different length of the paths caused by the distributed backscattering events in the investigated fiber. The interferent signal is guided to the receiver and with a Fourier Transform, the beat frequencies are extracted, shown as peaks, and using a linearly swept optical frequency they are reconducted to the backscattering event as a function of the length of the fibre.

Both temperature and strain cause spectral shift of the signal detected by the OBR instrument with respect to the acquired reference signal with a linear proportionality.

In the climatic chamber,the distributed sensor has been tested, leading to use it without the protective polymeric jacket. In fact, the polymeric expansion and contraction induce strain causing an error in the temperature measurements. Moreover, has been found that the strong reflection due to the end of the fibre cause the sensor to be non-usable in the last 10-15 centrimetres.

The comparison of the sensing capabilities of the sensors have been performed in uniform temperature conditions, with an *ad hoc* setup realized with a metallic cantilever used to generate a linear thermal gradient.

The central portion of the aluminium bar where the gradient is generated is 4-cm long, has a groove along its length to host the fibres (the distributed sensor protrudes of 29.7 cm from the area of linear thermal gradient) and has three T-type thermocouples as reference temperature sensors (the two external are sufficient to interpolate a linear profile).

The gradient is obtained by heating one side with a 4Ω resistor dissipating the power supplied by a power generator according to the Joule effect; whereas the other side is fixed with a transverse bar to a solid metal breadboard in order to exploit its high thermal inertia. To reduce the temperature changes due to air convection, the studied tract is fixed and covered by polystyrene blocks.

The preliminary test has been performed in the climatic chamber (no thermal gradient has been generated) with the fully distributed and the 15-FBGs-array optical fibre protected by a thin glass capillary, reporting satisfying from the point of view of the profile, but with non-negligible errors in the returning to the initial temperature level.

Two tests have been performed with the generation of the linear thermal gradient: the first without the capillary. Both the tests have been executed covering the sensible portion with thermal grease.

The results are better without the capillary because possible friction among the fibres and possible longitudinal forces due to the contact with the glass capillary, cause internal strain detected as thermal effect by the sensors, obtaining high error in the measurements if compared to the reference sensors.

The final trial has been in non-uniform thermal conditions: the laser ablation procedure has been performed on an *ex-vivo* bovine liver. The reference sensor has been a thermographic camera mounted above the setup.

A 915-nm-laser has been used to irradiate the tissue, the delivery fibres used are multi-mode fibres with polymeric cladding and coating.

The first test was performed with low-power laser in continuous emission mode and the delivery fibre emitted from the tip.

The second and third tests used the other multi-mode delivery fibre, treated with HeNe laser to obtain the cladding damage for the last 2-cm length, to make the fibre emit laterally.

The sensors have been placed on the liver slice parallel and orthogonal to the delivery and then covered with another slice. The distributed sensor is single but it is quite long to overlap in order sense both in parallel and orthogonal directions.

The results showed the highest temperature reached in the first test, because the power is delivered totally in the point close to the fibre tip.

The third test obtained the wider ablated area event though the temperature were not the highest but sufficient to cause cytotoxic effects.

From the results of the second and third test show a quasi-flattened profile due to the lateral emission of the 2-cm length damaged portion of the delivery fibre.

The temperatures are in agreement between the fibre sensors, the distance has played a crucial role because the temperature values decrease steeply, in few millimetres from the source the temperature change is non-negligible.

The comparisons with the reference sensor (the thermal camera) have been performed only at the end of each test because the second slice covering has a double effect: prevents from the air convection but reduces the infra-red radiation detected bu the camera. For this reason, the measurements of the optical fibre sensors at the end of the duration of irradiation are compared with the thermal camera measurement, acquired immediately, after the separation of the slices. The sensor acquisition after the separation of the slices are not reiable because the moving and the touching of the sensors induce strain perturbation not immediately recovered.

The compared temperature with the reference have demonstrated consistency both in value and in profile.

The results of the tests performed for this project showed the qualities of the optical fibre sensors to monitor the temperature during the laser ablation procedure: low effect of the strain, reduced dimension, high precision and accuracy of the measurements.

The disadvantages are the fragility of the fibre itself and the fact that the fully distributed sensor cannot measure the temperature in the extremity.

In conclusion, the qualities of the investigated sensors can lay the foundation for further studies to solve some limits and to improve the sensing capabilities of the optical fibre temperature sensors, in order to increase the employment of the laser ablation and the number of patient recovered from the tumour.

Part III

Appendices

Appendix A

Matlab code - FBG data processing

```matlab
%% CLIMATIC CHAMBER DATA %%

%Opening file .txt from Micron Optics si155

clear all
close all
clc

%Data acquisition in table
file_id = fullfile(pwd, 'Peaks.20191212153311.txt');
%fullfile returns the complete file name from the parts given
%'pwd' is to use the path of the current folder
%alternatively, it is possible to write the extended path of the file
%e.g. f = fullfile('c:\','myfiles','matlab','myfile1.m');

t = readtable(file_id, 'Delimiter', '\t');
%readtable fuction creates a table from a file
%all the formats are included in the same table (string, double,...)
%the delimiter \t used allows to distinguish the numeric variables
%contained in the file (in which the formated separator is tab).
%Using the 'Delimiter', '\t' parameters allows to convert also irregular
%files in dimension

time=t(:,1); %time contains the date and time data
mat_time=table2array(time);
mat_time=split(mat_time);
```

```
time_ar=mat_time(:,2); %time_ar is a string array containing the time information

datn=datenum(time_ar,'HH:MM:SS');


channels=t(:,(2:5)); %channels contains the data of the number FBGs detected in the four channels
mat_ch=table2array(channels);

info=t(:,(6:end)); %info contains the data acquired by each channel of the instrument
mat_info=table2array(info);

%-table2array converts a table to an array BUT its content must be homogeneous in type
%-split divides a string at whitespace
%-datenum function converts date and time to serial date number


%create a matrix for each channel, containing the corresponding data
ro=length(mat_ch); %number of rows
col_1=max(mat_ch(:,1)); %number of columns (FBGs detected) in the first channel
col_2=max(mat_ch(:,2)); %number of columns (FBGs detected) in the second channel
col_3=max(mat_ch(:,3)); %number of columns (FBGs detected) in the third channel
col_4=max(mat_ch(:,4)); %number of columns (FBGs detected) in the fourth channel


%CHANNEL 1
ch1=zeros(ro, col_1);
  for a=1:ro %moving on rows
     for b=1:col_1 %moving on columns
         ch1(a,b)=mat_info(a,b);
     end
  end

%CHANNEL 2
ch2=zeros(ro, col_2);
```

```
  for a=1:ro %moving on rows
    for b=1:col_2 %moving on columns
        ch2(a,b)=mat_info(a,(b+col_1));
    end
  end

%CHANNEL 3
ch3=zeros(ro, col_3);
   for a=1:ro %moving on rows
      for b=1:col_3 %moving on columns
          ch3(a,b)=mat_info(a,(b+col_1+col_2));
      end
   end

%CHANNEL 4
ch4=zeros(ro, col_4);
   for a=1:ro %moving on rows
      for b=1:col_4 %moving on columns
          ch4(a,b)=mat_info(a,(b+col_1+col_2+col_3));
      end
   end

datn=datn-datn(1);

%PLOTTING FIGURES OF EACH FBG DETECTED
j=0;
if col_1~=0
    for i=1:col_1
        j=j+1;
        figure(j)
        plot(datn, ch1(:,i),'LineWidth',1);
        hold on
        datetick('x','HH:MM:SS', 'keepticks');
        grid on
        ax = gca; % current axes
        ax.FontSize = 15;
        xlabel('Absolute time')
        ylabel('Wavelength (nm)')
        title(['Channel 1 - FBG num ', num2str(i)], 'fontsize', 18)
    end
end

```

```
if col_2~=0
    for i=1:col_2
        j=j+1;
        figure(j)
        plot(datn, ch2(:,i),'LineWidth',1);
        hold on
        datetick('x','HH:MM:SS', 'keepticks');
        grid on
        ax = gca; % current axes
        ax.FontSize = 15;
        xlabel('Absolute time')
        ylabel('Wavelength (nm)')
        title(['Channel 2 - FBG num ', num2str(i)], 'fontsize', 18)
    end
end

if col_3~=0
    for i=1:col_3
        j=j+1;
        figure(j)
        plot(datn, ch3(:,i),'LineWidth',1);
        hold on
        datetick('x','HH:MM:SS', 'keepticks');
        grid on
        ax = gca; % current axes
        ax.FontSize = 15;
        xlabel('Absolute time')
        ylabel('Wavelength (nm)')
        title(['Channel 3 - FBG num ', num2str(i)], 'fontsize', 18)
    end
end

if col_4~=0
    for i=1:col_4
        j=j+1;
        figure(j)
        plot(datn, ch4(:,i),'LineWidth',1);
        hold on
        datetick('x','HH:MM:SS', 'keepticks');
        grid on
        ax = gca; % current axes
```

```
        ax.FontSize = 15;
        xlabel('Absolute time')
        ylabel('Wavelength (nm)')
        title(['Channel 4 - FBG num ', num2str(i)], 'fontsize',
            18)
    end
end
```

Appendix B

LabVIEW$^{\mathrm{TM}}$ remote control program

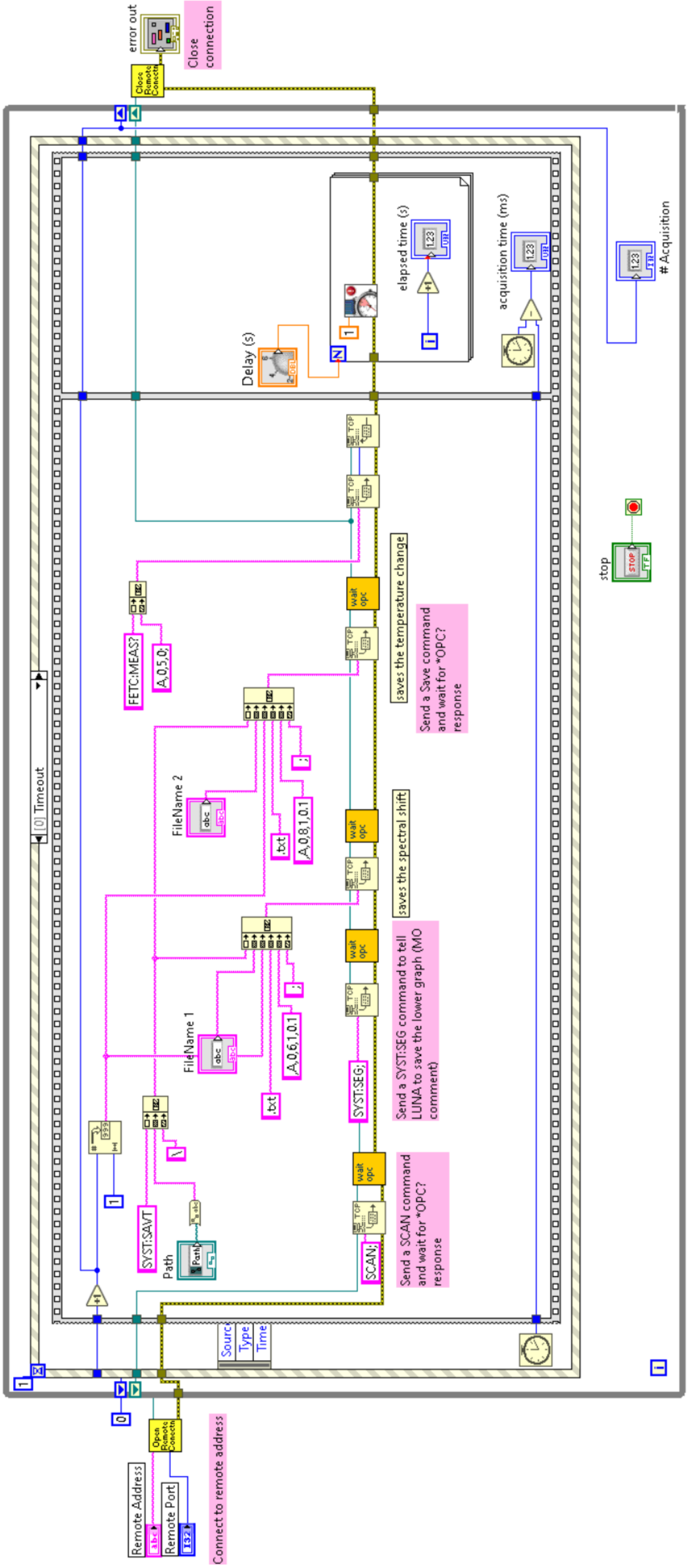

Figure B.1: LabVIEW block diagram of the OBR remote control program.

List of Figures

List of Tables

Bibliography

[1] Freddie Bray et al. "Global cancer statistics 2018: GLOBOCAN estimates of incidence and mortality worldwide for 36 cancers in 185 countries". In: *CA: A Cancer Journal for Clinicians* 68.6 (2018), pp. 394–424. DOI: `10.3322/caac.21492`. URL: `https://acsjournals.onlinelibrary.wiley.com/doi/abs/10.3322/caac.21492`.

[2] D. Hashim et al. "The global decrease in cancer mortality: trends and disparities". In: *Annals of Oncology* 27.5 (2016), pp. 926–933. DOI: `https://doi.org/10.1093/annonc/mdw027`. URL: `http://www.sciencedirect.com/science/article/pii/S0923753419374113`.

[3] Riccardo Gassino. "Development of a fiber optic probe for tumor laser ablation with integrated temperature measurement capabilities". PhD Thesis. Politecnico di Torino, 2019.

[4] Chris J. Diederich. "Thermal ablation and high-temperature thermal therapy: Overview of technology and clinical implementation". In: *International Journal of Hyperthermia* 21.8 (2005), pp. 745–753. DOI: `10.1080/02656730500271692`. URL: `https://doi.org/10.1080/02656730500271692`.

[5] C. Brace. "Thermal Tumor Ablation in Clinical Use". In: *IEEE Pulse* 2.5 (Sept. 2011), pp. 28–38. ISSN: 2154-2317. DOI: `10.1109/MPUL.2011.942603`.

[6] Michael Beland, Peter R. Mueller, and Debra A. Gervais. "Thermal Ablation in Interventional Oncology". In: *Seminars in Roentgenology* 42.3 (2007). Interventions in Oncology, pp. 175–190. ISSN: 0037-198X. DOI: `https://doi.org/10.1053/j.ro.2007.04.005`. URL: `http://www.sciencedirect.com/science/article/pii/S0037198X07000235`.

[7] Muneeb Ahmed et al. "Principles of and Advances in Percutaneous Ablation". In: *Radiology* 258.2 (2011). PMID: 21273519, pp. 351–369. DOI: `10.1148/radiol.10081634`. eprint: `https://doi.org/10.1148/radiol.10081634`. URL: `https://doi.org/10.1148/radiol.10081634`.

[8] Riadh W. Y. Habash et al. "Thermal Therapy, Part 1: An Introduction to Thermal Therapy". In: *Critical Reviews™ in Biomedical Engineering* 34.6 (2006), pp. 459–489. ISSN: 0278-940X.

[9] Nick Berg et al. "Energetic soft-tissue treatment technologies: An overview of procedural fundamentals and safety factors". In: *Surgical endoscopy* 27 (Apr. 2013). DOI: `10.1007/s00464-013-2923-6`.

[10] S. Nahum Goldberg et al. "Tissue ablation with radiofrequency: Effect of probe size, gauge, duration, and temperature on lesion volume". In: *Academic Radiology* 2.5 (1995), pp. 399–404. ISSN: 1076-6332. DOI: `https://doi.org/10.1016/S1076-6332(05)80342-3`. URL: `http://www.sciencedirect.com/science/article/pii/S1076633205803423`.

[11] Lorenzo Torrisi et al. "Applicazioni di fasci laser al settore biomedico". In: July 2011.

[12] M. Cutroneo, Lorenzo Torrisi, and Cristina Scolaro. "Laser applications in bio-medical field". In: 2010 (July 2012).

[13] Paola Saccomandi et al. "Laser ablation of the biliary tree: in vivo proof of concept as potential treatment of unresectable cholangiocarcinoma". In: *International Journal of Hyperthermia* 34.8 (2018). PMID: 29322853, pp. 1372–1380. DOI: `10.1080/02656736.2018.1427287`. URL: `https://doi.org/10.1080/02656736.2018.1427287`.

[14] Alexander B. Akimov et al. "Nd:YAG interstitial laser thermotherapy in the treatment of breast cancer". In: *Lasers in Surgery and Medicine* 22.5 (1998), pp. 257–267. DOI: `10.1002/(SICI)1096-9101(1998)22:5<257::AID-LSM1>3.0.CO;2-O`.

[15] URL: `http://centromedicalaser.weebly.com/chirurgia-cutanea-campania-basilicata-puglia-calabria-sicilia-napoli-salerno-potenza-matera-cosenza-taranto-catanzaro-reggio-calabria.html`.

[16] Svelto Orazio. *Principles of Lasers*. 5th ed. Springer.

[17] URL: `https://engineeringtutorial.com/laser-diode-working-principle/`.

[18] Heidi Brunborg et al. "Light propagation in pulp and paper research". In: 2003.

[19] URL: `https://www.doitpoms.ac.uk/tlplib/raman/raman_scattering.php`.

[20] D. K. Gifford et al. "Distributed fiber-optic temperature sensing using Rayleigh backscatter". In: *2005 31st European Conference on Optical Communication, ECOC 2005*. Vol. 3. Sept. 2005, 511–512 vol.3. DOI: `10.1049/cp:20050584`.

[21] Kalli Andreas Othonos; Kyriacos. *Fiber Bragg Gratings*. Artech House Boston - London, 1999.

[22] URL: `http://www.infibratechnologies.com/technologies/fiber-bragg-gratings.html`.

[23] URL: `https://fbgs.com/technology/fbg-principle/`.

[24] URL: `https://en.wikipedia.org/wiki/Fiber_Bragg_grating`.

[25] T. Erdogan. "Fiber grating spectra". In: *Journal of Lightwave Technology* 15.8 (Aug. 1997), pp. 1277–1294. ISSN: 1558-2213. DOI: `10.1109/50.618322`.

[26] Mark Froggatt; Ryan J. Seeley; Dawn K. Gifford. *High resolution interferometric optical frequency domain reflectometry (OFDR) beyond the laser coherence length*. US 7515276B2. Google Patents, Apr. 2009. URL: `https://patents.google.com/patent/US7515276B2/en?oq=US+7%5C%2c515%5C%2c276+B2`.

[27] Emiliano Schena et al. "Fiber Optic Sensors for Temperature Monitoring during Thermal Treatments: An Overview". In: *Sensors* 16.7 (2016). DOI: `10.3390/s16071144`. URL: `https://www.mdpi.com/1424-8220/16/7/1144`.

[28] Jijo et al. Paul. "Dual energy computed tomography thermometry during hepatic microwave ablation in an ex-vivo porcine model". In: *Physica Medica: European Journal of Medical Physics* 31 (7), pp. 683–691. DOI: `10.1016/j.ejmp.2015.05.014`. URL: `https://doi.org/10.1016/j.ejmp.2015.05.014`.

[29] Paola Saccomandi, Emiliano Schena, and Sergio Silvestri. "Techniques for temperature monitoring during laser-induced thermotherapy: An overview". In: *International Journal of Hyperthermia* 29.7 (2013), pp. 609–619. DOI: `10.3109/02656736.2013.832411`. URL: `https://doi.org/10.3109/02656736.2013.832411`.

[30] Eva Rothgang et al. "Interventional MR-imaging for thermal ablation therapy". In: Mar. 2011, pp. 1864–1868. DOI: `10.1109/ISBI.2011.5872771`.

[31] T J Vogl et al. "Malignant liver tumors treated with MR imaging-guided laser-induced thermotherapy: technique and prospective results." In: *Radiology* 196.1 (1995). PMID: 7540310, pp. 257–265. DOI: `10.1148/radiology.196.1.7540310`. URL: `https://doi.org/10.1148/radiology.196.1.7540310`.

[32] John De Poorter et al. "Noninvasive MRI Thermometry with the Proton Resonance Frequency (PRF) Method: In Vivo Results in Human Muscle". In: *Magnetic Resonance in Medicine* 33.1 (1995), pp. 74–81. DOI: `10.1002/mrm.1910330111`. URL: `https://onlinelibrary.wiley.com/doi/abs/10.1002/mrm.1910330111`.

[33] R Correia et al. "Biomedical application of optical fibre sensors". In: *Journal of Optics* 20.7 (June 2018), p. 073003. DOI: `10.1088/2040-8986/aac68d`. URL: `https://doi.org/10.1088%5C%2F2040-8986%5C%2Faac68d`.

[34] Yuetong Ding et al. "Dynamic temperature monitoring and control with fully distributed fiber Bragg grating sensor". In: *Progress in Biomedical Optics and Imaging - Proceedings of SPIE* 7845 (Nov. 2010). DOI: `10.1117/12.869931`.

[35] A. Zur and A. Katzir. "Fiber optic distributed thermal sensor". In: *Applied Physics Letters* 53.25 (1988), pp. 2474–2476. DOI: `10.1063/1.100217`. URL: `https://doi.org/10.1063/1.100217`.

[36] Francesco Barone et al. "Fiber-Optic Liquid Level Sensing by Temperature Profiling with an FBG Array". In: *Sensors* 18.8 (2018). ISSN: 1424-8220. DOI: `10.3390/s18082422`. URL: `https://www.mdpi.com/1424-8220/18/8/2422`.

[37] Y. Liu et al. “Innovative Fibre Probe for Laser Ablation of Tumour Cells”. In: *2015 European Conference on Lasers and Electro-Optics - European Quantum Electronics Conference*. Optical Society of America, 2015, $\mathrm{CL}_{P1}4$. URL: `http://www.osapublishing.org/abstract.cfm?URI=CLEO_Europe-2015-CL_P_14`.

[38] Mario Gallati et al. “Laboratorio di termoablazione dei tessuti biologici”. In: URL: `https://docplayer.it/6369113-Laboratorio-di-termoablazione-dei-tessuti-biologici.html`.

[39] Fabrizio Taffoni et al. “Optical Fiber-Based MR-Compatible Sensors for Medical Applications: An Overview”. In: *Sensors* 13.10 (2013), pp. 14105–14120. ISSN: 1424-8220. DOI: `10.3390/s131014105`. URL: `https://www.mdpi.com/1424-8220/13/10/14105`.

[40] Edoardo G. Macchi et al. “Optical fiber sensors-based temperature distribution measurement in ex vivo radiofrequency ablation with submillimeter resolution”. In: *Journal of Biomedical Optics* 19.11 (2014), pp. 1–7. DOI: `10.1117/1.JBO.19.11.117004`. URL: `https://doi.org/10.1117/1.JBO.19.11.117004`.

[41] Alessandra Beccaria. “Studio teorico e sperimentale del comportamento termo-ottico di tessuti biologici per il trattamento di tumori mediante ablazione laser”. Master’s degree thesis. Politecnico di Torino, 2019.